國 立 中 央 大 學

大 氣 科 學 系

博 士 論 文

WRF-LETKF 系統同化反演熱動力場與雷達資料：鋒面雨帶個案之分析探討

Analysis of Assimilating Retrieval Thermodynamic Fields and radar data by the WRF-LETKF Assimilation System: A Case Study of Frontal Rainband

研 究 生：柯緁盈

指導教授：鍾高陞 博士

中 華 民 國 一一一 年 六 月

國立中央大學圖書館學位論文授權書

填單日期：111 / 08 / 04

2019.9 版

授權人姓名	柯綾盈	學 號	104681001
系所名稱	大氣科學學系大氣物理博士班	學位類別	□碩士 ☑博士
論文名稱	WRF-LETKF系統同化反演熱動力場與雷達資料：鋒面雨帶個案之分析探討	指導教授	鍾高陞

學位論文網路公開授權

授權本人撰寫之學位論文全文電子檔：

- 在「**國立中央大學圖書館博碩士論文系統**」.
  - (✓)同意立即網路公開
  - (　)同意 於西元＿＿＿年＿＿＿月＿＿＿日網路公開
  - (　)不同意網路公開，原因是：＿＿＿＿＿＿＿＿＿＿
- 在**國家圖書館「臺灣博碩士論文知識加值系統」**
  - (✓)同意立即網路公開
  - (　)同意 於西元＿＿＿年＿＿＿月＿＿＿日網路公開
  - (　)不同意網路公開，原因是：＿＿＿＿＿＿＿＿＿＿

依著作權法規定，非專屬、無償授權國立中央大學、台灣聯合大學系統與國家圖書館，不限地域、時間與次數，以文件、錄影帶、錄音帶、光碟、微縮、數位化或其他方式將上列授權標的基於非營利目的進行重製。

學位論文紙本延後公開申請 (紙本學位論文**立即公開者此欄免填**)

本人撰寫之學位論文紙本因以下原因將延後公開

- **延後原因**
  - (　)已申請專利並檢附證明，專利申請案號：
  - (　)準備以上列論文投稿期刊
  - (　)涉國家機密
  - (　)依法不得提供，請說明：＿＿＿＿＿＿＿＿
- **公開日期**：西元＿＿＿＿年＿＿＿＿月＿＿＿＿日

※繳交教務處註冊組之紙本論文(送繳國家圖書館)若不立即公開，請加填「國家圖書館學位論文延後公開申請書」

研究生簽名：柯綾盈　　指導教授簽名：鍾高陞

*本授權書請完整填寫並親筆簽名後，裝訂於論文**封面之次頁**。

國立中央大學博士班研究生
論 文 指 導 教 授 推 薦 書

大氣科學學系大氣物理博士班 學系/研究所 柯緁盈 研究生

所提之論文 WRF-LETKF系統同化反演熱動力場與雷達資料：鋒面雨帶個案之分析探討

係由本人指導撰述，同意提付審查。

指導教授 鍾高陞 (簽章)

111 年 08 月 02 日

1110802

國立中央大學博士班研究生
論 文 口 試 委 員 審 定 書

大氣科學學系大氣物理博士班 學系/研究所 柯婕盈 研究生

所提之論文 WRF-LETKF系統同化反演熱動力場與雷達資料：鋒面雨帶個案之分析探討

經由委員會審議，認定符合博士資格標準。

學位考試委員會召集人 連國淵

委　　員 洪景山

林沛練

楊舒芝

鍾高陞

中　華　民　國　111　年　08　月　02　日

1110802

中文摘要

台灣北部出現豪大雨的梅雨鋒面系統個案 2012 年 6 月 11 日，10小時累積雨量多處超過400毫米，北部地區許多測站降雨紀錄創下歷史新高，造成北部各地出現淹水災情。本研究選用此個案，從雷達觀測資料分析，反演三維風場與熱動力場分析系統在台灣北部造成強降雨的複雜因素。進一步探討系集同化系統同化雷達資料，同時加入反演三維空間高解析熱動力場對於極端強降雨事件的降雨預報可行性探討。

研究利用高時空解析亦可解析地形的多都卜勒雷達風場反演技術(WISSDOM)與熱動力反演與水氣調整技術(TPTRS)，從反演結果得到三維風場、溫度、壓力與水氣三維結構結構。透過垂直渦度收支分析強降雨期間，對流尺度上地形噴流移動和強度的變化。研究發現，在台灣北部移速慢的梅雨鋒面，冷池前緣發展新的對流，受地形影響和加強的地形噴流形成Y型回波，對流被地形噴流往北推移和主對流合併加強系統，造就此歷史性的短延遲強降雨個案。

研究使用 WRF-LETKF 雷達同化系統，探討多尺度天氣系統中，同化雷達觀測資料之外，加入同化 3D 溫度和水氣資訊，進行可行性的影響評估。設計觀測系統理想模擬實驗，同化的熱動力變數來自理想無偏差或熱動力反演技術得到的熱動力變數。首先，理想實驗中同化兩小時的雷達資料顯示出比一小時更好的結構和短期降雨預測。其次，從同化雷達觀測變數和完美無偏差的熱力變數(溫度與水氣)分析結果顯示，當背景場出現降水位置誤差時，同化雷達資料加入溫度和/或水氣資訊一起同化，可以修正雨帶位置，縮短同化週期，得到較佳的預報分析場，並顯著改善定量降水預報。第三，進行反演熱力變數同化可行性研究。由於反演溫度和水氣存在偏差。加入反演溫度的資料同化實驗，由於溫度存在暖偏差，分析場的結果顯示，提升對流區的垂直運動和層狀區的冰相變數結構，並在極短期強降雨的預報有明顯效益。同化水氣助於重建近地表冷池的範圍和強度，但對三小時降雨預報的改進有限。同時加入同化反演溫度場和水氣場時，此實驗結果取得了最佳的分析，並能顯示降雨預報效益至少維持六小時。綜上所述，同化複雜降水系統中的三維熱力變數，此效益能縮短同化時間，提升最終分析場結構和短期降雨預報。

English Abstract

A frontal system with extremely heavy rainfall was over Northern Taiwan on 11 June 2012. Through multiple analyses of three different Doppler radars, three-dimensional wind fields are retrieved over the ocean and the complex terrain of Taiwan by Wind Synthesis System using Doppler Measurements (WISSDOM). The pressure and temperature structure are derived from the retrieved wind fields by Terrain-Permitting Thermodynamic Retrieval Scheme (TPTRS). The migration and intensity of the barrier jets at convective scales are revealed by a vorticity budget analysis. It is found that, taken together, the stagnated Mei-Yu front, the location and the strength of the barrier jet and cold pool, as well as orographic blockage over northern Taiwan explain the formation of this quasi-stationary and extremely heavy rainfall case.

This study examined the feasibility of assimilating 3D temperature and water-vapor information in addition to radar observations in a multiscale weather system. Using the WRF–LETKF Radar Assimilation System (WLRAS), we performed three sets of observing system simulation experiments to assimilate radar observations with or without thermodynamic variables obtained using different methods. First, assimilating the radar data for 2 h showed better structure and short-term forecast than 1 h. Second, we assimilated radar data and thermodynamic variables from a perfect model simulation. The results of the analysis revealed that when a precipitation position error was present in the background field, assimilating temperature and/or humidity information could correct the dynamic structure and shorten the spin-up assimilation period, resulting in substantial improvements to the quantitative precipitation forecast. Third, we applied a thermodynamics retrieval algorithm for a feasibility study. With a warm and wet bias of the retrieved fields, assimilating the temperature data had significant impact on the final analysis at the mid-level of stratiform areas and the forecast of the heavy rainfall was consequently improved. Assimilating the water vapor information helped reconstruct the range and intensity of the cold pool near the surface, but the improvement of 3-h rainfall forecast was limited. The optimal results of analysis and short-term forecast were achieved when both the retrieved temperature and water vapor fields were assimilated. In conclusion, assimilating thermodynamic variables in the precipitation system is feasible for shortening the spin-up period of data assimilation and improving the final analysis and short-term forecast.

致謝

在中央大學第十五個年頭，還記得踏入中央大學的第一個暑假，就被系上的C-POL 雷達和剛剛架好的 TEAM-R 深深的吸引。感謝當時林沛練老師和學長姐們，帶著我看了很多觀測儀器、分析資料，走進大自然直接蒐集資料，用熱血和身體力行的方式體驗大氣的奧秘。大四謝師宴當晚的一場大雨，讓我跌進了研究梅雨鋒面的坑。感謝陳台琦老師在我進研究所時，沒有拒絕我研究這個美麗的鋒面個案 2012、611(神秘數字)，總是耐心的帶著我看那一堆又一堆的圖，擺在地上擺地攤，也讓我在這之中能領悟到做研究做到能說出一個故事是一件多麼令人興奮的事情。在碩班畢業後，猶豫了一段時間，最後還是決定帶著緊張、興奮又害怕的心情選擇繼續念博士班。非常感謝我的指導老師鍾高陞老師回到中央大學就願意收我成為您的第一位博士班學生，帶領我挑戰高難度的模式模擬與反演資料的同化，給予滿滿的機會能參加國內外各種研討會，鼓勵我與外面學者交流，也讓我在挑戰博士班的過程中，讓我持續參與各種觀測活動。從野外觀測到電腦模擬，很感謝老師的鼓勵和支持，每每在我快要放棄的時候，總是會出現給予滿滿的希望，最後很開心能和老師一起完成研究，也讓我能有這麼完整的機會參與雷達氣象研究相關的所有過程。

一路走來，要感謝的人太多太多了。廖宇慶老師在雷達反演技術上不斷的突破，讓我在思考研究過程中，也會不自覺的往更高難度的方向去挑戰。張偉裕老師總是像個大學長一樣，隨時充滿活力，常提出不同的思考方向，激發大家一起動動腦。很榮幸能加入雷達實驗室大家庭，感謝所有學長姐們的照顧，學弟妹們的認真與搞笑，還有一起在實驗室的同學們，讓我產生一直還在大學時期很青春的錯覺。

最終要完成畢業論文的前夕，還是遇到了受疫情影響延期再延期的台美日國際聯合大型觀測實驗。就在這最後時刻，以學生的身分在永安的 TEAM-R 值班、加入在新竹的 NCAR S-Pol 實習觀測，帶著熱血參與實驗並完成最後的論文口試。特別感謝百忙之中願意抽空擔任口試委員：林沛練老師、楊舒芝老師、洪景山博士、連國淵博士，給予論文許多建議，讓研究可以更加完整。

最後最後，我真的很想謝天，滿滿的博士班訓練過程，有太多需要感謝的貴人，我都把大家記在心裡。也很感謝家人雖然不太知道為什麼我要一直很忙很忙，仍是默默的支持鼓勵。未來還有很多的未知，期許自己帶著好奇心，繼續探索世界，不懼怕來自四面八方的挑戰。

Table of contents

List of Figures

speed (contour lines); (d) cross-section of vertical wind (colour shaded, unit: m s-1) and wind vector relative to the system motion. Retrieved thermodynamic perturbations (e) pressure at 2 km; (f) temperature at level 2 km (shaded), and wind direction of relative background at 1-km height (vector).

Fig. 3-4. (a) Barrier jet (J1), the vertical vorticity fields (colour shaded, interval is 4*10-4 s^{-1}) and vertical vorticity tendency (contour lines, 0.5 and -0.8*10-6 s^{-2}) on 1-km level from WISSDOM at 1400 UTC; (b) Vertical vorticity budget of 1-km height at 1400 UTC: tilting term (colour shaded, interval is 0.5*10-6 s^{-1}) and stretching term (contour lines, 0.2 and 0.5 *10-6 s^{-1}); (c) same as (a), but at 1530 UTC and J2 indicates the location of the barrier jet; (d) schematic diagram to show the migration and enhancement of the barrier jet. Thinned arrows present the strength of the wind below 3-km height, vortex line is stretched by the upward motion (blue arrow) and induced a pair of vorticity tendency, pink arrows with dashed line is the original barrier jet and solid line is the evolved barrier jet; H and L refer to the location of high and low pressure, respectively.

Fig. 3-5. Schematic diagrams to demonstrate the mechanism of the extremely heavy rainfall event. (a) Pre-frontal convection forms a TS-type precipitation over the ocean, and the line convection is triggered due the cold outflow encountering a warm and humid southwesterly flow; (b) the strengthened cold pool and enhanced barrier jet repeatedly triggered the Y-shaped echo line convection, then merge with the main convection to form a PS-type precipitation over northern Taiwan. The location of the Mei-Yu front and the warm/humid southwesterly flow (red arrow) illustrate the environmental condition of the synoptic scale over Taiwan. The

List of Tables

Chapter 1

Introduction and Motivation

1.1 Introduction

In recent years, short-term heavy rainfall has often caused flooding and disasters. Such systems have small scales and short life cycles, and are affected by complex terrain in Taiwan, resulting in more complex interactions. The small-scale system has already occurred, and the development of the small-scale weather system is relatively nonlinear, so there is still a high degree of uncertainty in the numerical model. Among the observational data, meteorological radars provide real-time high temporal and spatial resolution data to understand the real-time development of small-scale systems and improve initial condition by assimilation which can effectively improve numerical models and reduce the risk.

According to the research on radar data assimilation, most of the reflectivity and radial velocity observed by radar have been successfully assimilated. Kerr et al. (2015) designed an Observing System Simulation Experiment (OSSE) experiment to try to assimilate radar data and then add satellite observations of cloud top temperature assimilation. The results showed that assimilating cloud top temperature alone cannot have a significant effect on rainfall forecasting because the rainfall system is mainly affected by radar data assimilation. However, there is a clear positive improvement for snow and soft hail when assimilating cloud top temperature. Ge et al. (2013) used the OSSE to simulate super cellular storms, and used the ARPS 3DVAR assimilation system to explore the importance of assimilating different meteorological variables for

convective-scale analysis fields. The results show that in the assimilation observation data at the convective scale, the most important is the horizontal wind, and the second is the water vapor and temperature field. The author mentioned that whether this conclusion is the same conclusion for different assimilation systems (such as 4DVAR and EnKF) remains to be confirmed.

Extending from radar observations and further through inversion techniques, additional information at the convective scale can be obtained. As mentioned in the literature, many studies have empirically converted radar observations into humidity field information for assimilation (Liou et al. 2003; Caumont et al. 2010; Wattrelot et al. 2014; Jacques et al. 2018). A moisture adjustment method was based on that of Liou et al. (2014), who proposed a simple and effective approach for adjusting temperature and moisture fields through iterative methods. In fact, the refractivity that can be observed by weather radar is a function of temperature and humidity. Radar observations are not only additional observational information, but are constantly being studied and improved (Nicol et al. 2013; Feng and Fabry 2016). At the same time, in the past, many countries have also tried to assimilate the additional radar observations besides reflectivity and radial wind into small and medium-scale systems. (Montmerle et al. 2002; Gasperoni et al. 2013; Nicol et al. 2014; Seko et al. 2017; Do et al., 2022).

Boutter (1994) mentioned that, especially in areas where observational data are sparse, observational information follows characteristics related to background errors. Zhang (2005) used an extratropical cyclone case to explore the mesoscale error structure of variables related to heat and dynamics and observed that the growth of the error can be interpreted by the mechanism of atmospheric dynamic balance, showing

that the flow field is flow-dependent. The characteristics and anisotropy of moisture processes are the main sources of error growth; Chung et al. (2013) used the Canadian ensemble Kalman filter and its forecasting system to explore the short-term situation-dependent structure of forecast errors at the convective scale. The results show that the error structures of rainfall and non-rainfall trends are significantly different, and the structure in the vertical direction is obviously affected by cloud physics.

1.2 Review of radar assimilation

The information provided by meteorological radar observations includes wind field and precipitation has high temporal and spatial resolution. For the small and medium-scale convective precipitation system, in addition to having a good monitoring function, in the research and development of radar meteorology, it is further discussed how to improve the real-time and very short-term weather forecast. Using simple extrapolation of radar reflectivity (Browning et al. 1982; Germann and Zawadzki 2002; Mandapaka et al. 2012), the location and intensity of precipitation in 0-6 hours can be estimated. The advantage of the extrapolation method is that it only needs to use very few computer computing resources. However, if the weather system has obvious development and dissipation in a very short time, the quantitative precipitation forecasting ability will decrease quickly, so the radar reflectivity extrapolation method is limited in 0~2 hours.

In order to overcome the limitations of the radar reflectivity extrapolation, the concept of data assimilation has been proposed. The meteorological radar observation data and numerical forecasting model are objectively used to obtain accurate mesoscale

and small-scale weather analysis fields. Radar data assimilation methods are mainly divided into three systems, three-dimensional variational scheme (3DVAR), four-dimensional variational scheme (4DVAR) and ensemble Kalman filter (ensemble Kalman filter, EnKF). 3DVAR is the most common data assimilation method for operating centers due to its high stability and low computing resources. The disadvantage of this approach is that it presents fixed background error information from climate statistics and is assimilated over all observations at a single time. Xiao et al. (2005) used the MM5 model to assimilate single-radar radial winds to improve rainfall forecasts for frontal rainbands. Xiao and Sun (2007) and Sugimoto et al. (2009) found that assimilating radar echoes is also helpful for short-term quantitative precipitation forecasting.

4DVAR further utilizes a large number of computing resources and considers the development of time and space. This method takes into account the prediction of error structure of flow field dependence by the adjoint model. However, this method needs to write the adjoint model, and requires large computing resources. By analyzing and diagnosing different cases, both the analysis field and the short-term forecast performance have been improved to a considerable extent. VDRAS (Variational Doppler Radar Analysis System) system is the leader of 4DVAR radar data assimilation in recent years (Sun and Crook 1997, Sun and Crook 2001, Chang et al. 2014a, Chang et al. 2016, Tai et al. 2017). In addition, NOAA (National Oceanic and Atmospheric Administration) uses the Rapid Update Cycle (RUC, Benjamin et al. 2004) model to assimilate radar echoes every hour to obtain a more accurate mesoscale initial field, which is provided for the high-resolution operation mode of 3 kilometers horizontally

High Resolution Rapid Refresh (HRRR, Benjamin et al. 2016) to enables forecasting techniques to reach 3-6 hours.

Many studies have used the Ensemble Kalman Filter (EnKF) system for assimilation. Ensembles can provide more information than a single deterministic forecast, and this approach has been extensively tested at different meteorological scales (Evensen 1994, Bishop et al. 2001, Anderson 2001, Whitaker and Hamill 2002, Hunt et al. 2007). Compared with the four-dimensional variational method in the application of medium and small scales, its advantages are: (1) its method does not require complex adjoint models; (2) it can maintain the medium and small scale flow field dependencies in the assimilation process (The properties of flow-dependent) (Chung et al. 2013, Ménétrier et al. 2015); (3) ensembles provide the uncertainty of numerical models in analysis and forecast. Therefore, many studies used this method to assimilate radar observation for analysis and discussion. Snyder and Zhang (2003) used the EnKF system for the first time to assimilate radar data for OSSE experiments. Tong and Xue (2005) used the Advanced Regional Prediction System (ARPS; Xue et al. 2006) model to assimilate the echoes and found that directly updating the relevant forecast variables yielded the best analysis results. Zhang et al. (2009) used the WRF-EnSRF system to assimilate radar data and applied it to a multi-scale weather case study to effectively improve hurricane track and intensity forecasts in the United States. Aksoy et al. (2010) used the DART (Data Assimilation Research Testbed) system with an ensemble adjustment Kalman filter (EAKF; ensemble adjustment Kalman filter, Anderson 2001) to assimilate radial winds and reflectivity to accurately predict and analyze different convection patterns. Tsai et al. (2014) used the WRF-LETKF Radar

Assimilation System (WLRAS, WRF-LETKF Radar Assimilation System), through OSSE experimental design, according to the characteristics of the spatial correlation distribution of different variables, designed the mixed localization radius, in Taiwan, which has a complex terrain environment, could effectively improve the short-term rainfall forecasting ability of typhoon Morakot. In addition, researches on the hybrid method (Hamill and Snyder 2000, Wang et al. 2007, Li et. al 2012, Gao and Stensrud 2014) that combine the variational method and the ensemble Kalman filter are desirable to obtain the optimized initial field.

1.3 Motivation of the study

In recent years, many studies have conducted on assimilating additional high-resolution information with radar data to improve storm-scale numerical weather prediction (NWP). Using a 3DVar system with observing system simulation experiments (OSSEs), Ge et al. (2013) investigated the impact of assimilating different state variables at the convective scale; their results demonstrated that dynamic variables such as horizontal wind play a major role in analyzing storm structure. Moreover, they revealed that thermodynamic variables such as temperature and humidity are more effective than hydrometeor variables for reconstructing severe storms because hydrometeors are primarily indicators of thermodynamical processes; without supporting wind, temperature, and humidity information, hydrometeors rapidly evaporate or precipitate. Many studies have attempted to include thermodynamic information into radar data. For example, Wattrelot et al. (2014) assimilated retrieved humidity profiles and radar data by using a 1D + 3DVar assimilation method. Their

results revealed the positive impact of analysis and short-term forecasts. Kerr et al. (2015) evaluated the effect of assimilating both cloud-top temperature from satellite data and radar observations, whereas Caumont et al. (2016) assimilated retrieved temperature and humidity profiles from ground-based microwave radiometers. Other strategies, such as using vertical integrated liquid water content or differential reflectivity columns to modify humidity or temperature or both, have recently been tested (Carlin et al. 2017; Lai et al. 2019), demonstrating substantial utility in terms of high-impact weather events.

The potential impact of assimilating both radar data and retrieved thermodynamic information remains unclear, and most studies have focused on areas of strong convection. Themens and Fabry (2014) described the potential benefit of providing temperature and humidity information over 3D domains for mesoscale forecasting, and high-density thermodynamic information has been successfully retrieved from radar data (Liou et al. 2019; Feng and Fabry 2016; Ellis and Vivekanandan 2010) despite some concerns related to accuracy and bias.

Since the impact of assimilating 3D thermodynamic variables inside severe weather systems had not been completely investigated, we conducted a series of OSSEs to explore this issue for both analysis and short-term forecast. First, high-density temperature and/or humidity fields were assimilated along with radar data simulated from a nature run. This was to evaluate and illustrate the added value of assimilating thermodynamic information to the ensemble-based DA system without the uncertainty due to thermodynamic retrieval algorithms. Second, a terrain-permitting thermodynamic retrieval scheme (TPTRS; see Liou et al. 2019) was applied to retrieve

temperature and water vapor assimilated to the DA system. Considering the uncertainty of the retrieval scheme, it is able to understand the feasibility of assimilating the thermodynamic information. A case study of a frontal system was selected to examine and demonstrate the impact of assimilating these observations in different areas of the precipitating weather system. The EnKF type assimilation system WLRAS was used in this study. In the assimilation of radar data at the convective scale, an ideal case experiment are used to explore the effect of adding a thermodynamic field (temperature, water vapor) in addition to the assimilation of radar reflectivity and radial wind information, and conduct a series of assessments of the impact and benefits of severe weather systems.

Chapter 2

Methodology and Data Operator

2.1 Wind Synthesis System using Doppler Measurements (WISSDOM)

In this study, a variational-based algorithm (Liou and Chang, 2009 and Liou et al. 2012) is used to retrieve the three dimensional wind fields with multiple Doppler radars. The system is named Wind Synthesis System using Doppler Measurements (WISSDOM, Liou et al. 2016). In Liou and Chang (2009), the uncertainties of the retrievals have been tested and validated with idealized experiments, and results show that the errors of horizontal winds are very small; larger uncertainty remains in vertical. In addition, the accuracy of the retrieved winds in real cases have been verified with an independent radar. This algorithm has been applied to diagnose different real case studies (Liou et al. 2013, Lee et al. 2014, and Liou et al. 2016). Brief descriptions and major features of WISSDOM are given as follows. There are five (weak) constraints in the cost function of WISSDOM for obtaining the optimal three dimensional winds, and they are:

(1) The geometric relation to connect the retrieved Cartesian wind components and the radial velocity directly measured by the individual radar

$$J_1 = \sum_{t=1}^{2} \sum_{x,y,z} \sum_{i=1}^{N} \alpha_{1,i} \left(T_{1,i,t}\right)^2, \tag{1}$$

$$T_{1,i,t} = (V_r)_{i,t} - \frac{(x - P_x^i)}{r_i} u_t - \frac{\left(y - P_y^i\right)}{r_i} v_t - \frac{(z - P_z^i)}{r_i} \left(w_t + W_{T,t}\right), and$$

$$r_i = \sqrt{(x - P_x^i)^2 + \left(y - P_y^i\right)^2 + (z - P_z^i)^2},$$

where the subscripts *t* (from 1 to 2) indicates the number of time levels, and *i* (from

1 to N) is for the number of radar sites. $(V_r)_{i,t}$ is the radial winds observed by *i*th radar at time *t*, $(u_t,\ v_t,\ w_t)$ mean the three-dimensional wind at the location (*x,y,z*) at time *t*, and $W_{T,t}$ represents the terminal velocity, which can be estimated using radar reflectivity data. $(P_x^i,\ P_y^i,\ P_z^i)$ denote the coordinates of the *i*th radar, and r_i is the distance for each grid point to the *i*th radar.

(2) The difference between the retrieved wind field (Vt) and the background winds ($V_{B,t}$):

$$J_2 = \sum_{t=1}^{2} \sum_{x,y,x} \alpha_2 \left(V_t - V_{B,t}\right)^2 \tag{2}$$

This constraint provides auxiliary information in the data void region in the retrieved domain.

(3) The anelastic continuity equation, expressed as:

$$J_3 = \sum_{t=1}^{2} \sum_{x,y,z} \alpha_3 \left[\frac{\partial(\rho_0 u_t)}{\partial x} + \frac{\partial(\rho_0 v_t)}{\partial y} + \frac{\partial(\rho_0 w_t)}{\partial z}\right]^2 \tag{3}$$

where ρ_0 is the air density that varies with height only

(4) The simplified vertical vorticity equation which neglects the mixing and baroclinic terms, and it is formulated as:

$$J_4 = \sum_{x,y,z} \alpha_4 \left\{\frac{\partial \xi}{\partial t} + \left[\overline{u_t \frac{\partial \xi}{\partial x} + v_t \frac{\partial \xi}{\partial y} + w_t \frac{\partial \xi}{\partial z} + (\xi + f)\left(\frac{\partial u_t}{\partial x} + \frac{\partial v_t}{\partial x}\right) + \left(\frac{\partial w_t}{\partial x}\frac{\partial v_t}{\partial y} - \frac{\partial w_t}{\partial y}\frac{\partial u_t}{\partial z}\right)}\right]\right\}^2 \tag{4}$$

where $\xi = \left(\frac{\partial v}{\partial x} - \frac{\partial u_t}{\partial y}\right)$ is the vertical vorticity and f is the Coriolis parameter. The overbar represents a temporal average over the two time levels.

(5) The Laplace smoothing filter, defined as:

$$J_5 = \sum_{t=1}^{2} \sum_{x,y,z} \alpha_5 [\nabla^2 (u_t + v_t + w_t)]^2 \tag{5}$$

where $\nabla^2 = \frac{\partial^2}{\partial x^2} + \frac{\partial^2}{\partial y^2} + \frac{\partial^2}{\partial z^2}$, and the purpose of this penalty term is to minimize the discrepancy between observation and data-void region. The weighting coefficients in equations (1) – (5) are given the same values as Liou et al. (2009).

The cost function of WISSDOM includes basic constraints for wind retrieval: a geometric relation to connect radial component and three dimensional winds, an anelastic continuity equation, and the Laplacian smoothing term in space. In addition, extra constraints are applied in the algorithm: 1) a background term to cover the data-void region; 2) a vertical vorticity equation in the cost function to guarantee the balance of the vorticity budget. As mentioned in Liou et al. (2009), this constraint can both improve the accuracy of the wind and thermodynamic retrievals. With these formulas as weak constraints, WISSDOM is able to retrieve the wind field along the radar baseline. By implementing the Immersed Boundary Method (IBM, Tseng and Ferziger 2003), Liou et al (2012) improved the WISSDOM so the retrieval algorithm can take into account the terrain effect.

2.2 Terrain-Permitting Thermodynamic Retrieval Scheme (TPTRS)

The terrain-permitting thermodynamic retrieval scheme (TPTRS, Liou et al., 2019) is an algorithm for immediately retrieving the 3D pressure and temperature fields for complex terrain using wind information. In the algorithm, three basic equations of motion employ momentum equations to obtain thermodynamic fields (Liou et al. 2003), including moisture-related contributions:

$$\frac{1}{\theta_{v0}}\left[\frac{\partial u}{\partial t}+\vec{V}\cdot\nabla u-fv+turb(u)\right]=-\frac{\partial \pi'}{\partial x}\equiv -F \tag{6}$$

$$\frac{1}{\theta_{v0}}\left[\frac{\partial v}{\partial t}+\vec{V}\cdot\nabla u-fv+turb(v)\right]=-\frac{\partial \pi'}{\partial y}\equiv -G \tag{7}$$

$$\frac{1}{\theta_{v0}}\left[\frac{\partial w}{\partial t}+\vec{V}\cdot w+turb(w)+gq_r\right]=-\frac{\partial \pi'}{\partial z}+g\frac{\theta_c'}{\theta_0\theta_{v0}}\equiv -H \tag{8}$$

$$u\frac{\partial \theta_c'}{\partial x}+v\frac{\partial \theta_c'}{\partial y}+w\frac{\partial \theta_c'}{\partial z}+w\frac{\partial \theta_0}{\partial z}+S=0 \tag{9}$$

In the equation, the subscript *0* on the right represents the basic state, and a prime represents the disturbance of the basic state. f is the Coriolis parameter; g is the gravitational acceleration; q_r is rain mixing ratio, which can be estimated by radar reflectivity. In the formula, gq_r represents the buoyancy term. The left formula represents the wind field of the three components in the space of *u*, *v*, and *w*, which is known from WISSDOM; where *S* is the total effect of the temporal variation, diffusion, and source/sink achieved through microphysical processes (Liou, 2001). The *S* term is treated as a retrievable parameter in the study, and no additional parameterizations were applied.

Furthermore, the contributions of vapor, cloud, and rainwater are included to estimate the buoyancy force. In the retrieval scheme, a normalized pressure (π) is obtained (Exner function), and it is defined as

$$\pi = C_p\left(\frac{P}{P_{00}}\right)^{\frac{R}{C_p}} \tag{10}$$

where P is the air pressure, P_{00} is 1000 hPa, R is the air constant, and C_p is the specific heat capacity at constant pressure. In addition, θ_{v0} is the basic state of the virtual potential temperature; it is the virtual cloud potential temperature, which has included the contributions of water vapor and rain. Defined as follows:

$$\theta_{v0}=\theta_0(1+0.61q_{v0}) \tag{11}$$

$$\theta_c'=\theta'+(0.61q_v'-q_c)\theta_0 \tag{12}$$

Here, q_{v0} is a water vapor mixing ratio, and q_c is a cloud-water mixing ratio. In (12), q_r refers to the rainwater mixing ratio, which can be estimated using the relationship with radar reflectivity (η in dBZ, Sun and Crook 1997):

$$\eta = 43.1 + 17.5log(\rho q_r) \tag{13}$$

where ρ is the air density.

2.3 Moisture and temperature adjustment scheme

The moisture adjustment method was based on that of Liou et al. (2014), who proposed a simple and effective approach for adjusting temperature and moisture fields through iterative methods. In the process, the water vapor mixing ratio perturbation is initially set to 0, and then the temperature is converted to temperature T through equation (12), where the virtual cloud potential temperature is the thermodynamic field derived from the temperature perturbation field and the cloud-water mixing ratio is derived from the model. The model is treated as DA and uses the inverted surface temperature and pressure to calculate the dew-point temperature:

$$T_d = \frac{B}{ln(A\varepsilon/q_{wv}P)_{sfc}} \tag{14}$$

$$A = 2.533 \times 10^8 \ \ kPa \tag{15}$$

$$B = 5.417 \times 10^3 \ \ K \tag{16}$$

$$\varepsilon = 0.622 \tag{17}$$

$$q_{wv} = q'_{wv} \ \ + q_{v0} \tag{18}$$

When the radar reflectivity exceeds 10 dBZ, this area is regarded as saturated. The value

of the saturated water vapor mixing ratio on these saturated grid points is calculated, the water vapor mixing ratio of the basic state is subtracted to obtain a new q'_{wv}, and the result is substituted into formula (12) to obtain a new potential temperature perturbation field θ'. Subsequently, the difference between the newly obtained water vapor perturbation and potential temperature perturbation and the original water vapor perturbation field and potential temperature perturbation field is calculated. If the difference between the two is less than the threshold, the calculation is stopped and the water vapor adjustment iterative process is complete, resulting in a new q'_{wv} and θ'. The threshold values are 5×10^{-5} for the temperature field and 5×10^{-2} for the water vapor mixing ratio.

2.4 WRF-LETKF Radar Assimilation System (WLRAS)

This study uses the radar assimilation system WRF-LETKF Radar Assimilation System (WLRAS) built by Tsai et al. (2014), which for the first time aims to improve quantitative precipitation nowcasting. After that, many papers have successfully used WLRAS to study the Meiyu system and typhoon system in Taiwan. Shao (2015) applied this system for the first time, and successfully improved the short-term rainfall forecast of a real case Meiyu system. Wu (2015) relocated typhoon Morakot into the ensemble to improve convective-scale quantitative precipitation real-time forecasting, and Zheng (2017) discussed the impact of multi-scale heavy rainfall Meiyu system on forecasting.

The Local Ensemble Transform Kalman Filter (LETKF) is one representation of the deterministic EnKF, developed at the University of Maryland (Ott et al. 2004), and the full method description is first seen in Hunt et al. (2007). Like other EnKF methods,

LETKF is derived under the framework of minimum variance unbiased estimation. LETKF has the common advantages of other EnKF methods: (a) the background error covariance estimated by the forecast ensemble is flow-dependent, which can better represent the local error characteristics than the fixed background error covariance used by 3DVAR; (b) EnKF and 4DVAR have comparable analysis accuracy (Caya et al. 2005; Yang et al. 2009; Miyoshi et al. 2010), but EnKF does not need to write tangent linear models and adjoint models, so it is easily to different models. (c) the complete nonlinear model and nonlinear observation operators can be used to deal with the nonlinear processes of the atmosphere; (d) the analysis algorithm of EnKF can be easily parallelized. In addition, EnKF can handle the reliability of ensemble error covariance through covariance localization techniques (Greybush et al. 2011).

Brief descriptions of LETKF's features are provided here, and the details of the algorithm are available in the studies of Hunt et al. (2007) and Yang et al. (2009).

The final analysis can be obtained as follows: each grid point is independently operated, which can be expressed as a matrix formula as follows:

(1) Estimate the state variables and their uncertainty by updating the ensemble mean and perturbations as

$$\overline{\mathbf{x}_a} = \overline{\mathbf{x}_b} + \mathbf{X}_b\overline{\mathbf{w}} \tag{19}$$

$$\mathbf{X}_a = \mathbf{X}_b\mathbf{W} \tag{20}$$

where $\bar{\mathbf{x}}$ is the ensemble mean of the model variables, $\mathbf{X}$ is the ensemble disturbance of the model variables, and the subscripts *a* and *b* are the analysis field and the background field.

(2) $\overline{\mathbf{w}}$ and $\mathbf{W}$ are the weight coefficients of the mean field and the perturbation field. Through the localization process, the background field and observation information within the grid localization radius are selected, and the obtained weight coefficient formula is as follows:

$$\overline{\mathbf{w}} = \widetilde{\mathbf{P}_a}\mathbf{Y}_b^T\mathbf{R}^{-1}(\mathbf{y}_o - \overline{\mathbf{y}_b}) \tag{21}$$

$$\mathbf{W} = \left[(K-1)\widetilde{\mathbf{P}_a}\right]^{1/2} \tag{22}$$

Among them, $\mathbf{y}_o$ is the observation vector, the matrix $\mathbf{y}_b$ and the column vector $\overline{\mathbf{y}_b}$ are the background ensemble mean and disturbance in the observation space, respectively, and $\mathbf{R}$ is the observation error covariance matrix, which is diagonal due to the assumption that the observation errors are independent matrix, I is the identity matrix, K is the number of ensembles.

(3) $\widetilde{\mathbf{P}_a}$ is the analysis error covariance matrix in the ensemble space, which can be calculated as:

$$\widetilde{\mathbf{P}_a} = [(K-1)\mathbf{I}/\rho + \mathbf{Y}_b^T\mathbf{R}^{-1}\mathbf{Y}_b]^{-1} \tag{23}$$

where matrix $\mathbf{Y}_b$ represents the perturbations in the observation space, $\mathbf{R}$ is the observation error covariance matrix, $\mathbf{I}$ is an identity matrix, K is the ensemble size, and ρ is a multiplicative covariance inflation factor (Anderson 2001).

(4) The R-localization scheme (Hunt et al. 2007) models the observation error with a Gaussian function to propagate the information between the observation and analysis grid point. Figure 2-1 presents a schematic of a horizontal and vertical R-localization.

(5) To sum up the above, $\overline{\mathbf{w}}$ can keep the observational information in the average

state of the ensemble, and W has the characteristic of flow-dependent error structure. Finally, the analysis field of each ensemble member is:

$$\mathbf{x}_a = \overline{\mathbf{x}_a} + \mathbf{X}_a = \overline{\mathbf{x}_b} + \mathbf{X}_b\overline{\mathbf{w}} + \mathbf{X}_b\mathbf{W} \tag{24}$$

The LETKF system is coupled with the WRF model in the present study. The system was originally developed by Yang et al. (2009) for assimilating conventional observations, and Tsai et al. (2014) modified this system for radar DA at the convective scale, renaming it the WRF–LETKF radar assimilation system (WLRAS). The features and setup of this system are described as follows:

(1) A mixed localization strategy (Tsai et al. 2014) is used to avoid unrealistic correlations and assign different error covariance localization radii to different model variables. In the present study, three horizontal radii of 36 (horizontal wind, U and V), 24 (temperature T, water vapor mixing ratio Qv, and cloud mixing ratio Qc), and 12 km (vertical velocity W, rain mixing ratio Qr, snow mixing ratio Qs, and graupel mixing ratio Qg) are used to update the model variables. The vertical localization radius is 4 km for all the variables.

(2) A data quality control procedure is used to reject a particular observation if the innovation (the difference between the observation and background state) is three times larger than the observation error.

(3) To address the under-dispersive problem, an inflation coefficient ρ is applied, and an empirical value of 1.08 is used throughout the assimilation experiments.

(4) In contrast to the findings of Tsai et al. (2014), all the observations assimilated in the WLRAS system are used to update all the model variables without switching off any cross-variable error correlation.

2.5 Observation data and Operator

This study continues the setting of Tsai et al. (2014) and Shao (2015) using the WLRAS assimilation system, and further modifies two parts 1) In order to understand the cross-correlation characteristics between observed variables and model variables, the observed variables are no longer limited to only update specific model variables. The observation data can simultaneously update the three-dimensional wind fields (U, V, W), temperature (T), humidity (Qv) and microphysical variable fields (Qr, Qs, Qg, Qi. Qc) through the assimilation process. 2) The operator of reflectivity is improved into a more complex process, including considering rain, graupel, and snow, and distinguishing the difference between dry snow and wet snow around zero degrees Celsius.

The observation operator for the reflectivity is the sum of rain, snow, and graupel under the assumptions of the Marshall-Palmer raindrop size distribution (Marshall and Palmer 1948) and considering the contribution of ice particles:

$$Z = Z_r + Z_s + Z_g \tag{25}$$

According to Dowell et al. (2011), the rain reflectivity formula is as follows:

$$Z_r = \frac{7.2\times10^{20}\times(\rho_a q_r)^{1.75}}{\pi^{1.75}\times {n_{0r}}^{0.75}\times {\rho_r}^{1.75}} \tag{26}$$

n_{0r} is the intercept parameter and ρ_r is the air density. Since the microphysical

scheme used in this experiment is Goddard Cumulus Ensemble (GCE) models (Tao et al. 2003) 3-ice scheme, the intercept parameter and the rainwater density are:

$$n_{0r} = 8 \times 10^6 \ \ (m^{-4}) \tag{27}$$

$$\rho_r = 1000 \ \ \left(\frac{\text{kg}}{m^3}\right) \tag{28}$$

In this study, the snow below 0 degrees Celsius is dry snow, and the snow above 0 degrees Celsius is wet snow. The reflectivity formulas are as follows:

$$Z_{s-dry} = \frac{\frac{{K_i}^2}{{K_r}^2} \times \left(\frac{{\rho_s}^2}{{\rho_r}^2}\right) \times 7.2 \times 10^{20} \times (\rho_a q_s)^{1.75}}{\pi^{1.75} \times {n_{0s}}^{0.75} \times {\rho_s}^{1.75}} \ \ , T < 0°C \tag{29}$$

$$Z_{s-wet} = \frac{7.2 \times 10^{20} \times (\rho_a q_s)^{1.75}}{\pi^{1.75} \times {n_{0s}}^{0.75} \times {\rho_s}^{1.75}} \ \ , T > 0°C \tag{30}$$

where *K* is the permittivity, and similarly the intercept parameter and density of snow are as follows:

$$n_{0s} = 1.6 \times 10^7 \ \ (m^{-4}) \tag{31}$$

$$\rho_s = 100 \quad \left(\frac{\text{kg}}{m^3}\right) \tag{32}$$

Similarly, the reflectivity formula (33), intercept parameter (34) and density (35) of hail are obtained as follows:

$$Z_g = \frac{0.23 \times \left(\frac{{\rho_g}^2}{{\rho_r}^2}\right) \times 7.2 \times 10^{20} \times \left(\rho_a q_g\right)^{1.75}}{\pi^{1.75} \times {n_{0g}}^{0.75} \times {\rho_g}^{1.75}} \tag{33}$$

$$n_{0g} = 4 \times 10^6 \ \ (m^{-4}) \tag{34}$$

$$\rho_g = 400 \ \ \left(\frac{\text{kg}}{m^3}\right) \tag{35}$$

Finally, the operators for the reflectivity contributions from rain (36), dry snow (37), wet snow (38) and graupel (39) are as follows:

$$Z_r = 3.63 * 10^9(\rho_a q_r)^{1.75} \quad (36)$$

$$Z_{s-dry} = 2.79 * 10^8(\rho_a q_s)^{1.75} \quad (37)$$

$$Z_{s-wet} = 1.21 * 10^{11}(\rho_a q_s)^{1.75} \quad (38)$$

$$Z_g = 1.12 * 10^9\left(\rho_a q_g\right)^{1.75} \quad (39)$$

Chapter 3

Case study: Mei-Yu front on 11 June 2012

3.1 Case review

A mesoscale convective rainfall event accompanied by a frontal system on 11 June 2012 was selected for this study. The weather system resulted in total accumulated rainfall of more than 400 mm within 10 h, leading to flooding in Northern Taiwan.

According to an analysis of the surface weather map (Fig. 3-1a), the Mei-Yu front remained north of Taiwan at 1200 UTC on June 11 (2000 LST), and the weather map at 850 hPa revealed a short-wave trough and abundance of water vapor over the ocean west of Taiwan (Fig. 3-1b). During this time, a strong and deep southwesterly was flowing from the surface to the mid-levels in the southern region of the frontal system. The environmental conditions ahead of the frontal system were highly favorable to the development of severe weather.

Figure 3-2 illustrates the evolution of the composite reflectivity observed by the RCWF radar at 1-h intervals from 1200 to 1600 UTC. At 1200 UTC, a line convection system with strong reflectivity (>40 dBZ) approached Northern Taiwan. After the system landed over Taiwan, a convective cell with a line shape was triggered along and parallel to the northwest coast and then merged with the main precipitation system. This feature was repeated twice between 1400 and 1600 UTC while the main precipitating system remained quasi-stationary.

This event was poorly predicted by the Central Weather Bureau of Taiwan because a 5-km resolution numerical weather prediction model failed to accurately capture the

precipitation system that had become stationary over Northern Taiwan. Wang et al. (2016) studied this event with a higher resolution (1.5-km) numerical simulation to analyze its dynamics and thermodynamics. Despite their strategy of nesting and downscaling, they realized that improving the initial conditions for a very short-term QPF at the cloud resolving scale was crucial. By using radiosondes, surface observations, and reanalysis data, Chen et al. (2018) demonstrated that high moisture content and the existence of a barrier jet accompanying a frontal system caused long-lived convection cells over Taiwan's northwestern coast. Using a retrieval algorithm to obtain wind, pressure, and temperature data in three dimensions, Ke et al. (2019) examined the evolution of severe weather phenomena by using multiple Doppler radar observations. These studies highlight the role of multiscale features (such as the location of the frontal system, strength of the barrier jet, and cold pool) and orographic interactions in the formation of the front over Northern Taiwan.

3.2 Evolution of Reflectivity

The evolution of the precipitation system is illustrated by radar observations. Figure 3-2 shows the composite reflectivity of the RCWF radar at 30-minute intervals from 1200 UTC to 1600 UTC. At 1200 and 1230 UTC, a main convection centre C1 (defined as reflectivity > 40 dBZ and length > 150 km) approached northern Taiwan. During this time interval, a line convection S1 (length of approximately 50 km), oriented in an east-west direction, occurred along the southwest part of the main precipitation system and continued to develop (Fig. 3-2a, b). When the system moved toward Taiwan, the main convection C1 weakened at 1300 and 1330 UTC according to

the reflectivity (Fig. 3-2c, d). C1 continued to move southeast towards northern Taiwan and eventually merged with S1. The convention center C2 was formed at 1400 UTC (Fig. 3-2e), strengthening the main convection. Based on the leading edge of the strong reflectivity (>40 dBZ), we determined that the precipitation system landed over northern Taiwan at 1400 UTC. After landing, a line convection S2 (Fig. 3-2f) was triggered again at the south western part of the main precipitation system parallel to the orography. S2 merged with C2 at 1500 UTC, yielding C3 (Fig. 3-2g). A new line convection, S3, resembling S2 (Fig. 3-2h) formed at 1530 UTC; subsequently it merged with the main convection, yielding C4 (Fig. 3-2i).

Parker and Johnson (2000) categorized linear convection of the MCS into three different types based on the environmental flow, speed of translation, and the reflectivity pattern of the precipitation system: trailing stratiform (TS), leading stratiform (LS) and parallel stratiform (PS). According to their categorization, the precipitation system changed from TS (1200-1230 UTC; Figs. 3-2a, b) to PS (1430-1600 UTC; Figs. 3-2f – i). By plotting contours of reflectivity values greater than 40 dBZ, the echo of the Y-shaped structure at 1430 and 1530 UTC is clearly demonstrated (Fig. 3-2j). This repeated Y-shaped echo structure is not uncommon in northern Taiwan. Previously, Wang et al. (1991) examined this structure by using a Velocity Azimuthal Display (VAD) algorithm. Deng et al. (1992) further analysed the synoptic environment when the Y-shaped echo structure occurred. However, their studies focused on the synoptic-scale conditions and strong mesoscale convection when the precipitation system remained over the ocean.

According to the system translation speed (estimated by the strong line echo, Z >

40dBZ, of the radar observation) and the pattern of the rainband, we divide the lifecycle of the precipitation system into three different stages (Table 3-1). The first 30-min (1200-1230 UTC) is stage one. During this time, the system moved rapidly (15 km hr-1) from the southern China to the northern Taiwan. Between 1300 UTC and 1400 UTC, the system underwent a transitional period: the line convection S1 merged with C1 (see Fig. 3-2), and the united convection C2 landed in northern Taiwan. This is defined as the second stage. During the third stage (after 1430 UTC), the line convection S2 and S3 with Y-shaped echo formed and merged with the main convection, and the displacement of the system became quasi-stationary.

It should be noted that these synoptic-scale features are commonly seen during the Mei-Yu season in Taiwan. However, how to form a quasi-stationary precipitation system with repeated Y-shaped echoes is not fully known. In the next section, the structure of the precipitation system and its evolution in time are investigated using a retrieval technique.

3.3 Result of retrieval by WISSDOM and TPTRS at 1400 UTC

The retrievals show transition features when the precipitation system landed over Taiwan. Before the line convection S1 merges with the main convection C1 (Fig. 3-2d, e), the low-level convergence (at 1-km height) and vertical velocity (at 5-km height) at 1330 UTC reveal that the convection C1 was weakening (not shown). After merging, the intensity of the convergence field and updraft motion at 1400 UTC (Fig. 3-3a) is maintained similarly to the first stage.

On the other hand, Fig. 3-b shows the region of the barrier jet (isotach > 15 m s^{-1})

was wider and stronger than the result at 1200 UTC. In the transition period, the cross-section (see Fig. 3-3a, line 2-2') of the reflectivity shows that a new convection (~121°E) developed in the south-west of the main precipitation system. The isotach in Fig. 3-2c illustrates that an intense wind (southwesterly) exists between 2 and 5 km on the southwest side of the strong reflectivity. The retrieved vertical motion in Fig. 3-2d shows a tilted structure (southwest to northeast), and the updraft is much stronger than the downdraft.

The pressure perturbations at 2-km height at 1400 UTC are shown in Fig. 3-3e. A meso-low center (L1) is distributed over the retrieved domain at 1400 UTC. The low of L1 is caused and followed by the precipitation system. In the meantime, a relative weak low, L2, is located inland of northern Taiwan. The intensity of the low pressure (L2) is weaker before convection S1 united with C1, and it is strengthened (Fig. 3-3e) after the two systems merged over northern Taiwan. The pressure gradient force due to L2 over land would accelerate area I and decelerate area II of the southwesterly wind (Fig. 3-3e). The forcing in area I is superimposed over the original barrier jet and this could explain the enhancement and extension of the barrier jet at 1400 UTC (Fig. 3-3b).

The temperature fields (Fig. 3-3f) at 2-km height illustrate that the warm region stays in the southwest of the retrieval domain. From the sounding data for Makung and Banqiao stations, the wind shear below 700 hPa indicates warm advection, as in Li et al. (1997). Therefore, it is expected that the enhanced barrier jet would advect more humid and warm air from the south of the ocean and that the positive temperature perturbation would be larger at 1400 UTC (Fig. 3-3f). The convection S2 with Y-shaped

echo was triggered in this warmer area because the outflow of the cold pool near the surface encountered the barrier jet (dashed line in Fig. 3-3f). Moreover, the time series of the temperature field (Fig. 3-3f) shows the cold region evolved from the northwest to the northeast of the domain when the precipitation system approached and landed over northern Taiwan.

3.4 Evolution of Enhanced Barrier jet

The mechanism of the evolved barrier jet is further investigated with the vertical vorticity signature and vertical vorticity budget (tendency, tilting and stretching). Since the horizontal wind are retrieved with at least two radars at each time, and the errors of the retrieved horizontal wind are very small (Liou et al. 2009, see their table 1), it is able to analyse the vertical vorticity quantitatively. The horizontal pattern of 1 km vertical vorticity ($\zeta = \frac{\partial v}{\partial x} - \frac{\partial u}{\partial y}$) at 1400 UTC (Fig. 3-4a) shows that positive (negative) ζ distributed left (right) wing of the barrier jet (blue vector J_1 in Fig. 3-4a). When computing the different terms of the vorticity budget, a positive (negative) vorticity tendency occurs at the right (left) wing of the barrier jet, implying displacement of the barrier jet. In addition, further examination confirms that stretching and tilting dominates the positive vorticity tendency at 1400 UTC (Fig. 3-4b). This feature matches the intense convection and the location of upward motion retrieved by WISSDOM in Fig. 11a. The evolution of the vorticity at the right wing of the barrier jet (J_1) in Fig. 3-4a can be estimated as follows: the vertical vorticity is about $-8*10^{-4}$ s^{-1} and the vorticity tendency in vertical direction is up to $0.5*10^{-6}$ s^{-2}. Assuming the vorticity tendency is constant, the vertical vorticity at the right wing of J_1 would

increase to $2.7*10^{-3}$ s^{-1} over 1.5-hr. The increment ($2.7*10^{-3}$) due to the tendency exceeds the original negative vorticity; hence, the vorticity at the right wing of the barrier jet (J_1) would become positive. The vorticity tendency thus moves the barrier jet inland (east) at 1530 UTC as shown in Fig. 3-4c. The schematic diagram in Fig. 3-4d illustrates the migration and strengthening of the barrier jet. The vertical wind shear shows a horizontal vortex. When the strong convection landed, the barrier jet enhanced by the intense pressure gradient force (from southwest to northeast, Fig. 3-3e) and moved inland by the positive vertical vorticity tendency from tilting and stretching via convective updrafts (blue vector in Fig. 3-4d).

3.5 Schematic diagrams of the extremely heavy rainfall event

Based on this study, the schematic diagram in Fig. 3.5 illustrates the mechanism behind the formation of TS and PS precipitation over northern Taiwan in this case:

(1) As shown in Fig. 3-5a, the Mei-Yu front is accompanied by a MCS (prefrontal precipitation) located over the ocean to the north of Taiwan. At the same time, Taiwan is surrounded by southwesterly flow and the barrier jet already exists along the coast due to orographic effect over Taiwan. The cold outflow of the main precipitation system encounters a warm and humid prevailing wind (southwesterly flow), and then triggers a line convection over the ocean.

(2) When the main precipitation moves southeast and approaches Taiwan, the line convection is pushed by the southwesterly flow and merges with the main precipitation system. In addition, strong convection occurs near the location of the barrier jet, and it strengthens the pressure gradient force (PGF) at low levels. The

PGF is co-located with the barrier jet in the same direction; therefore, the barrier jet is enhanced after the system lands over Taiwan. The upward motion of the strong convection tilts and stretches the horizontal vortex. This mechanism further causes the barrier jet to move east towards the mountain area.

(3) Since the Mei-yu front moves slowly after strong convection occurs inland, a PS-type precipitation is formed (Fig. 3-5b). The strong convection was blocked by orography and thus maintained in the north of Taiwan. In the meantime, the stratiform area produces a wide cold region over north of Taiwan, and the cold outflow encounters the barrier jet and triggers a new line convection. Because the outflow is partially blocked by the orography, the line convection is oriented from southwest to northeast. The main precipitation and new convection then display a Y-shaped echo structure.

(4) The line convection is pushed towards and united with the main precipitation system by the enhanced barrier jet. This feature of the Y-shaped convection can repeat several times when the barrier jet and cold outflow coexist in the right locations. Overall, the locations of the cold pool, barrier jet, orography and the quasi-stationary Mei-Yu front over northern Taiwan form a mechanism to maintain the intensity of the convection and render the precipitation system quasi-stationary. Extremely heavy rainfall can thus occur for an extended period of time in the same area. Once the front moved further south, the outflow due to precipitation no longer coupled well with the barrier jet and this mechanism could not be maintained.

The case was selected from 11 June, 2012, which was affected by the southwesterly air flow and the Meiyu front, resulting in the extreme heavy rainfall in

the northern part as the research and analysis. The rainfall forecast for a frontal case often depends on the position and speed of the front. In this case, the numerical model forecast of the Central Weather Bureau at that time did not capture the extreme rainfall equivalent to the actual rainfall. There are still many unknown factors in the system. We first understand the environmental characteristics and dynamic structure characteristics of extreme rainfall cases, and further improve the forecast deviation of the model itself through the assimilation of convective-scale radar data, and improve short-term quantitative rainfall forecasting.

Chapter 4

Experiments Design and Validation scores

4.1 Experiments design

(a) OSSE experimental design with WRF

The WRF model (Powers et al. 2017; Skamarock et al. 2008) was used to conduct a series of OSSEs. Two-way nesting was configured using a three-layer nested domain. The horizontal resolution was 27 (D01), 9 (D02), and 3 km (D03) with 251 × 261, 337 × 271, and 223 × 232 grid points, respectively (Fig. 4-1). The vertical model contained 51 levels, with the level top at 10 hPa. The parameterization schemes of the model were as follows: the rapid radiative transfer model for the physical parameterization of long-wave radiation (Mlawer et al. 1997); the Dudhia method for short-wave radiation (Dudhia 1989); and the Yonsei University scheme for boundary layer parameterization (Hong et al. 2006). In D01 and D02, the Grell–Dévényi ensemble scheme (Grell and Dévényi 2002) was used for cumulus parameterization; the microphysical GCE scheme was applied in all domains. The 40 members of the ensemble were generated from the WRF–3DVar random perturbations (Barker et al. 2004) in D01 and nested down to 9-km and 3-km resolutions. In this study, all the data were assimilated in the innermost domain (D03), and the changes were propagated through upscaling.

To mimic the actual uncertainty inherent of front position error in this event, two sets of initial conditions were used to differentiate the experiments from the nature run (truth, Exp. 1, Table 4-1) and the control run (NoDA, Exp. 2). The 1° × 1° final operational global analysis (FNL) from the National Centers for Environmental

Prediction (NCEP) for 0000 UTC on 11 June 2012 was applied to all the experimental tests. ERA-interim reanalysis data of a higher resolution (0.75° × 0.75°) were used to initialize the model as the nature run. Figure 4-2 presents the two initial conditions for the nature run (truth, Figs. 4-2a, c) and control run (NoDA, Figs. 4-2b, d). The synoptic features (Figs. 4-2a, b) of the southwestern wind, potential height, and potential temperature near Taiwan were similar in the two reanalysis fields at 850 hPa. However, the water vapor mixing ratio of the ERA-interim reanalysis (Fig. 4-2c) was slightly larger than that of the NCEP FNL (Fig. 4-2d) in the Taiwan area. According to the observations at 1400 UTC (Fig. 3-3c), the rainband of the nature run (Fig. 4-3a) had already landed in Northern Taiwan, whereas the rainband of the control run initialized by NCEP (Fig. 4-3b) was still over the ocean. Furthermore, in terms of the QPF performance (not shown), the forecast initialized by NCEP did not predict heavy rainfall over Northern Taiwan, whereas the simulation initialized by the ERA-interim reanalysis was able to closely reproduce the location and total accumulated rainfall of the surface observations in Northern Taiwan.

(b) Synthetic radar data and thermodynamic variables

To clearly examine the benefit and added value of providing 3D thermodynamic information at the convective scale, we assume that the temperature and humidity observations are obtained from the area of precipitation in the experiments. Therefore, the observation operator in these experiments is the mapping of the true state of temperature and water vapor mixing ratio on the model grid to the observation spaces. The simulated observations were generated from the nature (truth) run. In addition,

considering the uncertainty of the observations, true states were perturbed randomly according to the prescribed observation errors: 5 dBZ for reflectivity (Z) and 3 m s^{-1} for radial wind (Vr) as in Tsai et al. (2014), and 0.8 K for temperature and 0.8 g kg^{-1} for the water vapor mixing ratio. Radar observation data (reflectivity and radial velocity) of two radars in Northern Taiwan were obtained up to a range of 230 km (180 km) from the RCWF (NCU-CPOL) site every 15 minutes by a radar scan strategy as Volume Coverage Pattern (VCP) 221 with nine plan position indicator (PPI) elevations between 0.5° and 19.5°. The superobbing method (Alpert and Kumar 2007; Lindskog et al. 2004) was applied to reduce the simulated observation count in this study. The data points were collected every 4 km in the radial direction and every 4° in the azimuthal direction in the PPI (Fig. 4-4) and then averaged through inverse distance weighting.

(c) Thermodynamic variables retrieved via TPTRS

By taking 3D wind fields from two consecutive (15-min interval) of the true state, the 3D thermodynamic variables (T and Qv) inside the precipitation system were obtained using TPTRS. Figure 4-5 shows that horizontal temperature perturbation at 1400UTC is mainly divided into two blocks, the cold area on the northwest side of the rainfall system and the warm area on the southeast side. At a height of 0.5 km (Figs. 4-5a, b), it can be seen that the retrieved results of the northern cold region of the rainfall system are close to truth, while the retrieval of the warm region shows a warmer situation. At an altitude of 1.0 km (Figs. 4-5c, d), the difference between the retrieval and the truth is less obvious. The difference between the retrieval and the truth mainly exists in the lowest level, which is speculated to be due to the deviation of the lower

level affected by the boundary layer. On the other hand, there is no obvious rainfall system on the southeast side, the deviation of the retrieval system TPTRS in the system less environment is more obvious. A cross-section y-z plane of retrieval temperature perturbation shows warmer in the convection area and cold area than truth in vertical structure.

The vertical structure of the retrieved temperature data (Fig. 4-6a) indicated that the mesoscale warm sector in the convection area and low-level cold pool area was well demonstrated, similar to that in the truth state (Fig. 4-5). The horizontal structure of the retrieved water vapor data at a height of 1.5 km (Fig.4-6) indicated that the wet area in front of the rainband and dry area behind the frontal system were well illustrated. The results of the temperature revealed that the root mean square error (RMSE) in the temperature was less than 0.5 K, and the bias was positive, meaning that the retrieved temperature was slightly warmer than that in the truth state (Fig. 4-6c). The retrieved water vapor results indicated that the overall performance was slightly wetter than truth model, with a correlation of 0.99 and error of 0.56 g kg^{-1} (Fig. 4-6d). In general, the retrievals obtain a good quality of temperature and humidity fields with slightly bias. Therefore, this set of the experiments assumes that the basic state of the temperature and water vapor is error-free and the source of the error is from the perturbations of thermodynamic variables. The observation errors of the retrieved temperature and water vapor were set at 0.8 K and 0.8 g kg^{-1}, respectively (slightly larger than the root mean square error). This setup accords with other studies of thermodynamic retrieval (Foerster and Bell 2017, Liou et al 2003, Liou et al. 2019, Feng et al. 2019).

(d) Experiments setup

The assimilation experiments in this study were conducted in three sets (Table 4-1). In the first set, radar observation data were assimilated for 1 h (Exp. Z assimilated reflectivity only; Exp. Vr assimilated radial wind only; and Exp. ZVr assimilated both radar reflectivity and radial velocity), and then the assimilation period was extended to 2 h (Exp. ZVr2h assimilated both radar reflectivity and radial velocity). In the second set, the thermodynamic field temperature and water vapor generated from the nature run were additionally assimilated (Exp. ZVrT assimilated reflectivity, radial velocity, and temperature; Exp. ZVrQv assimilated radar observations and the humidity field; Exp. ZVrTQv assimilated radar observations and both the temperature and humidity fields; Exp. ZVrTQv2h is an experiment extended assimilation period to 2h from Exp. ZVrTQv). Without any bias, the first and second sets of experiments can investigate the added value of assimilating 3D thermodynamic fields in the severe weather system. In the final set, to mimic bias could be existed in observations retrieved from remote sensing, a retrieved 3D temperature and water vapor information with warm and wet bias from section 3.2 (c) is assimilated (Exp. ZVrTR, Exp. ZVrQvR, and Exp. ZVrTQvR).

The flowcharts for all the experiments are presented in Fig. 4-7. The initial conditions derived from the ERA-interim and NCEP analyses were launched at 0000 UTC on 11 June 2012 and then integrated. The cycled DA started at 1300 (1200) UTC, assimilating observations every 15 min for a 1-h (2-h) assimilation period. Once the final analysis was obtained at 1400 UTC, a 3-h deterministic forecast was initialized using the ensemble mean to examine the QPF performance.

4.2 Validation scores

(a) Ensemble spread (SPD) and Root mean square error (RMSE)

The ensemble spread (*SPD*) are used to estimate the difference in ensemble that is a statistic of the difference between ensemble members and the ensemble mean ($\bar{x}$), N is total members:

$$SPD = \left[\frac{1}{N-1}\sum_{n=1}^{N}(x^n - \bar{x})^2\right]^{1/2} \tag{40}$$

to examine uncertainty of model simulations. When the ensemble spread is small, it means that the model is underdispersive that may limit the effectiveness of assimilating observations in an EnKF. The assimilation results will be biased towards the model without observation data. Conversely, if the ensemble spread is over dispersive, it will cause the mode to fail to converge.

Whereas Root mean square error (RMSE) is the forecast error difference between the ensemble members and the truth (x_t):

$$RMSE = \left[\frac{1}{N-1}\sum_{n=1}^{N}(x^n - x_t)^2\right]^{1/2} \tag{41}$$

In the study, we could have RMSE to validate how impacts of analysis and forecast to close as truth run in OSSEs.

(b) Error Correlation Coefficient (Coor)

The error correlation coefficient is defined by the following equation:

$$Coor(a_{xyz}, b_{lmn}) = \frac{\frac{1}{K-1}\sum_{k=1}^{K}(a_{xyzk} - \overline{a_{xyzk}})\times(b_{lmnk} - \overline{b_{lmnk}})}{\sigma_a \sigma_b} \tag{42}$$

K is total number of ensemble members. To calculate ensemble mean of variable a at location (x, y, z) as *a* reference point. If variable *a* is variable *b*, the *Coor* is called auto-

correlation. On the other hand, it is called cross-correlation. In the study, we calculated auto-correlation that the value of *Coor* is 1 at the reference point.

(c) The relative Spatial Correlation Coefficient (RSCC)

The spatial correlation coefficient (SCC) is defined by the following equation:

$$SCC = \frac{\Sigma_1^N\left((x_{exp}-\overline{x_{exp}})(x_{truth}-\overline{x_{truth}})\right)}{\left[\Sigma_1^N(x_{exp}-\overline{x_{exp}})^2 \cdot \Sigma_1^N(x_{truth}-\overline{x_{truth}})^2\right]^{\frac{1}{2}}} \quad (43)$$

where x refers to the hydrometeor variables (Qr, Qs, or Qg) and exp is an experiment. We define relative *SCC* (*RSCC*) by the following equation:

$$RSSC = \frac{SCC_{exp}-SCC_{ZVr}}{SCC_{ZVr}} \times 100\% \quad (44)$$

If *RSCC* is positive, the experiment has positive improvement compared with Exp. ZVr.

(d) Fractions Skill Score (FSS)

The Fractions Skill Score (*FSS*, Roberts and Lean 2008) is a spatial neighborhood technique, defined by the following equation:

$$FSS = 1 - \frac{\frac{1}{N}\left(P_{fcst}-P_{obs}\right)^2}{\frac{1}{N}\left(\Sigma_N\left(P_{fcst}\right)^2+\Sigma_N(P_{obs})^2\right)} \quad (47)$$

where N is the number of total observation points and P is the probability of achieving a value over a threshold around a grid point. In this study, rainfall accumulation to be verified was 0.01–70 mm, and the range distance was 24 km. If *FSS* is 1, the forecast is accurate. An *FSS* of zero indicates no skill scores were obtained for the rainfall accumulation forecast.

Chapter 5

Result of OSSE and retrieval variables assimilation

5.1 Ensemble background error analysis

Ensemble-based data assimilation uses short-term ensemble forecasts to estimate flow-dependent background error covariance which represents the statistics of forecast error is very important to decide the weighting of observation and spread out the observation information to the vicinity of model grid points.

Before entering the ensemble data assimilation, the characteristics between the ensembles are understood through the ensemble dispersion at 1300 UTC, as shown in Figure 5-1. In the vicinity of the front reflectivity, the reflectivity SPD (Fig. 5-1a) shows dispersion over 25 dBZ at height 2500-m. The spread of potential temperature (Fig. 5-1b) and water vapor mixing ratio (Fig. 5-1c) are about 0.6 K and 0.6 g kg^{-1}, respectively. The SPD of the Qr (rain water) field is relatively scattered, which is close to the rainfall area. The value of the horizontal wind field SPD is about 4 m s^{-1}, and more obvious near the rainfall area what we are concerned about. From the SPD analysis, it can be determined that the observation error value of the assimilation system set in this experiment is similar to the model background error. It is not biased towards the model or the observation, and the assimilation weight is coordinated by the flow-independent between the model and the observation.

Figure 5-2 shows the horizontal distribution of spatial correlation calculated from the variables obtained from the ensemble at 1300 UTC on 2500-m. Autocorrelation is the variable at the single point position in space, and calculate the correlation

distribution with the surrounding space (Fig. 5-2a, b, and c). The radius of the range where the correlation is over 0.7 shows about 40 km in U-wind (Fig. 5-2a) and V-wind (Fig. 5-2b). The range of the autocorrelation is depended on wind direction that U-wind is wider at zonal direction and V-wind is long range at meridional direction. The autocorrelation of water vapor presents a sector-shaped toward southwesterly region (Fig. 5-2c). The area of the temperature correlation 0.7 is around 10-km (Fig. 5-2d). It means we need more dense temperature data to improve data assimilation for the limited correlation area. However, the structure of autocorrelation is not purely homogeneous isotropic background error correlations but it presents situation-dependent correlations in convective-scale system. It can be seen that the spatial distribution of independent variable correlations in meso- and small-scale systems is not a homogenous distribution, and the performance error structure is affected by the environment, system and terrain.

5.2 Performance of the cycling process

The RMSE of reflectivity, radial velocity, temperature and water vapor for Exps. 3-9 were presented in Fig. 5-3 during the assimilation period. The reflectivity error was similar for all the experiments (Fig. 5-3a), except the Exp. Vr. because reflectivity data was not assimilated in this experiment. In only radar assimilation experiments, Exp. ZVr2h shows lower error than other experiments of only assimilation for 1-h (Z, Vr, ZVr). In addition, the experiments of assimilating additional thermodynamic variables presents the best result is the longer assimilation with both T and Qv (Exp. ZVrTQv2h, purple dashed line). On the other hand, the RMSE of radial velocity (Fig. 5-3b) revealed

that the error of Exp. Z was much larger than the other experiments when radial wind information is not assimilated.

The RMSE of temperature and water vapor were presented in Fig. 5-3c and Fig. 5-3d, respectively. When assimilating 3D temperature in Exps. ZVrT, ZVrTQv and ZVrTQv2h, the error of temperature decreased rapidly in the early assimilating period compared to other experiments. In addition, Exp. ZVrQv gradually improved the error of temperature during cycling process and had similar error at the final analysis as Exps. ZVrT, ZVrTQv and ZVrTQv2h. This indicated that via background error covariance in the analysis steps, assimilating water vapor information could improve temperature field. On the other hand, experiments of assimilating radial wind and/or reflectivity (solid lines in Fig. 5-3c) had larger error in the final analysis. Result of Exp. ZVr2h (black dashed line) shows that the error of temperature could not further improve by assimilating radial wind and reflectivity in a longer assimilation period. When examining the RMSE of water vapor, experiments of assimilating radial wind and/or reflectivity (solid lines in Fig. 5-3d) had similar result. Smaller error of water vapor was illustrated when water vapor information was assimilated (green and blue dashed lines in Fig. 5-3d). Assimilating 3D temperature (Exp. ZVrT, red dashed line) could not have similar error of water vapor compared to Exps. ZVrQv and ZVrTQv. Results of Fig 5-3c (blue dashed line) and 5-3d (red dashed line) indicated that assimilating 3D water vapor information was more crucial and effective than assimilating temperature field to obtain optimal analysis.

5.3 Analysis and Short-term forecast of OSSEs

(a) Performance of Final Analysis

Figure 5-4 depicts the convergence field at a height of 1-km (1400 UTC). A strong convergence area was located northwest of Taiwan in the truth state (Fig. 5-4a). However, the convergence field was unclear in NoDA (Fig. 5-4b), indicating a forecast position error. When radar data (radial wind and/or reflectivity) were assimilated in Exps. Z, Vr, ZVr, and ZVr2h, the convergence field demonstrated that the position error had been largely corrected, triggering convection in the appropriate place (Figs. 5-4c–f). In addition, in terms of the intensity of the convergence field (Figs. 5-4c, d, and e), assimilating both radial wind and reflectivity in Exp. ZVr produced a stronger convergence than that in Exp. Z and Exp. Vr. The strength of the convergence field in Exp. ZVr2h (Fig. 5-4f) was the most intense, similar to that in the truth state (Fig. 5-4a). Thus, to obtain the optimal analysis in a multiscale weather system such as a frontal system, increasing the assimilation period is beneficial. However, when assimilating additional information, such as temperature and/or water vapor, for the 1-h assimilation in Exps. ZVrT, ZVrQv, and ZVrTQv (Figs. 5-4g, h, and i), the results revealed that a comparable intensity of the convergence was achieved near the northwest coast (truth, Fig. 5-4a). For 2-h assimilation, ZVrTQv2h (Fig. 5-4j) shows the convergence range are similar as true (Fig. 5-4a) than ZVr2h (Fig. 5-4f) with additional thermodynamic variables information.

The reflectivity at a height of 2.5 km in the final analysis (1400 UTC) for all experiments is illustrated in Fig. 5-5. The assimilation of 1-h radial wind and/or reflectivity data (Figs. 5-5c–e) resulted in the correction of the strong convection

(reflectivity > 40 dBZ) along the coast of northwestern Taiwan. In addition, assimilating both reflectivity and radial wind (Fig. 5-5e) provided a superior rainband structure compared with only assimilating Z (Fig. 5-5c) or Vr (Fig. 5-5d). When Z and Vr were both assimilated for 2 h, as indicated in Fig. 5-5f, the rainband structure was even more similar to that of the nature run (Fig. 5-5a). Thus, longer assimilation lengths for Z and Vr further improved the analysis of the precipitation system. On the other hand, when additional information related to the thermodynamics field was assimilated, the rainband position error and precipitation intensity error were minimized (Figs. 5-3g, h, and i), demonstrating a similar performance to that in Exp. ZVr2h (Fig. 11d). Notably, the result of Exp. ZVrT (Fig. 5-5g) captured the strong convective rainband because of the assimilation of radial wind and reflectivity in 1 h with the addition of temperature. The horizontal reflectivity fields with assimilating additional water vapor show the strong convective line-shaped rainband similar as the result of Exp. ZVrT (Fig. 5-5g). The overestimated reflectivity was also reduced near the north-west area (Exp. ZVrQv, Fig. 5-5i and Exp. ZVrTQv, Fig. 5-5j). The results indicate that providing thermodynamic information shortened the cycling process and assisted in improving the analysis of the strong convective rainband (Figs. 5-5g, h, and i). Moreover, the rainband structure of Exp. ZVrTQv2h is closer to the truth than other experiments.

Figure 5-6 provides a cross section of reflectivity at 1400 UTC in the vertical structure (15 km × 333 km, see the solid line in Fig. 4-3a) across the rainband between 120.75°E–25.93°N and 121.50°E–23.00°N. In the truth state, the reflectivity in Fig. 5-6a clearly demonstrates the structure of the rainband, revealing both a strong convective (Z > 40dBZ at X = 110–150 km) and stratiform (X = 0–110 km) region. Figure 5-6b

depicts the spurious convection (X = 0–10 km) caused by the initial position error from the NoDA. By assimilating reflectivity only (Exp. Z, Fig. 5-6c), the structure of the rainband can be modified to the right location but intensity of Z >40 dBZ in strong convection (X ~111 km) is not as high as the truth. Figure 5-6d reveals the weak convection due to assimilating radial velocity without reflectivity in Exp. Vr. When Z and Vr were both assimilated, the rainband shifted to the correct position (Exp. ZVr, Fig. 5-6e, and Exp. ZVr2h, Fig. 5-6f), and in particular, the area of strong convection was accurately captured. However, because of the initial position error in the background state, relatively strong precipitation (Z = 25–35 dBZ at X = 0–10 km) behind the main precipitation system could not be removed properly, even for the longer assimilation window in Exp. ZVr2h (Fig. 5-6f). The additional temperature and/or humidity information (Figs. 5-6g, h, and i) was able to reduce these incorrect areas of precipitation. In the strong convective area, reflectivity values were above 45 dBZ and close to the truth state when additional thermodynamic variables were assimilated (ZVrT, ZVrQV, and ZVrTQv, Figs. 5-6g, h, and i). The last experiment of ZVrTQv2h (Fig. 5-6j) shows the strong reflectivity values at convective area more similar as truth than ZVr2h (Fig. 5-6f).

We further investigated the cross sections of the vertical velocity and temperature fields, revealing the impact of assimilating thermodynamic variables. Figure 5-7a presents the results of the truth run as a reference. The maximum updraft of the vertical velocity (shaded) was observed near a height of 6 km in the convective area; relative weak vertical velocity was noted in the stratiform area. The temperature perturbation (contours) indicated a warm core (solid lines) at the upper layer in the convection area

and a cold pool (dashed lines) at a low level of 3 km in the stratiform area. In the NoDA, no updraft or cold pool signature was observed (Fig. 5-7b). The assimilation of reflectivity alone in Exp. Z (Fig. 5-7c) sort of reconstructed the upward motions and warm core of the convection, but the results were weaker than those of the truth. At a low level, the negative temperature perturbation revealed that the cold pool was weaker and thinner than that in the truth. According to the stable and stratified features (warm above and cold below, refer to Fig. 5-7a) in the stratiform region, assimilating both reflectivity and radial velocity for 1 h (ZVr, Fig. 5-7e) and 2 h (ZVr2h, Fig. 5-7f) did not suitably modify the vertical temperature structure. Assimilating the thermodynamic information (ZVrT, ZVrQv, ZVrTQv, and ZVrTQv2h, Figs. 5-7g, h, i, and j), by contrast, strengthened the intensity of the vertical velocity (with an upward motion of up to 9 m s^{-1}) and temperature (with positive perturbations of up to 3 K) more effectively than extending the assimilation period (Exp. ZVr2h, Fig. 5-7f). When temperature and/or humidity information (Figs. 5-7g, h, i, and j) was assimilated, the stratiform region could be entirely reconstructed. To explain this result, single observation tests of temperature and horizontal wind are applied in the stratiform area (not shown). The results illustrated that assimilating the temperature field alone propagated the information and adjusted the stratiform area more effectively than solely assimilating the horizontal winds.

In the study, WLRAS allows all variables updated by all simulated observation. Hydrometers are important to affect the reflectivity structure and short-term forecast at the final analysis. Figure 5-8 presents vertical structure of hydrometers of rain, graupel and snow mixing ratio. Examining the vertical structure of the microphysical variables,

Fig. 5-8a shows the mixting ratio of rain (Qr), snow (Qs), and graupel (Qg) and the 0-degree temperature (black line) for Truth. The hydrometers structures of NoDA (Fig. 5-8b) and Exp. Vr (Fig. 5-8d) are not ideal compared to other experiments. There are obvious maximum values of Qr, and Qg in convective area, and Qs in stratifrom upper than 0-degree line. The microphysical variables Qr, and Qg show well structure in convective area but Qs have not been completely corrected in stratiform area in Exp. Z (Fig. 5-8c), Exp. ZVr (Fig. 5-8e), and Exp. ZVr2h (Fig. 5-8f) even after assimilating radar data. However, Exp. ZVrT (Fig. 5-8g), Exp. ZVrQv (Fig. 5-8h), and Exp. ZVrTQv (Fig. 5-8i) present well Qg and Qr at corrective area. In stratiform, the structure of Qs shows wider similar as truth by assimilating additional thermodynamic variables. Hydrometers of Qr, Qs, and Qg are overestimated than truth from Exp. ZVrTQv2h (Fig. 5-8j).

Figure 5-9 is RSCC that presents improvement of each experiment (Exps. ZVr2h, ZVrT, ZVrQv, ZVrTQv and ZVrTQv2h) for the reflectivity-related hydrometeor variables (mixing ratio of rain, graupel, and snow) compared with Exp. ZVr in which Vr and Z were assimilated. The results revealed that all the hydrometeor variables are improved by approximately 10% when the assimilation period was extended. Assimilating temperature information led to additional improvements for the mixing ratios of graupel and snow. However, when humidity was assimilated with radial wind and reflectivity, the mixing ratios of rain, graupel, and snow are improved by more than 20%. In particular, the mixing ratio of rain exhibited a more than 40% improvement when assimilating water vapor (ZVrQv and ZVrTQv). Thus, radar DA with additional thermodynamic variables also improved the distribution of hydrometeor variables when

warm core and cold pool are better reproduced in the final analysis. The best experiment is Exp. ZVrTQv2h that the RSCC score are all over than 0.3.

(b) Performance of short-term forecast

The short-term forecast was launched by the ensemble mean analysis at 1400 UTC, and the results of 1-h (Fig. 5-10) and 3-h (Fig. 5-11) accumulated rainfall.

In a 1-h rainfall short-term forecast, the truth presents the rainfall accumulation area as a rainband across northern Taiwan, and the maximum value is over 50-mm (Fig. 5-10a). For experiments on assimilating radar data, Exp. Vr (Fig. 5-10d) shows a wider rainfall area than Exp. Z (Fig. 5-10c). Both assimilating Z and Vr, the rainfall forecast is better in the case study but Exp. ZVr2h is similar to Exp. ZVr even with one more one-hour assimilation of radar data. For the experiments of assimilating thermodynamic variables, all of the four experiments of Exp. ZVrT (Fig. 5-10g), Exp. ZVrQv (Fig. 5-10h), Exp. ZVrTQv (Fig. 5-10i) and Exp. ZVrTQv2h (Fig. 5-10j), the rainfall in the first hour presents a good structure in the rainband and the value is over 50 mm closed to the truth. The best result is Exp. ZVrTQv2h (Fig. 5-10j) because including more thermodynamic information at an early stage than Exp. ZVr2h (Fig. 5-10f).

The truth state in Fig. 5-11a reveals extreme heavy rainfall along the coast of northern Taiwan. The rainfall accumulation in NoDA (Fig. 5-11b) was low, and the area of precipitation was over the ocean because this experiment employed the mean forecast from the random perturbations without DA. Figures 5-11c and d present the results of rainfall accumulation when only one set of radar data (reflectivity or radial velocity) was assimilated. The rainfall position in northern Taiwan was more accurate

in the truth state than in the NoDA run (Fig. 5-11b), but the rainfall accumulation was not sufficient to obtain a heavy rainfall signature. The results of Exp. ZVr (Fig. 5-11e) and Exp. ZVr2h (Fig. 5-11f) displayed the correct position of the total accumulated rainfall. Exp. ZVr2h demonstrated a higher level of rainfall accumulation in northern Taiwan because of the use of a longer assimilation period than in Exp. ZVr. More observation information for model assimilation had a positive impact on the QPF, but the intensity of the precipitation was weaker than that in the truth (Fig. 5-11a). On the other hand, the QPF is improved when the thermodynamic variables were assimilated (Figs. 5-11g, h, and i). Figure 5-11g (Exp. ZVrT) depicts the rainfall accumulation area, revealing improved values compared with ZVr2h (Fig. 5-11f). Thus, the additional temperature information shortened the spin-up assimilation period. In Exp. ZVrQv and Exp. ZVrTQv in which humidity information is assimilated (Fig. 5-11h), the location and intensity of the rainfall were very close to the truth and the overestimation of rainfall in the northwest was mitigated. For the last experiment, ZVrQv2h (Fig. 5-11j), assimilating both temperature and humidity for 2 hours, the coverage and intensity of the rainfall were the best performance presented in rainfall over 90-mm among all experiments.

We check the FSSs of the short-term forecast for 1 (Fig. 5-12a), 3 (Fig. 5-12b), and 6 (Fig. 5-12c) h accumulated rainfall. FSS of Exp. Vr are higher than Exp. Z, and the dynamic information is more important to maintain weather system for a good rainfall forecast. Exp. ZVr2h shows clearly skill score than the experiment with only one-hour radar assimilation. The experiments with water vapor are better than experiment with temperature for the rainfall forecast. This also highlights that water

vapor is key to prolonging the rainfall forecast results in the frontal event in this study. The first hour rainfall forecast skill score FSS shows higher score of experiments with temperature and water vapor (Exp. ZVrT, ZVrQv, and ZVrTQv) than Exp. ZVr2h (Fig. 5-12a). This result revealed that adding 3D temperature assimilation improved the performance of radar DA for short-term rainfall forecasting and shortened the spin-up assimilation period from 2 to 1 h. The best result is Exp. ZVrTQv2h that shows the skill score higher than 0.3 till forecast 6-h by assimilating more thermodynamic variables (Fig. 5-12c).

5.4 Results of retrieval variables assimilation

(a) Performance of analysis

Temperature and water vapor information are retrieved from model truth (Exp.1) by the retrieval algorithm TPTRS (Section 4.1c). The three experiments as ZVrTR, ZVrQvR, and ZVrTQvR are listed in Table 4-1. Figures 5-13a–c present the low-level convergence fields in the final analysis (1400 UTC). The convergence of Exp. ZVrTR revealed comparable intensity as Exp. ZVrT and better than Exp. ZVr2h. The reflectivity field in Fig. 5-13d shows that the intensity of the strong convective is similar as Exp. ZVrT and the truth state in northern Taiwan, but the line-shaped convective rainband is not broadening enough. In Exp. ZVrQvR, the convergence (Fig. 5-13b) inland was weaker than Exp. ZVrQv (Fig. 5-13h) and Exp. ZVrTR (Fig. 17a). Besides, the simulated reflectivity (Fig. 5-13e) shows similar intensity and pattern as Exp. ZVrTR. In Exp. ZVrTQvR, the convergence (Fig. 5-14c) is similar to Exp. ZVrTR and Exp. ZVrQvR, but a better rainband coverage and pattern in Fig. 5-13f was illustrated.

Simulated reflectivity in Fig. 5-13f shows that the analysis could better represent the line-shaped area as truth (Fig. 5-5a). The optimal results for convergence and reflectivity among the three experiments come from Exp. ZVrTQvR.

Figures 5-13g-i reveal the cross section of vertical velocity and temperature fields as Fig. 5-7. In the experiment that only assimilated retrieved temperature with radar (Exp. ZVrTR, Fig. 5-13g), the upward motion was stronger (up to 8 m s^{-1}) than the other two experiments (Exp. ZVrQvR and Exp. ZVrTQvR). The temperature perturbation revealed the warm core at the mid-level as the truth (Fig. 5-7a), but the cold pool at the low level was distributed in a smaller region compared to the truth and Exp. ZVrT because the retrieved temperature has warm bias as mentioned in Section 4.1c. By assimilating water vapor only (Exp. ZVrQvR, Fig. 5-13h), the warm core and upward motion were weaker than Exp. ZVrTR at mid-level (Fig. 5-13g). On the other hand, the structure of temperature perturbation showed a better distribution of the cold pool as Exp. ZVrQv at the low level. The optimal result of temperature perturbation comes from Exp. ZVrTQvR (Fig. 5-13i). The results revealed that the cold pool at the low level and the warm core in the mid-level were close to the truth (Fig. 5-7a). Among the three experiments, assimilating retrieved temperature enhanced the warm core structure at the mid-level and strengthens the upward motion in strong convection areas. In contrast, assimilating retrieved water vapor improved the intensity of cold pools near the surface. Overall, the results demonstrated that assimilated retrieved thermodynamic fields had a positive impact on the final analysis of the severe weather system.

(b) Performance of short-term forecast

By launching the model from the ensemble mean of final analysis in Section 4.4a, the benefit of assimilating retrieved thermodynamic information for the QPF was examined. For the 1-h and 3-h total accumulated rainfall, ZVrTR (Figs. 5-14a, c) can produce the local maximum rainfall over 50 mm. Even though the retrieved temperature field has the warm bias compared with the truth, ZVrTR can better predict the local maximum of the heavy rainfall with shorter DA period (1-h) compared with ZVr2h (Fig. 5-10f). This is due to the warm core at mid-level and more intense upward motion in the final analysis. In Exp. ZVrQvR, more precipitation occurred in the first hour (Fig. 5-14e), but the amount of precipitation was less than the truth state (Fig. 5-10a) and the Exp. ZVrQv (Fig.5-11h) for 3-h QPF. The optimal result comes from Exp. ZVrTQvR (Figs. 5-14c, f). The accumulated rainfall revealed a well line-shaped pattern and coverage as the truth over northern Taiwan. In addition, the amount of the precipitation was up to 70 mm though it was underestimated compared to the truth state (Fig. 5-10a, Fig. 5-11a). The feasibility study shows that when assimilating the retrieved thermodynamic fields with bias, providing temperature information has more QPF improvement than assimilating retrieved water vapor. This is because more intense upward motion and warm core are reproduced in the analysis when assimilating retrieved temperature. Overall, when both retrieved temperature and water vapor are assimilated, the result can still improve the QPF and outperform Exp. ZVr2h.

The FSSs of the short-term forecast for 1, 3, and 6 h accumulated rainfall was displayed in Fig. 5-15. Among the three experiments, assimilating additional retrieved temperature with radar data (Exp. ZVrTR) showed much more improvements of the

short-term forecast in the first hour of the QPF (Fig. 5-15a), resulting in the highest FSS. This was due to the warm core at mid-level and more intense upward motion effected by the retrieved temperature with warm bias. For 3-h forecast (Fig. 5-15b), the FSS showed the benefit of assimilating both retrieval temperature and water vapor (Exp. ZVrTQvR), especially in the heavy rainfall condition (thershold over 30 mm). When both retrieved temperature and water vapor are assimilated, the result shows the best impact to improve the QPF after 3-h. For 6-h rainfall forecast, FSS of Exp. ZVrTQvR shows improvement than the experiment of assimilated only temperature or water vapor.

Chapter 6

Conclusions and Future Work

6.1 Conclusions

An extremely heavy rainfall occurring on 11 June 2012 during the Mei-Yu season was investigated in this study. By using multiple Doppler radar observations, wind, pressure, and temperature fields were retrieved in time and space in order to examine the interaction of dynamics, thermodynamics, and terrain effect on the mesoscale and convective scale. The precipitation system is divided into three phases, and the evolution of the barrier jets at the convective scale is revealed for the first time by analysing the migration and intensity of the barrier jet within the first 4 hours when the heavy rainfall took place.

At the first stage (TS-type), typical mesoscale convection occurred south of the front, and the retrievals presented a squall-line structure when the system remained over the ocean in the north of Taiwan. The horizontal wind at low levels demonstrated that a barrier jet had already appeared along the west coast at this stage. A line convection initialized by south-westerly flow developed and merged with the main precipitation system. The system landed over northern Taiwan and went through a transition period at the second stage: strong connection with upward motion inland favoured the eastward displacement of the barrier jet. In the meantime, thermodynamic retrievals illustrated a strengthened meso-low located inland of northern Taiwan, and the pressure gradient force enhanced the intensity of the barrier jet. At the third stage (PS-type), the location of the cold pool and the orography over northern Taiwan act as obstacles. When

the cold outflow encounters the barrier jet, Y-shaped echo convection appeared at the cold pool outflow convergence zone and then united to the main convection. These features formed a favourable condition to maintain a strong convection around the same location and cause extremely heavy rainfalls in a short period of time.

In this study, we examined the impacts of assimilating 3D thermodynamic fields with radar data (radial wind and reflectivity). A series of OSSEs were designed, and three sets of DA experiments were conducted using the WLRAS ensemble DA system. Different types of thermodynamic variables were obtained from the truth state or retrieved from the TPTRS retrieval algorithm. A frontal system that brought extremely heavy rainfall to Northern Taiwan on 11 June 2012 was investigated. The results of both analysis and very short-term forecast were examined through the three sets of experiments, resulting in the following conclusions:

(1) In this particular case, which clearly demonstrated a precipitation position error in the background, assimilating radar observations of radial wind and reflectivity promptly corrected or reduced the position error of the convergence zone and rain bands. In addition, when dealing with a multiscale weather system, such as the frontal system in this study, increasing the assimilation period helped improve the analysis and short-term forecast. However, improvements in the analysis of the stratiform area were limited and the 6-h QPF was underestimated.

(2) In the OSSEs, providing additional information regarding the unbiased temperature and/or humidity fields in the multiscale precipitation system shortened the spin-up assimilation period as expected. In addition, the upward motion and warm core in the mid-level and the cold pool in the stratiform areas were more improved through

additional thermodynamic variables than through additional cycles of radial wind and reflectivity assimilation. The improvement in the stratiform region further benefited the hydrometeor variables, which were strongly associated with the vertical structure of temperature. The results demonstrated that assimilating thermodynamic variables achieved greater improvements (0–6 h) in extremely heavy rainfall prediction than when only assimilating radar data. In addition, assimilating humidity information alone yielded a stronger accumulated rainfall performance than assimilating the 3D temperature field alone.

(3) In the study, we discuss the feasibility of assimilating retrieval 3D thermodynamic with radar data. When the biased thermodynamic fields were obtained by a retrieval algorithm, assimilating temperature information reproduced a stronger upward motion and warm core at the convective area of the final analysis, and improved the very short-term QPF at the first hour. Assimilating humidity field helped to reconstruct the coverage and intensity of the cold pool near the surface. The optimal result is to assimilate the 3D thermodynamic fields both temperature and water vapor that could shorten a spin-up assimilation period to improve the QPF up to 6 hours.

6.2 Future work

This study uses retrieval algorithm WISSDOM and TPTRS to analyze the mechanism of frontal heavy rainfall and the interaction between the evolution of the barrier jet and topography. The retrieval information is adding to the radar data assimilation system to study whether the thermodynamic retrieval information can

improve the structure of the model initial condition and the ability of rainfall forecast. Although the results show a positive impact, there are still issues that we can continue to explore.

(1) Carefully understand the causes of the thermal retrieval structure, discuss the relationship between temperature and microphysics, and the related configuration of pressure field and wind field. It is expected that by explaining the state of the system under static and non-static conditions, we can have more confidence in the retrieval results from TPTRS,

(2) Carefully compare the differences between the dynamic and thermodynamic fields of the retrieved 3D information and the truth simulated by the model. Check whether the interaction between the barrier jet and the complex terrain is consistent at the small scales, and provide an analytical basis for the quality of the assimilation results. In the future, the differences between the model and actual observations can be explored the key influencing factors can be identified, and the main points of the model to improve the small-scale simulation can be provided.

(3) A more in-depth discussion and explanation of the phenomenon of warm deviations in the retrieval temperature results and warm bias in the water vapor are carried out. After it is added to the radar data assimilation system, the resulting factors still need to be discussed more carefully.

(4) Whether different microphysical schemes will cause changes in the results of assimilating thermodynamic variables is a topic worthy of discussion in the future.

(5) The research of real cases will encounter the problem of duplication of retrieval data and radar data. In the future, different interpolation methods can be used to generate data misalignment to avoid this problem.

Overall, this study demonstrated that assimilating 3D thermodynamic fields in addition to radial wind and reflectivity was important and crucial to improve the analysis and QPF for convective weather systems. In addition, it was possible to assimilate 3D thermodynamic fields from scanning weather radars. In the study, thermodynamic variables are temperature and mixing ratio of water vapor. Thermodynamic variables could be represented as virtual temperature, potential temperature, equivalent potential temperature, relative humidity, … etc. We can study which variables are efficiently to improve numerical model analysis and QPF. As a next step, we are preparing to assimilate the following information in the WLRAS: (1) low-level information from surface observations and (2) humidity information from radar refractivity and/or dual-wavelength retrievals. The evaluation and verification of QPFs will be examined with real cases of severe weather systems such as typhoons and thunderstorms.

References

邵彥銘，2015：利用局地系集轉換卡爾曼濾波器雷達資料同化系統改善短期定量降雨預報：SoWMEX IOP8 個案分析。國立中央大學，大氣物理研究所，碩士論文。

吳品穎，2015: 利用系集重新定位法改善對流尺度定量降水即時 預報：2009 年莫拉克颱風個案研究，國立中央大學，大氣物理研究所，碩士論文

鄭翔文，2017:雷達資料同化於多重尺度天氣系統(梅雨)的 強降雨預報影響：SoWMEX IOP#8 個案研究，國立中央大學，大氣物理研究所，碩士論文

Alpert, J. C., and V. K. Kumar, 2007: Radial Wind Super-Obs from the WSR-88D Radars in the NCEP Operational Assimilation System. Mon. Wea. Rev., 135, 1090-1109.

Aksoy, A., D. C. Dowell, and C. Snyder, 2010: A Multicase Comparative Assessment of the Ensemble Kalman Filter for Assimilation of Radar Observations. Part II: Short-Range Ensemble Forecasts. *Mon. Wea. Rev.*,**138**, 1273-1292.

Anderson, J. L., 2001: An ensemble adjustment Kalman filter for data assimilation. *Mon. Wea. Rev.*, **129**, 2884-2903

Arnold Jr., C. P., and C. H. Dey, 1986: Observing-systems simulation experiments: Past, present, and future. *B. Am. Meteor. Soc.*, **67**, 687-695.

Barker, D. M., W. Huang, Y.-R. Guo, A. J. Bourgeois, and Q. N. Xiao, 2004: A three-dimensional variational data as- similation system for use with MM5: Implementation and initial results. *Mon. Wea. Rev.*, **132**, 897–914.

Benjamin, S. G., G. A. Grell, J. M. Brown, T. G. Smirnova, and R. Bleck, 2004: Mesoscale weather prediction with the RUC hybrid isentropic–terrain-following coordinate model. *Mon. Wea. Rev.*, **132**, 473–494.

——, and Coauthors, 2016: A North American hourly assimilation and model forecast cycle: The Rapid Refresh. *Mon. Wea. Rev*., **144**, 1669–1694

Bishop, C. H., B. J. Etherton, and S. J. Majumdar, 2001: Adaptive sampling with the ensemble transform Kalman filter. Part I: Theoretical aspects. *Mon. Wea. Rev.*, **129**, 420-436.

Browning, K. A., C. G. Collier, P. R. Larke, P. Menmuir, G. A. Monk, and R. G. Owens, 1982: On the forecasting of frontal rain using a weather radar network. *Mon. Wea. Rev.*, **110**, 534-552.

Bouttier, F., 1994: A dynamical estimation of forecast error covariances in an assimilation system. *Mon. Wea. Rev*., **122**, 2376-2390.

Carlin, J. T., J. Gao, J. C. Snyder, and A. V. Ryzhkov, 2017: Assimilation of ZDR Columns for Improving the Spinup and Forecast of Convective Storms in Storm-Scale Models: Proof-of-Concept Experiments. *Mon. Wea. Rev*., **145**, 5033-5057.

Caumont, O., V. Ducrocq, É. Wattrelot, G. Jaubert, and S. Pradier-Vabre, 2010: 1D+3DVar assimilation of radar reflectivity data: A proof of concept. *Tellus A*, **62**, 173–187.

——, and Coauthors, 2016: Assimilation of humidity and temperature observations retrieved from ground-based microwave radiometers into a convective-scale NWP model. Quart. J. Roy. Meteor. Soc., 142, 2692-2704.

Caya, A., J. Sun, and C. Snyder, 2005: A comparison between the 4DVAR and the ensemble Kalman filter techniques for radar data assimilation. *Mon. Wea. Rev.*, **133**, 3081-3094.

Chang, S.-F., J. Sun, Y.-C. Liou, S.-L. Tai, and C.-Y. Yang, 2014a: The influence of erroneous background, beam-blocking and microphysical nonlinearity on the application of a fourdimensional variational Doppler radar data assimilation system for quantitative precipitation forecasts. Meteor. Appl., 21, 444–458.

——, Y.-C. Liou, J. Sun, and S.-L. Tai, 2016: The Implementation of the Ice-Phase Microphysical Process into a Four-Dimensional Variational Doppler Radar Analysis System (VDRAS) and Its Impact on Parameter Retrieval and Quantitative Precipitation Nowcasting. *J. Atmos. Sci*., **73**, 1015–1038.

Chen, Y.-L., Y.-J. Chu, C.-S. Chen, C.-C. Tu, J.-H. Teng, and P.-L. Lin, 2018: Analysis and Simulations of a Heavy Rainfall Event over Northern Taiwan during 11–12 June 2012. *Mon. Wea. Rev.*, **146,** 2697-2715

Chung, K.-S., W. Chang, L. Fillion, and M. Tanguay, 2013: Examination of situation-dependent background error covariances at the convective scale in the context of the ensemble Kalman filter. *Mon. Wea. Rev.*, **141**, 3369–3387.

Deng, T.-W., Chen, C.-S. and Wang Chen, T.-C. 1992. Analysis of synopic environment and precipitation characteristics for heavy rain case on 9 June, 1990. Atmospheric Science 20, 79–118 (in Chinese)

Do, Phuong-Nghi, K.-S. Chung, P.-L. Lin, C.-Y. Ke, and S. M. Ellis: Assimilating Retrieved Water Vapor and Radar Data From NCAR S-PolKa: Performance and

Validation Using Real Cases. *Mon. Wea. Rev.*, **150**, 1177–1199

Dowell, D. C., L. J. Wicker, and C. Snyder, 2011: Ensemble Kalman filter assimilation of radar observations of the 8 May 2003 Oklahoma City supercell: Influences of reflectivity observations on storm-scale analyses. *Mon. Wea. Rev.*,**139**, 272–294.

Dudhia, J., 1989: Numerical study of convection observed during the Winter Monsoon Experiment using a mesoscale two–dimensional model. *J. Atmos. Sci.*, **46**, 3077–3107.

Ellis, S. M. and Vivekanandan, J.: Liquid water content estimates using simultaneous S and Ka-band radar measurements, *Radio Sci*., **46**, RS2021.

Evensen, G., 1994: Sequential data assimilation with a nonlinear quasi-geostrophic model using Monte Carlo methods to forecast error statistics. *J. Geophys. Res.*, **99**, 10143-10162

Fabry, F., C. Frush, I. Zawadzki, and A. Kilambi, 1997: On the extraction of near-surface index of refraction using radar phase measurements from ground targets. *J. Atmos. Oceanic Technol.*, **14**, 978–987.

Feng, Y.-C., and F. Fabry, 2016: The imperfect phase pattern of real parabolic radar antenna and data quality. *J. Atmos. Oceanic Technol.*, **33**, 2655–2661.

——, H.-W. Hsu, P.-L. Lin, Y.-C. Liou, T. Weckwerth, 2019: T The characteristics and application of radar refractivity in tropical coastal region. 39th International Conference on Radar Meteorology, 15-20 September 2019, Nara, Japan, *Amer. Meteor. Soc.*, 13A-02

Foerster, A. M., and M. M. Bell, 2017: Thermodynamic retrieval in rapidly rotating vortices from multiple-Doppler radar data. *J. Atmos. Oceanic Technol.*, **34**, 2353–2374.

Gao, J. and David J. Stensrud, 2014: Some Observing System Simulation Experiments with a Hybrid 3DEnVAR System for Storm-Scale Radar Data Assimilation. *Mon. Wea. Rev.*, **142**, 3326–3346.

Gasperoni, N. A., M. Xue, R. D. Palmer, and J. Gao, 2013: Sensitivity of convective initiation prediction to near-surface moisture when assimilating radar refractivity: Impact tests using OSSEs. *J. Atmos. Oceanic Technol*., **30**, 2281–2302.

Ge, G., J. Gao, and M. Xue, 2013: Impacts of Assimilating Measurements of Different State Variables with a SimulatedSupercell Storm and Three-Dimensional Variational Method. *Mon. Wea. Rev.*,**141**, 2759-2777.

Germann, U., and I. Zawadzki, 2002: Scale-dependence of the predictability of precipitation from continental radar images. Part I: Description of the methodology. *Mon. Wea. Rev.*, **130**, 2859-2873.

Grell, G. A., and D. Dévényi, 2002: A generalized approach to parameterizing convection combining ensemble and data assimilation techniques. *Geophysical Research Letters*, **29**, 38-31-38-34.

Greybush, S. J., E. Kalnay, T. Miyoshi, K. Ide, and B. R. Hunt, 2011: Balance and ensemble Kalman filter localization techniques. *Mon. Wea. Rev.*, **139**, 511-522.

Hamill, T. M., and C. Snyder, 2000: A hybrid ensemble Kalman filter-3D variational analysis scheme. *Mon. Wea. Rev*., **128**, 2905-2919.

Hong, S.-Y., Noh, Y. and Dudhia, J. 2006. A new vertical diffusion package with an explicit treatment of entrainment processes. *Mon. Wea. Rev.* **134**, 2318-2341.

Hunt, B. R., E. J. Kostelich, and I. Szunyogh, 2007: Efficient data assimilation for spatiotemporal chaos: a local ensemble transform Kalman filter. *Physica D*, **230**, 112-126.

Jacques, D., D. Michelson, J.-F. Caron, L. Fillion, 2018: Latent Heat Nudging in the Canadian Regional Deterministic Prediction System. *Mon. Wea. Rev*., **146**, 3995-4014.

Ke, C.-Y., K.-S. Chung, T.-C. Chen Wang, and Y.-C. Liou, 2019: Analysis of heavy rainfall and barrier-jet evolution during Mei-Yu season using multiple Doppler radar retrievals: a case study on 11 June 2012. *Tellus A: Dynamic Meteorology and Oceanography*, **71**, 1-21.

Kerr, C. A., D. J. Stensrud, and X. Wang, 2015: Assimilation of cloud-top temperature and radar observations of an idealized splitting supercell using an observing system simulation experiment. *Mon. Wea. Rev*., **143**, 1018–1034.

Lai, A., and Coauthors, 2019: Assimilation of Radar Radial Velocity, Reflectivity and Pseudo Water Vapor for Convective-scale NWP in a Variational Framework. *Mon. Wea. Rev*. **147**, 2877–2900.

Lee, J.-T., Lee, D.-I., You, C.-H., Uyeda, H., Liou, Y.-C. and co-authors. 2014. Dual-Doppler radar analysis of a near shore line-shaped convective system on 27 July 2011, Korea: a case study. *Tellus Dyn. Meteorol. Oceanograph*. **66**, 100–200

Li, J., Chen, Y. L. and Lee, W. C. 1997. Analysis of a heavy rainfall event during

TAMEX. *Mon. Wea. Rev.,* **125**, 1060–1082.

Li, Y., X. Wang, and M. Xue, 2012: Assimilation of Radar Radial Velocity Data with the WRF Hybrid Ensemble–3DVAR System for the Prediction of Hurricane Ike (2008). *Mon. Wea. Rev.*, **140**, 3507–3524.

Lindskog, M., K. Salonen, H. Ja¨ rvinen, and D. B. Michelson, 2004: Doppler radar wind data assimilation with HIRLAM 3DVAR. *Mon. Wea. Rev.*, **132**, 1081-1092.

Liou, Y.-C., 2001: The derivation of absolute potential temperature perturbations and pressure gradients from wind measurements in three dimensional space. *J. Atmos. Oceanic Technol.,* **18**, 577–590.

——, T.-C. Chen Wang, and K.-S., Chung, 2003, A three-dimensional variational approach for deriving the thermodynamic structure using Doppler wind observations – An application to a subtropical squall line, *J. Appl. Meteo*., **42**, 1443-1454.

——, and Chang, Y. J. 2009. A variational multiple Doppler radar three-dimensional wind synthesis method and its impacts on thermodynamic retrieval. *Mon. Wea. Rev.* **137,** 3992–4010.

——, Chang, S.-F. and Sun, J. 2012. An application of the immersed boundary method for recovering the three dimensional wind fields over complex Terrain using multiple Doppler radar data. *Mon. Wea. Rev*. **140**, 1603–1619.

——, J.-L.Chiou, W.-H.Chen, and H.-Y. Yu, 2014: Improving the Model Convective Storm Quantitative Precipitation Nowcasting byAssimilating State Variables Retrieved from Multiple-Doppler Radar Observations.Method.*Mon. Wea.*

Rev.,**142**, 4017-4035

——, Wang, T. C. C. and Huang, P. Y. 2016. The inland eyewall reintensification of Typhoon Fanapi (2010) documented from an observational perspective using multiple Doppler radar and surface measurements. *Mon. Wea. Rev.* **144,** 241–261

——, P.-C. Yang, and W.-Y., Wang, 2019: Thermodynamic recovery of the pressure and temperature fields over complex terrain using wind fields derived by multiple Doppler radar synthesis. *Mon. Wea. Rev.*, **147**, 3843–3857

Mandapaka, P. V., U. Germann, L. Panziera, and A. Hering, 2012: Can Lagrangian extrapolation of radar fields be used for precipitation nowcasting over complex Alpine orography?. *Wea. Forecasting*, **27**, 28-49.

Marshall, J. S., and W. McK. Palmer, 1948: The distribution of raindrops with size. *J. Meteor.,* **5**, 165-166.

Ménétrier, B., T. Montmerle, Y. Michel, and L. Berre, 2015: Linear filtering of sample covariances for ensemble-based data assimilation. Part I: Optimality criteria and application to variance filtering and covariance localization. *Mon. Wea. Rev.,* **143**, 1622–1643.

Miyoshi, T., Y. Sato, and T. Kadowaki, 2010: Ensemble Kalman filter and 4D-Var intercomparison with the Japanese operational global analysis and prediction system. *Mon. Wea. Rev.*, **138**, 2846-2866.

Mlawer, E. J., S. J. Taubman, P. D. Brown, M. J. Iacono, and S. A. Clough, 1997: Radiative transfer for inhomogeneous atmospheres: RRTM, a validated correlated-k model for the longwave. *Journal of Geophysical Research:*

Atmospheres, **102**, 16663-16682.

Montmerle, T., A. Caya, and I. Zawadzki, 2002: Short-term numerical forecasting of a shallow storms complex using bistatic and single-Doppler radar data. *Wea. Forecasting,* **17**, 1211–1225.

Nicol, J. C., and A. J. Illingworth, 2013: The effect of phase-correlated returns and spatial smoothing on the accuracy of radar refractivity retrievals. *J. Atmos. Oceanic Technol*., **30**, 22–39.

——, ——, and K. Bartholomew, 2014: The potential of 1 h refractivity changes from an operational C-band magnetron-based radar for numerical weather prediction validation and data assimilation. *Quart. J. Roy. Meteor. Soc.*, **140**, 1209–1218.

Ott, E., and Coauthors, 2004: A local ensemble Kalman filter for atmospheric data assimilation. *Tellus*, **56A**, 415–428.

Parker, M. D. and Johnson, R. H. 2000. Organizational modes f midlatitude mesoscale convective systems. *Mon. Wea. Rev.,* **128**, 3413–3436.

Powers, J. G., and Coauthors, 2017: The Weather Research and Forecasting Model: Overview, System Efforts, and Future Directions. *Bulletin of the American Meteorological Society*, **98**, 1717-1737.

Roberts, N. M., and H. W. Lean, 2008: Scale-selective verification of rainfall accumulations from high-resolution forecasts of convective events. *Mon. Weather Rev.*, **136**, 78–97.

Seko, H., E.-I. Sato, H. Yamauchi, and T. Tsuda, 2017: Data assimilation experiments

of refractivity observed by JMA operational radar. *Data Assimilation for Atmospheric, Oceanic and Hydrologic Applications (Vol. III),* S. K. Park and L. Xu, Eds., Springer, 327–336.

Skamarock, W. C., and Coauthors, 2008: A Description of the Advanced Research WRF Version 3. *NCAR Tech*. Note NCAR/TN-475+STR, 113 pp.

Snyder, C., and F. Zhang, 2003: Assimilation of simulated Dopplerradar observations with an ensemble Kalman filter. *Mon. Wea.Rev.*, *131*, 1663–1677.

Sugimoto, S., N. A. Crook, J. Sun, Q. Xiao, and D. M. Barker, 2009: An examination of WRF 3DVAR radar data assimilation on its capability in retrieving unobserved variables and forecasting precipitation through Observing System Simulation Experiments. *Mon. Wea. Rev.*, **137**, 4011-4029

Sun, J., and N. A. Crook, 1997: Dynamical and microphysical retrieval from Doppler radar observations using a cloud model and its adjoint. Part I: Model development and simulated data experiments. *J. Atmos. Sci.*, **54**, 1642-1661

——, and ——, 2001: Real-time low-level wind and temperature analysis using single WSR-88D data. *Wea. Forecasting*, **16**, 117– 132.

Tai, S.-L., Y.-C. Liou, J. Sun, and S.-F. Chang, 2017: The Development of a Terrain-Resolving Scheme for the Forward Model and Its Adjoint in the Four-Dimensional Variational Doppler Radar Analysis System (VDRAS). *Mon. Wea. Rev.*, **145**, 289-306.

Tao, W. K., and Coauthors, 2003: Microphysics, radiation and surface processes in the Goddard Cumulus Ensemble (GCE) model. *Meteorology and Atmospheric*

Physics, **82**, 97-137.

Themens, D., and F. Fabry, 2014: Why Scanning Instruments Are a Necessity for Constraining Temperature and Humidity Fields in the Lower Atmosphere. *J. Atmos. Oceanic Technol.*, **31**, 2462-2481.

Tong, M., and M. Xue, 2005: Ensemble Kalman filter assimilation of Doppler radar data with a compressible nonhydrostatic model: OSS experiments. *Mon. Wea. Rev.*, **133**, 1789–1807

Tsai, C.-C., S.-C.Yang, and Y.-C. Liou, 2014:Improving quantitative precipitation nowcasting with a local ensemble transform Kalman filter radar data assimilation system: Observing system simulation experiments. *Tellus A*, **66**, 21804.

Wang, T.-C., Lin, P.-L. and Chen, C.-S. 1991. Radar analysis of a flash-flood producing mesoscale convective system in 1990 Mei-Yu season of Taiwan. Conference on Weather Analysis and Forecasting 1991, Taipei, Taiwan, Central Weather Bureau (in Chinese).

Wang, X., C. Snyder, and T. M. Hamill, 2007: On the theoretical equivalence of differently proposed ensemble-3DVAR hybrid analysis schemes. *Mon. Wea. Rev.*, **135**, 222-227.

Wattrelot, E., O. Caumont, and J.-F. Mahfouf, 2014: Operational implementation of the 1D+3D-Var assimilation method of radar reflectivity data in the AROME model. *Mon. Wea. Rev*., **142**, 1852–1873.

Whitaker, J. S., and T. M. Hamill, 2002: Ensemble data assimilation without perturbed observations. *Mon. Wea. Rev.*, **130**, 1913-1924.

Xiao, Q., Y.-H.Kuo, J. Sun, W.-C.Lee, E. Lim, Y.-R.Guo and D. M. Barker, 2005: Assimilation of Doppler radar observations with a regional 3DVAR system: Impact of Doppler velocities on forecasts of a heavy rainfall case. *J. Appl. Meteor.*, **44**, 768-788.

——, and J. Sun, 2007: Multiple-radar data assimilation and short-range quantitative precipitation forecasting of a squall line observed during IHOP_2002. *Mon. Wea. Rev.*, **135**, 3381-3404.

Xue, M., M. Tong, and K. K. Droegemeier, 2006: An OSSE framework based on the ensemble square root Kalman filter for evaluating the impact of data from radar networks on thunderstorm analysis and forecasting. *J. Atmos. Oceanic Technol.*, **23**, 46-66.

Yang, S.-C., M. Corazza, A. Carrassi, E. Kalnay, and T. Miyoshi, 2009: Comparison of local ensemble transform Kalman filter, 3DVAR, and 4DVAR in a quasigeostrophic model. *Mon. Wea. Rev.*, **137**, 693-709.

Zhang, F. Q., Y. H. Weng, J. A. Sippel, Z. Y. Meng, and C. H, Bishop, 2009: Cloud-Resolving Hurricane Initialization and Prediction through Assimilation of Doppler Radar Observations with an Ensemble Kalman Filter. *Mon. Wea. Rev.*, 137, 2105-2125.

——, 2005: Dynamics and structure of mesoscale error covariance of a winter cyclone estimated through short-range ensemble forecasts. Mon. Wea. Rev., 133, 2876-2893.

Figures

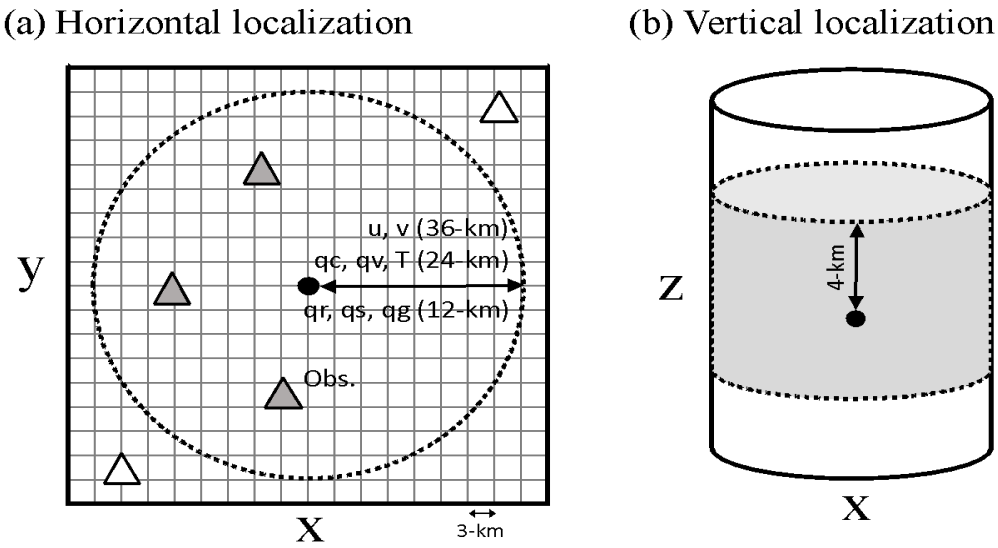

Fig. 2-1. (a) Horizontal localization: location of the model variable (black dot), locations of observation data within the localization area (gray triangles) or outside (white triangles), localization distance (double-headed arrow), localization range (dashed line); (b) Vertical localization: location of the model variable (black dot), localization distance (double-headed arrow), localization area (dashed line and gray shaded).

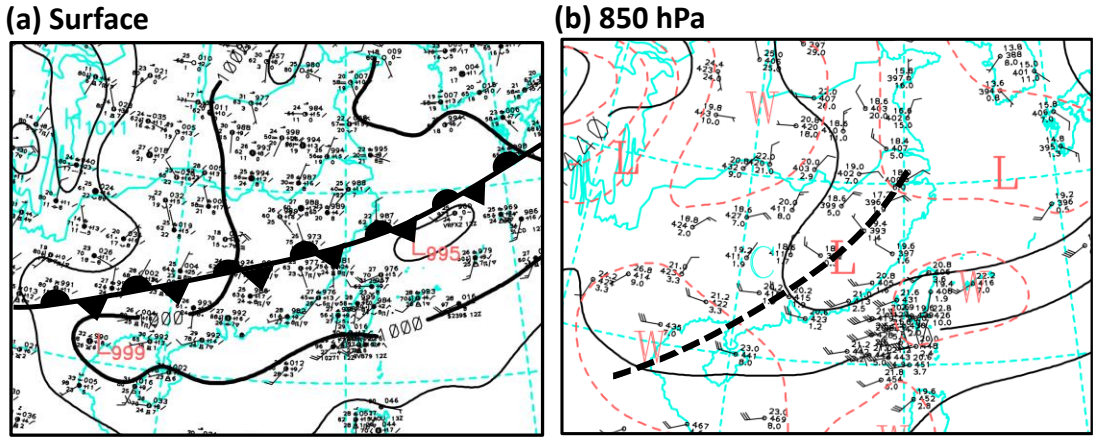

Fig. 3-1. Weather maps at 1200 UTC 11 June 2012: (a) surface; (b) 850-hPa, black dashed line is trough.

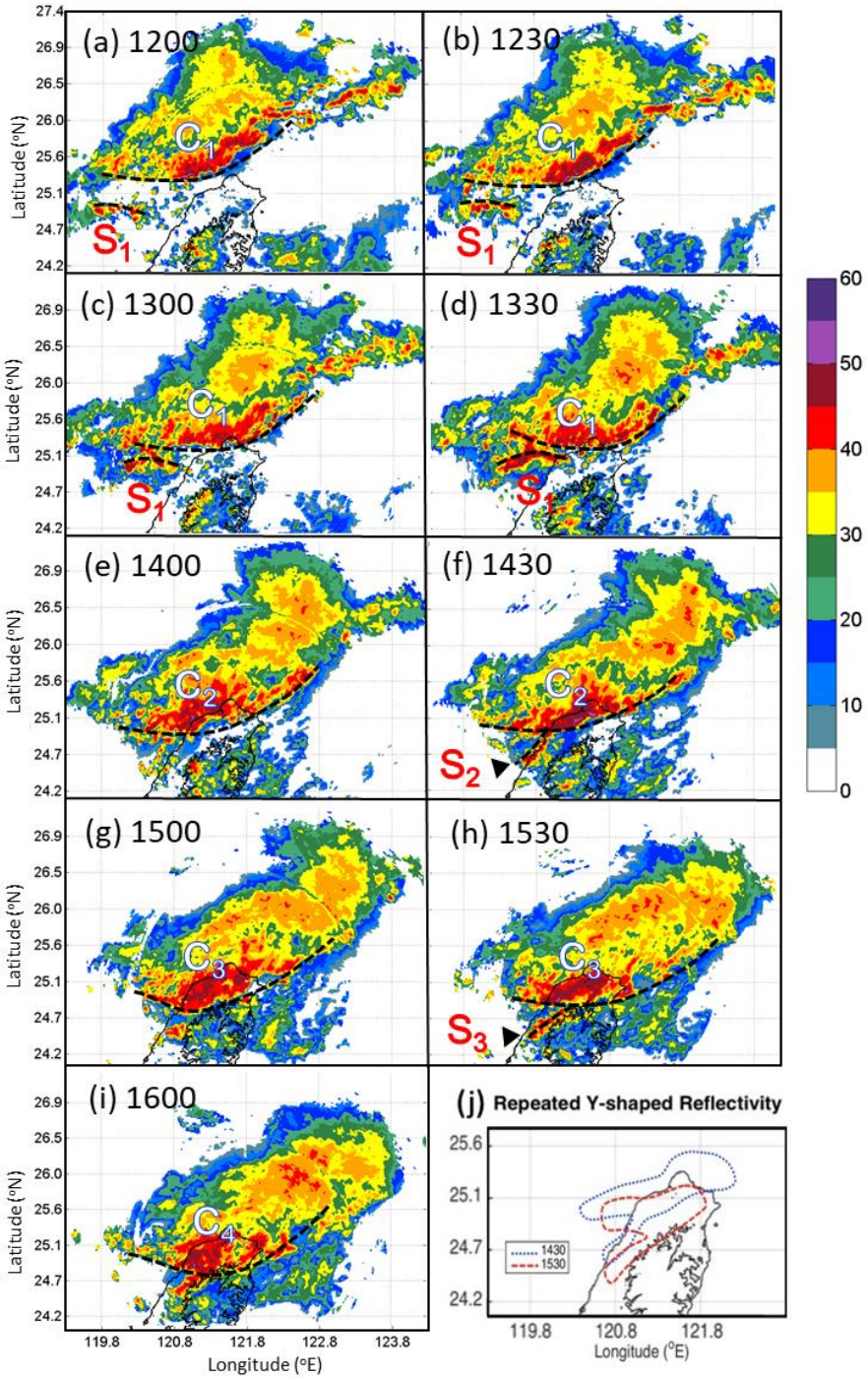

Fig. 3-2. The composite reflectivity of RCWF radar on 11 June 2012 at: (a) 1200 UTC; (b) 1230 UTC; (c) 1300 UTC; (d) 1330 UTC; (e) 1400 UTC; (f) 1430 UTC; (g) 1500 UTC; (h) 1530 UTC; (i) 1600 UTC. C1, C2, C3 and C4 indicate the main convection of the precipitation system (reflectivity > 40 dBZ) in different stages. S1, S2 and S3 are the line convection that occurred in different stages. (j) The contours of 40 dBZ shows repeated Y-shaped reflectivity at 1430 UTC and 1530 UTC.

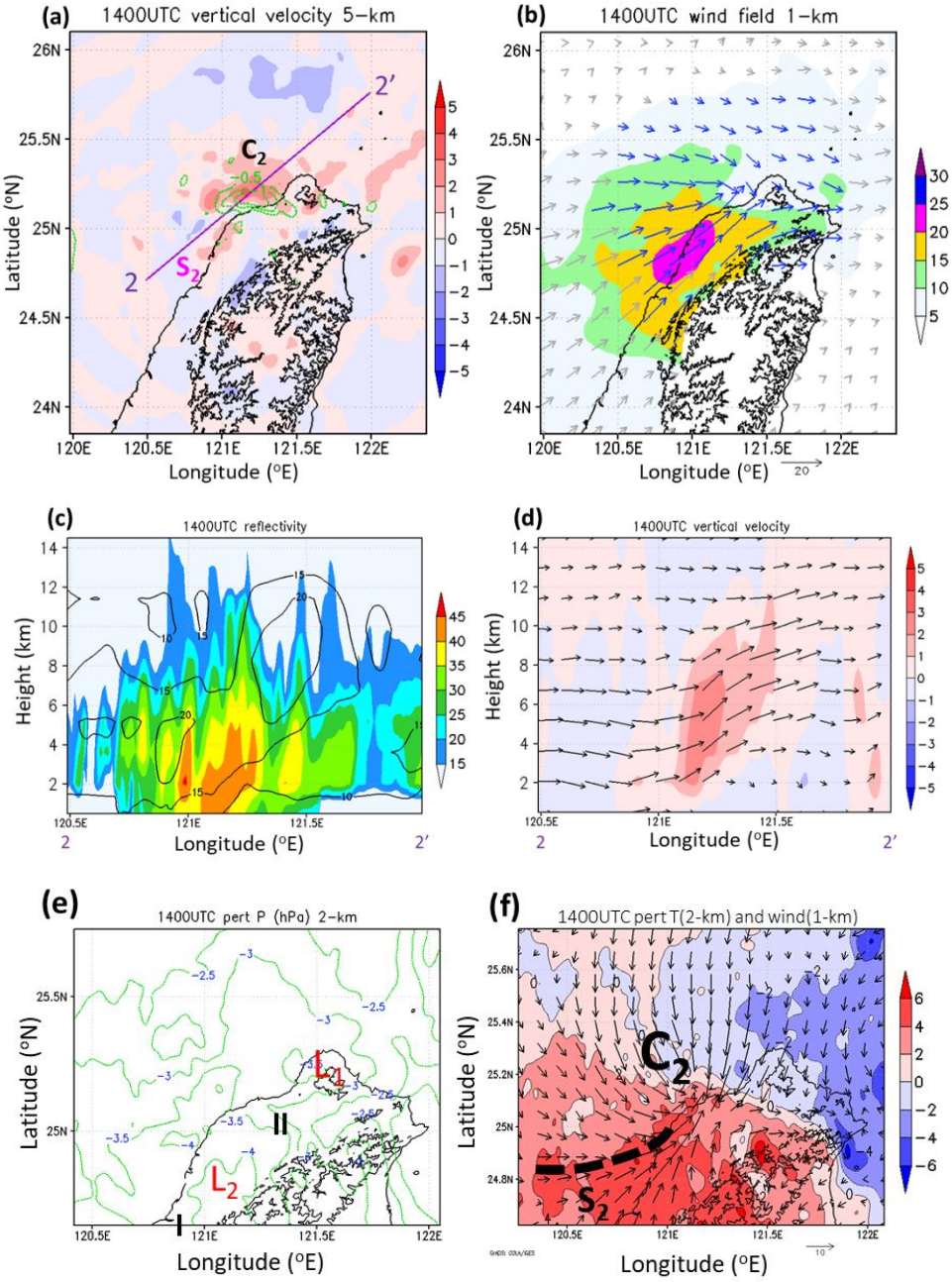

Fig. 3-3. Retrieved result at 1400 UTC 11 June 2012: (a) vertical velocity (colour shaded, unit: m s^{-1}) at 5 km and convergence area (green contour, interval is 0.5x10^{-3} s^{-1}) at 1 km; (b) horizontal wind speed (unit: m s^{-1}) and wind vector at 1 km height (blue colour shows wind retrieved with radar observations, and grey colour indicates retrieved wind beyond radar observations); (c) vertical cross-section of radar reflectivity (colour shaded, unit: dBZ) and the horizontal wind speed (contour lines); (d) cross-section of vertical wind (colour shaded, unit: m s^{-1}) and wind vector relative to the system motion. Retrieved thermodynamic perturbations (e) pressure at 2 km; (f) temperature at level 2 km (shaded), and wind direction of relative background at 1-km height (vector).

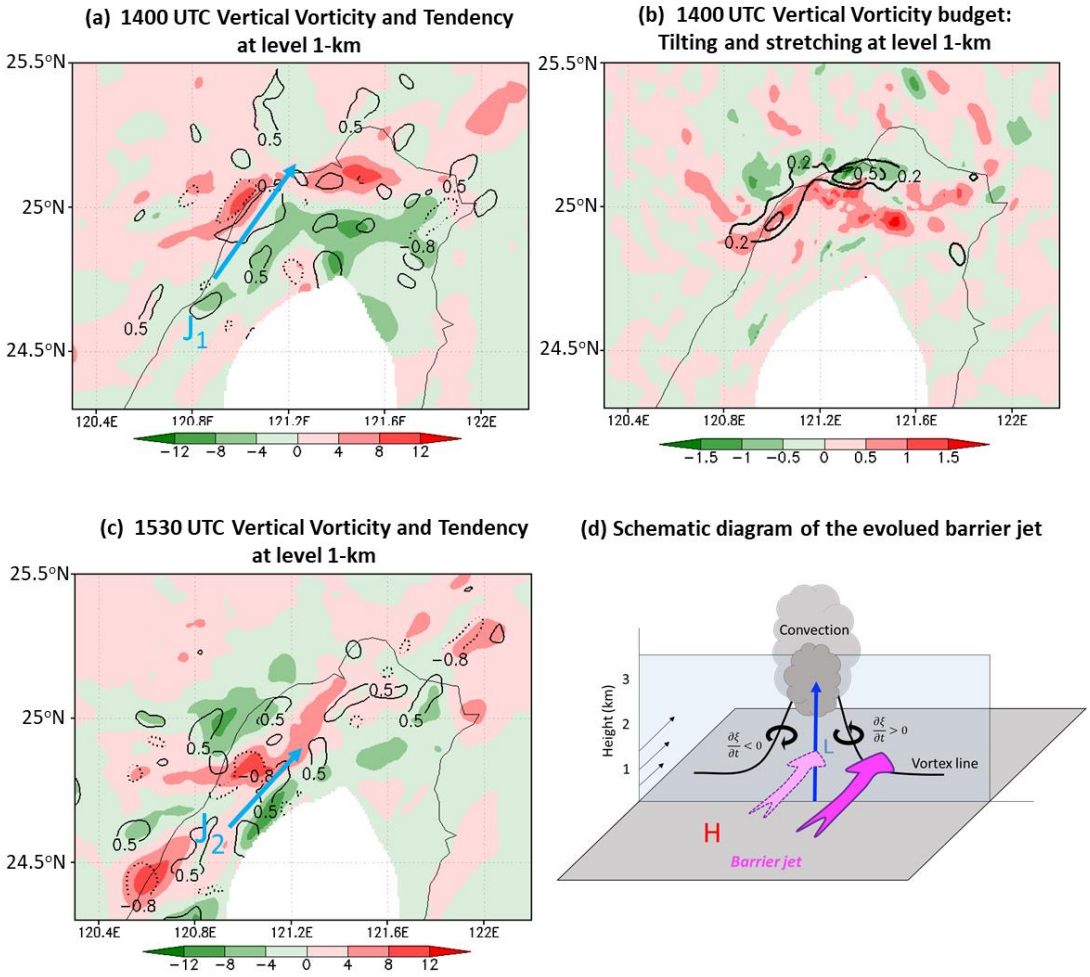

Fig. 3-4. (a) Barrier jet (J_1), the vertical vorticity fields (colour shaded, interval is $4*10^{-4}$ s^{-1}) and vertical vorticity tendency (contour lines, 0.5 and $-0.8*10^{-6}$ s^{-2}) on 1-km level from WISSDOM at 1400 UTC; (b) Vertical vorticity budget of 1-km height at 1400 UTC: tilting term (colour shaded, interval is $0.5*10^{-6}$ s^{-1}) and stretching term (contour lines, 0.2 and 0.5 $*10^{-6}$ s^{-1}); (c) same as (a), but at 1530 UTC and J_2 indicates the location of the barrier jet; (d) schematic diagram to show the migration and enhancement of the barrier jet. Thinned arrows present the strength of the wind below 3-km height, vortex line is stretched by the upward motion (blue arrow) and induced a pair of vorticity tendency, pink arrows with dashed line is the original barrier jet and solid line is the evolved barrier jet; H and L refer to the location of high and low pressure, respectively.

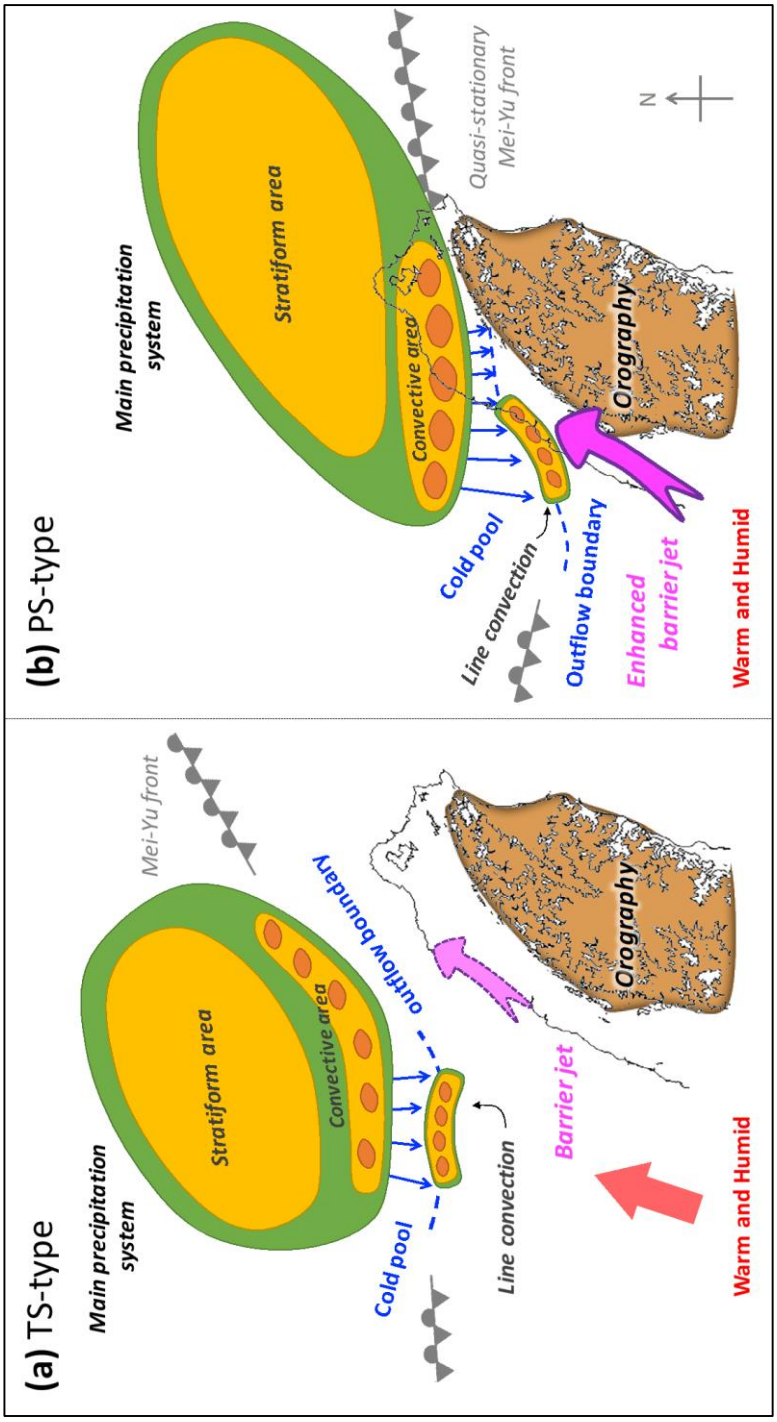

Fig. 3-5. Schematic diagrams to demonstrate the mechanism of the extremely heavy rainfall event. (a) Pre-frontal convection forms a TS-type precipitation over the ocean, and the line convection is triggered due the cold outflow encountering a warm and humid southwesterly flow; (b) the strengthened cold pool and enhanced barrier jet repeatedly triggered the Y-shaped echo line convection, then merge with the main convection to form a PS-type precipitation over northern Taiwan. The location of the Mei-Yu front and the warm/humid southwesterly flow (red arrow) illustrate the environmental condition of the synoptic scale over Taiwan. The location of the cold pool and the orography in northern Taiwan blocks the displacement of the main convection.

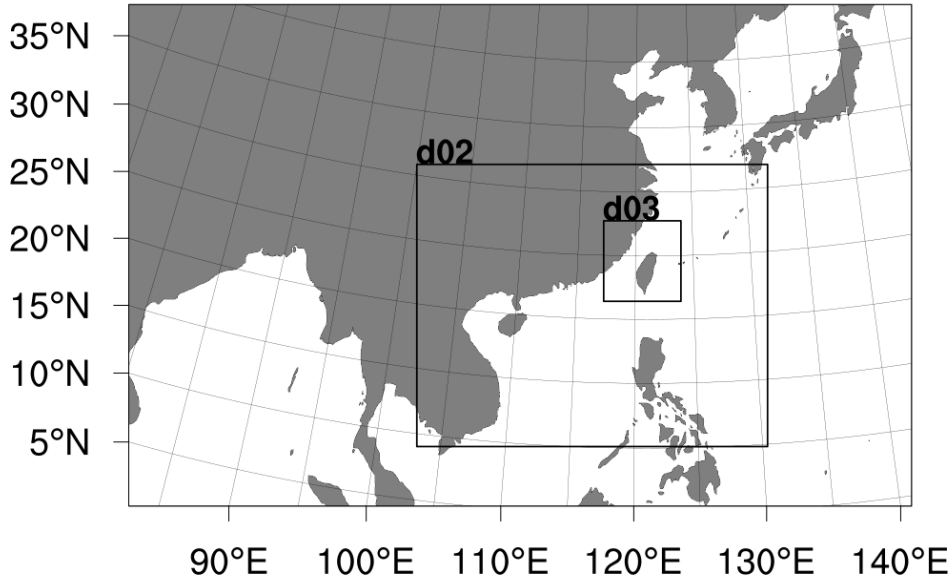

Fig. 4-1. Domain nesting of the WRF model with horizontal grid spacing of 27 (251 × 261 points), 9 (337 × 271 points), and 3 (223 × 232 points) km, respectively.

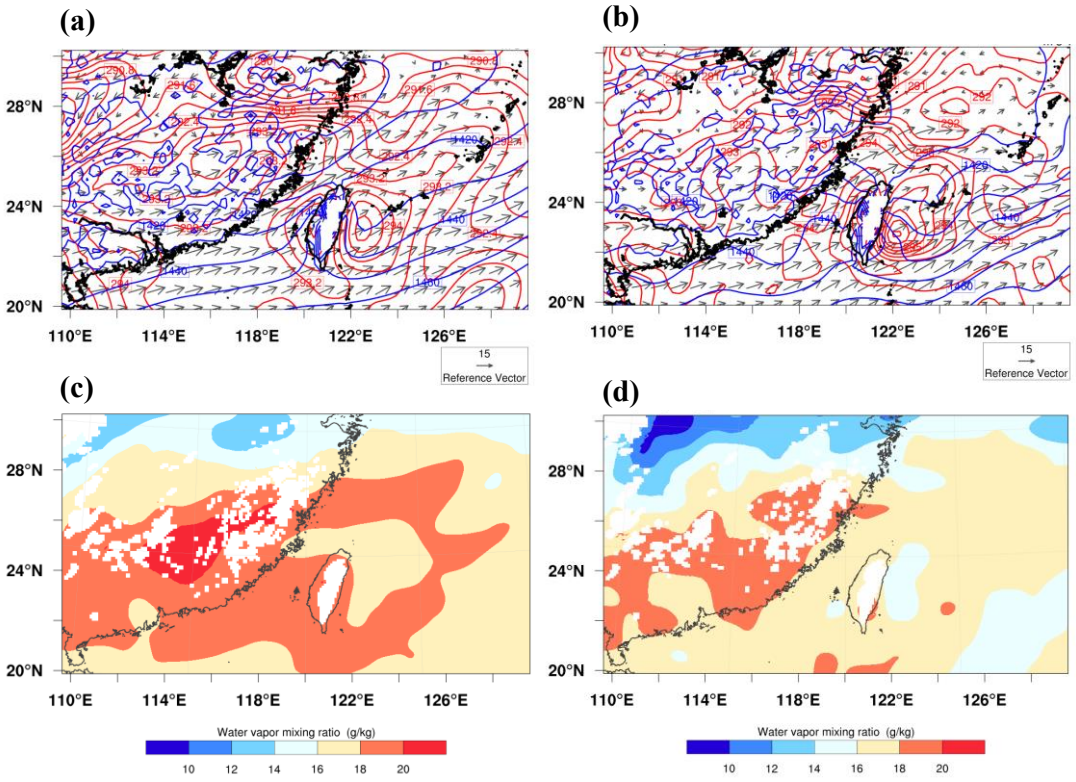

Fig. 4-2. Reanalysis fields of (a), (b) potential height (blue line), potential temperature (red line), and wind vector (gray vector) at 850-hPa; (c), (d) water vapor mixing ratio at 925-hPa at 0000 UTC 11 June 2012. (a), (c) ERA-interim for the truth run; (b), (d) NCEP for the NoDA and OSSE experiments.

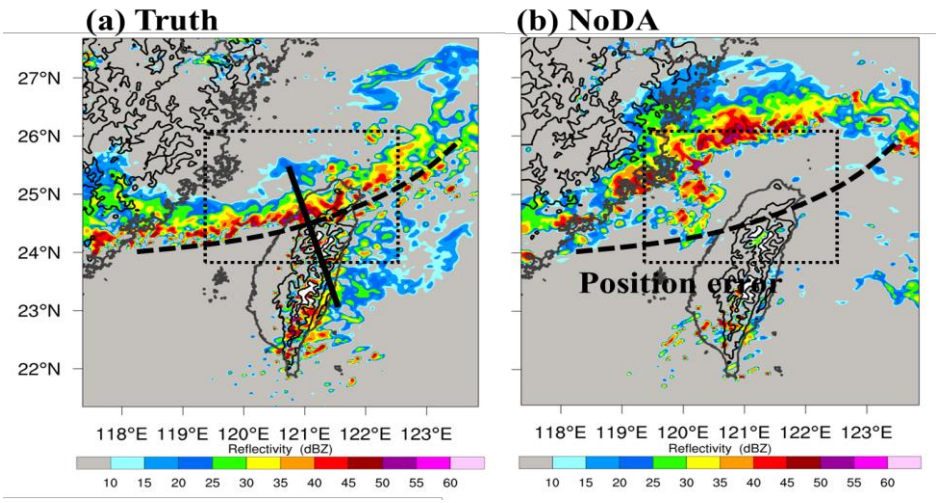

Fig. 4-3. Reflectivity at 2.5-km height (shaded) in d03 shows the rainband (black-dashed line) located at northern Taiwan at 1400 UTC in (a) "truth" simulated from the initial condition ERA-interim 0.75º × 0.75º and (b) NoDA simulated from the initial condition NCEP-FNL 1º × 1º. The black solid line in 5a is a vertical cross-section portion between (120.75ºE, 25.93ºN) and (121.18ºE, 24.64ºN). The dotted square shows the focused area in the study.

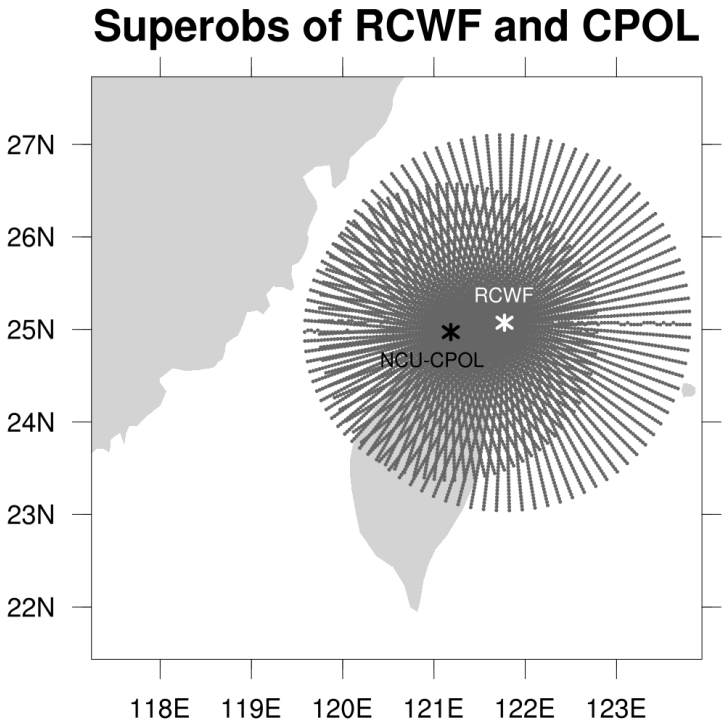

Fig. 4-4. The super observation points (gray) of simulated observations averaging 5-km in the radial direction and 5º in the azimuthal direction on every sweep from RCWF (121.77ºE, 25.07ºN) and NCU-CPOL (121.18ºE, 24.97ºN). The gray marks (*) are the radar locations of RCWF (white) and NCU-CPOL (black).

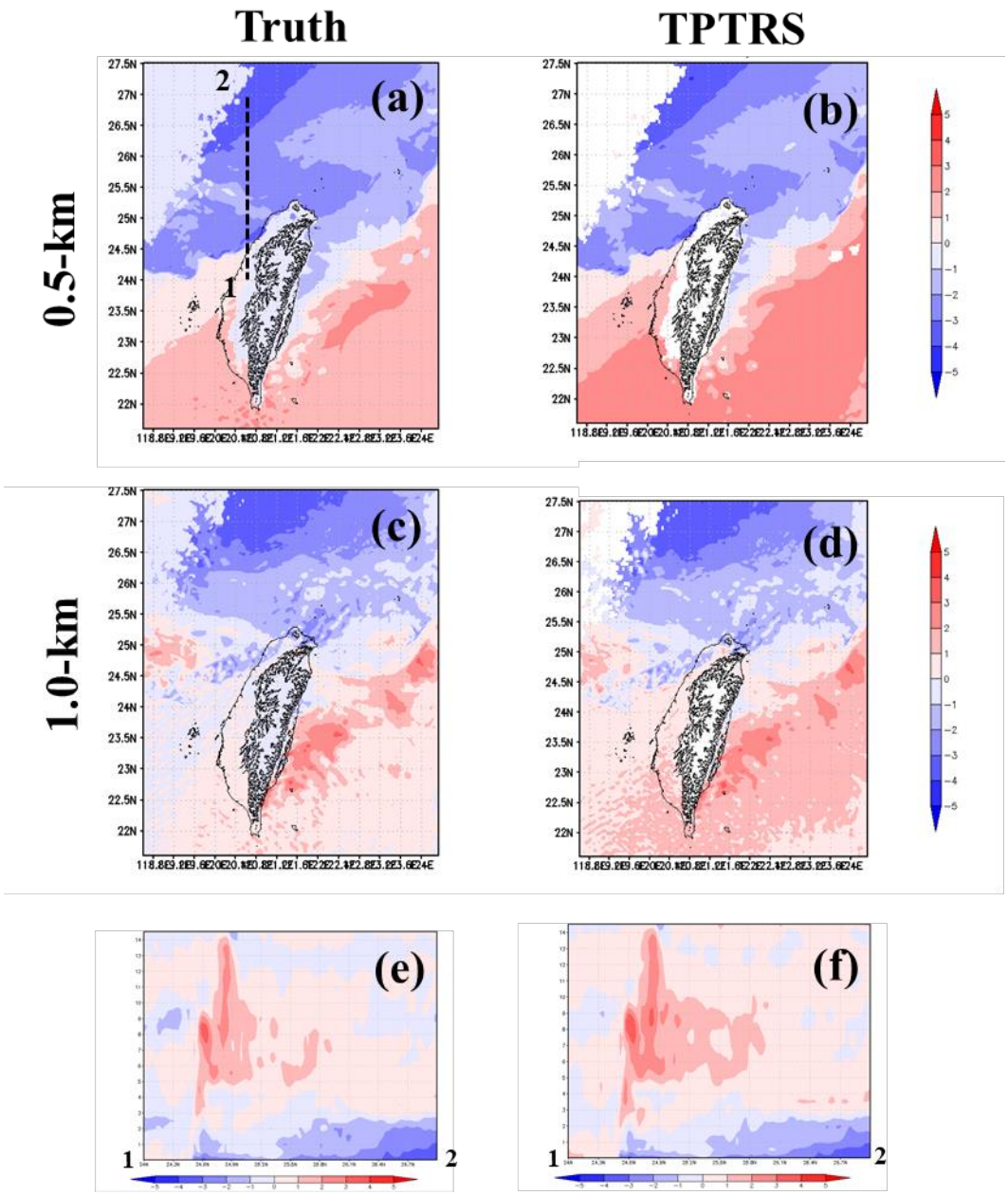

Fig. 4-5. Temperature perturbation (a), (b) at 0.5-km height; (c), (d) at 1.5-km height; (e), (f) Vertical cross-section of temperature perturbation along dashed line in (a) at 1400 UTC. (a), (c), (e) are truth; (b), (d), (f) are Retrieved by TPTRS at 1400 UTC.

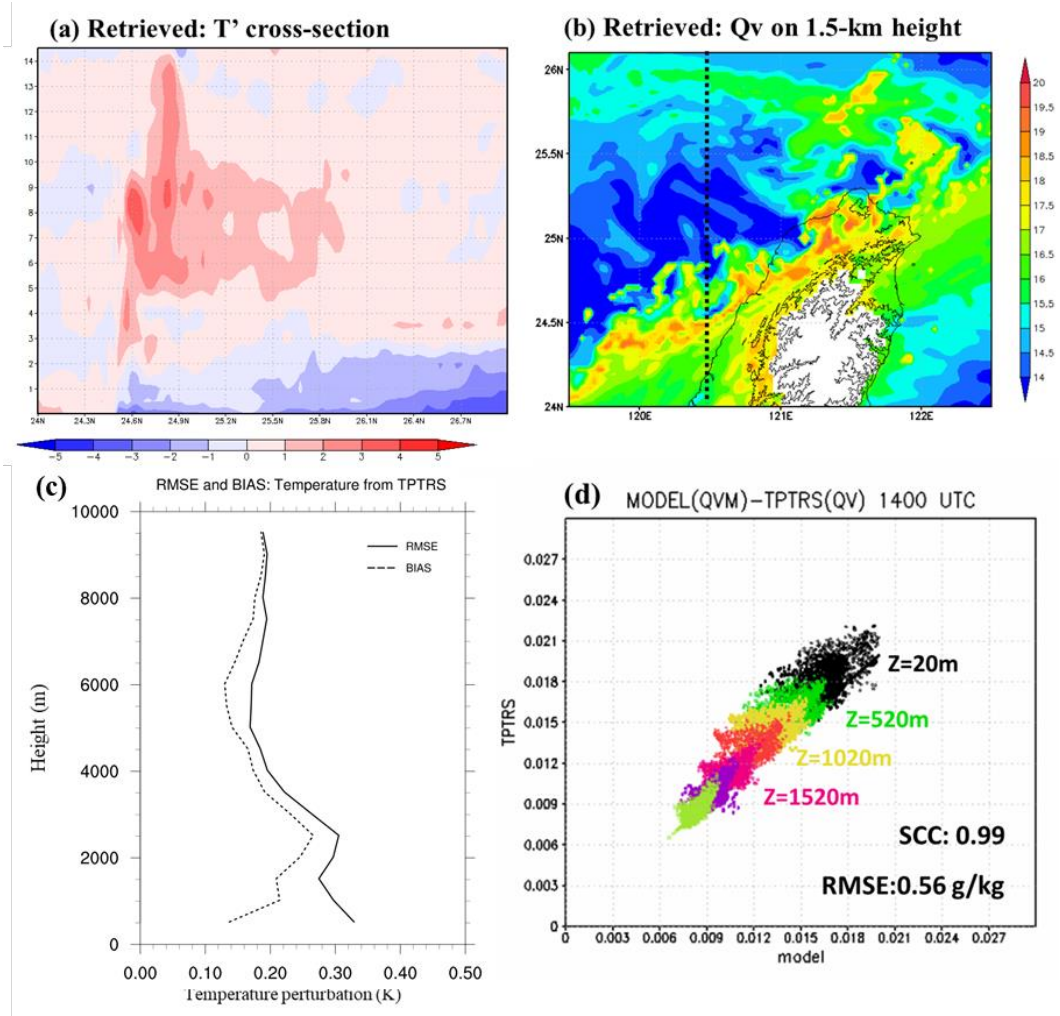

Fig. 4-6. (a) Vertical cross-section of retrieved temperature perturbation along dashed line in (b) at 1400 UTC. (b) Retrieved water vapor at 1.5-km height at 1400 UTC. (c) Vertical profile of retrieval temperature RMSE and BIAS. (d) Scatter plot of water vapor between truth model and retrieved by TPTRS.

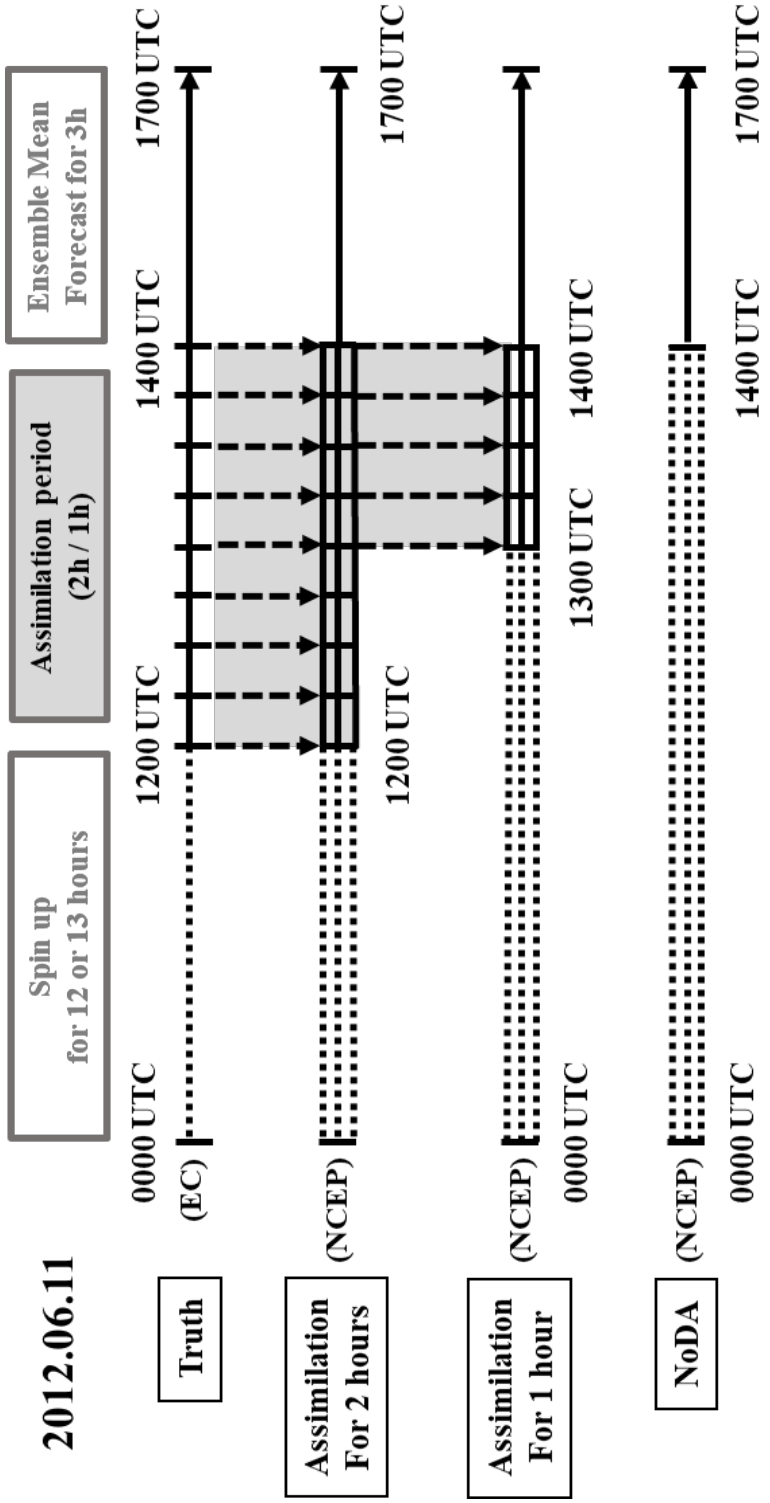

Fig. 4-7. The schematic design of the study strategy. The single lines (solid and dotted) refer to a single run, while the triple lines represent ensemble simulations. The dotted lines indicate the model spin-up period from 0000 UTC 11 June 2012 to 1200 (or 1300) UTC. The gray area indicates the data assimilation period for two (or one) hours experiment and the dashed vectors show the frequency of assimilating data every 15-min.

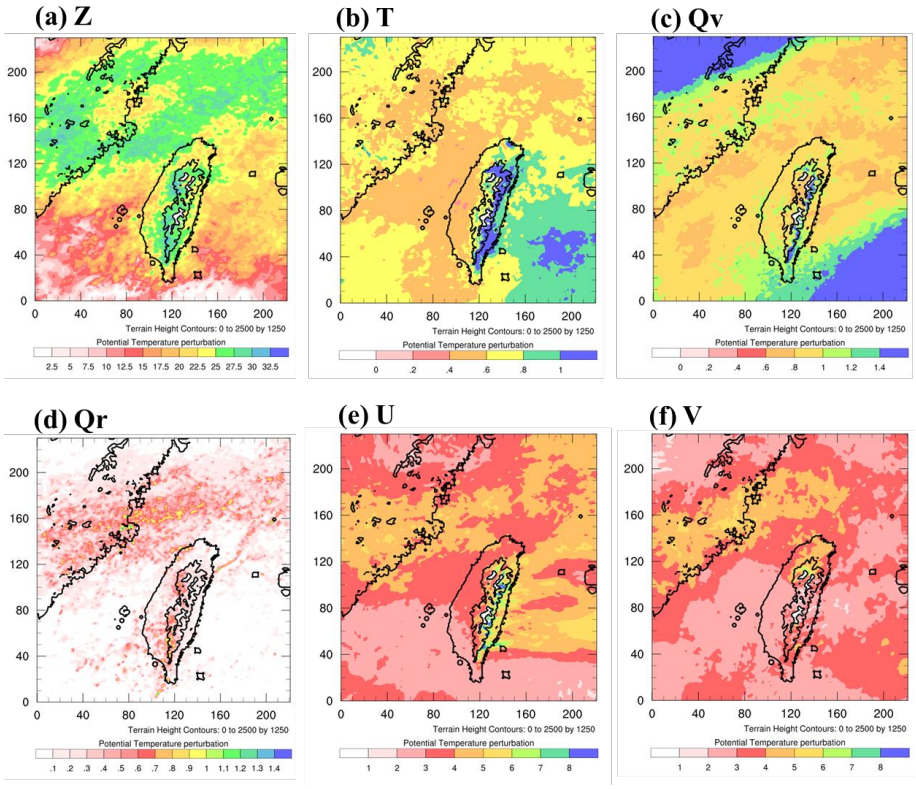

Fig. 5-1. The ensemble spread on 2500 m height at 1300 UTC. (a) Z; (b) T; (c) Qv; (d) Qr; (e) U; (f) V.

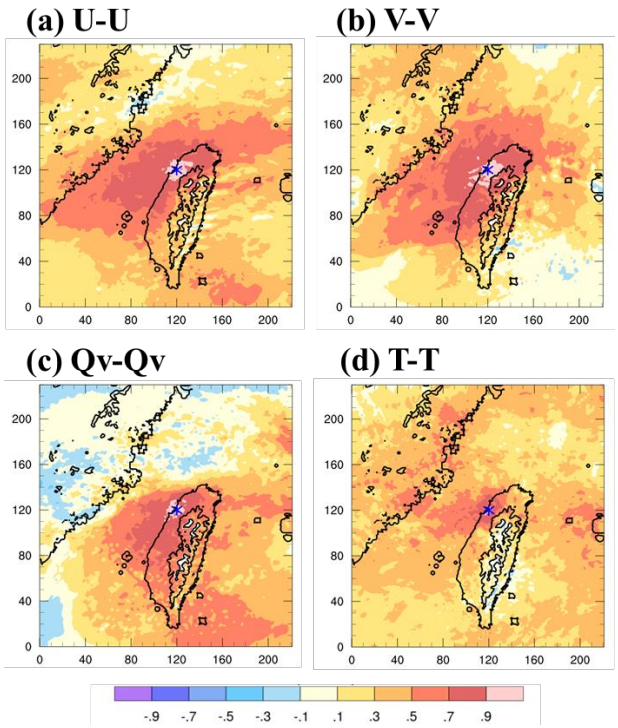

Fig. 5-2. Auto-correlation on 2500 m. Blue mark (*) means the location of reference variable that shows on the first variable of title. (a) U; (b) V; (c) Qv; (d) T.

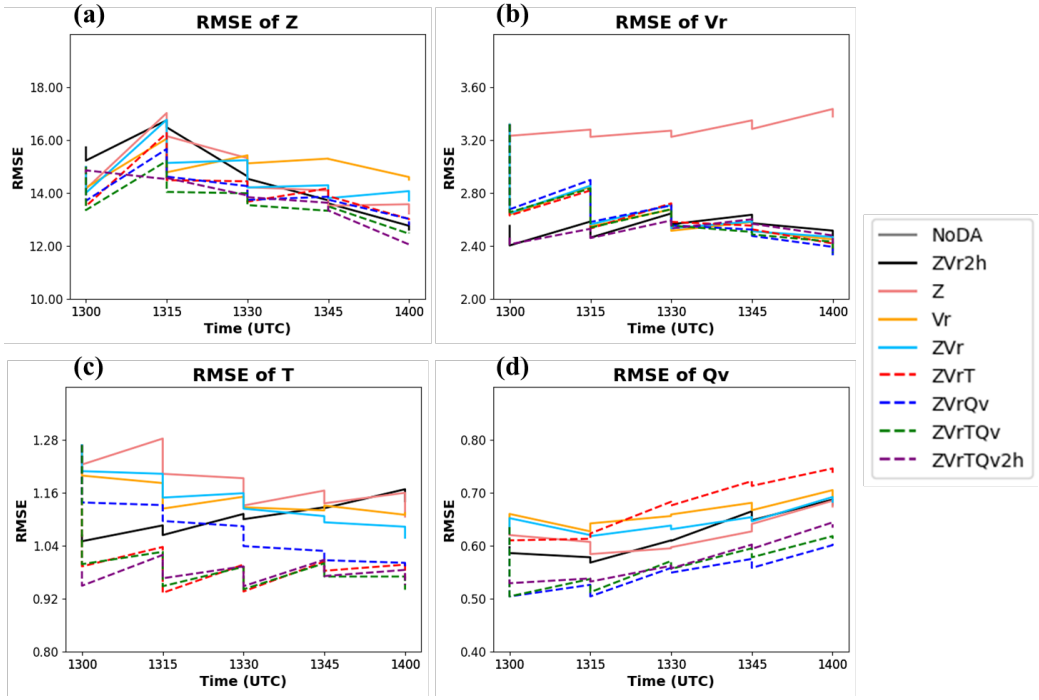

Fig. 5-3. Root mean square error in assimilation period (a) Z (unit: dBZ); (b) Vr (unit: m s^{-1}); (c) T (unit: K); (d) Qv (unit: g kg^{-1}).

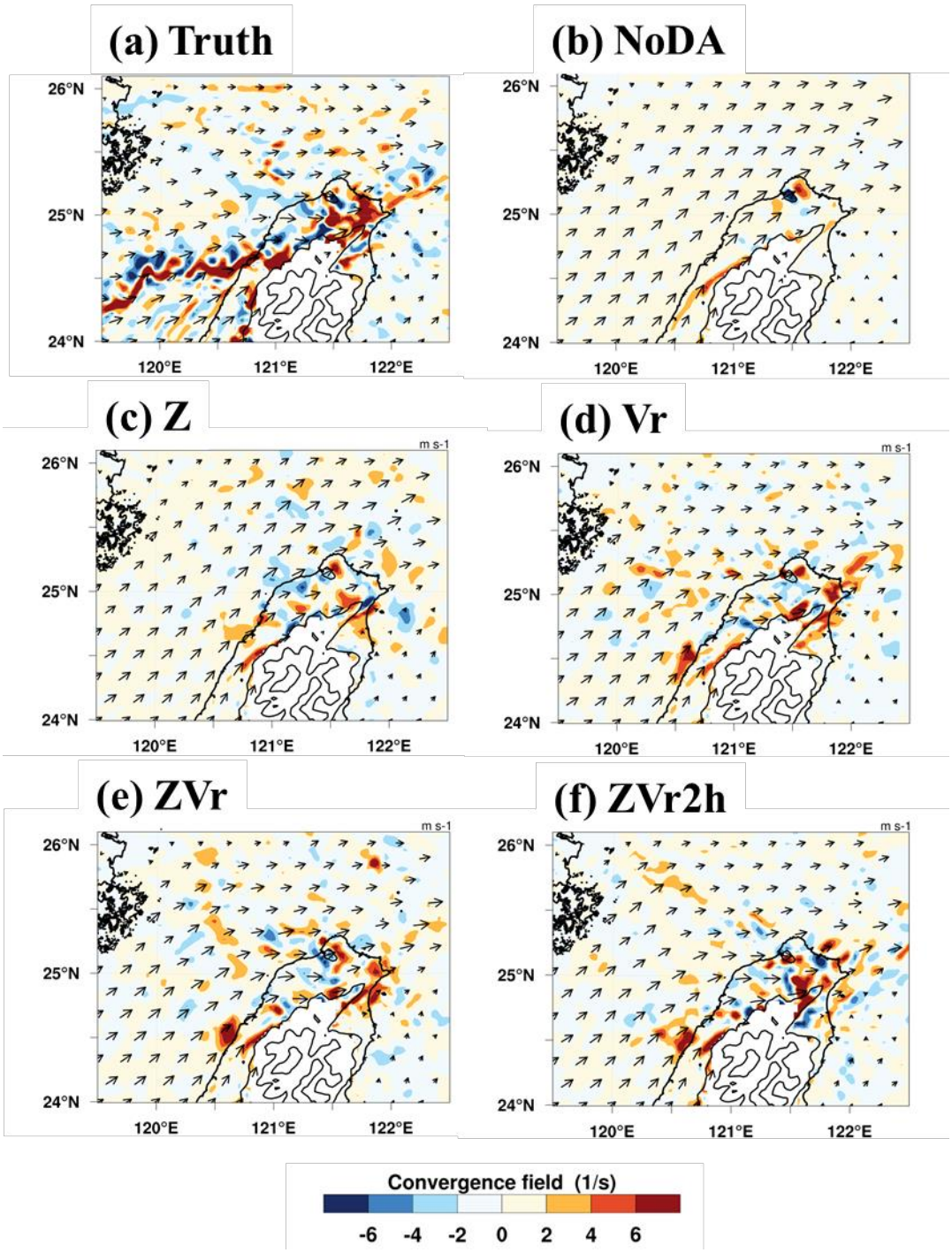
(a) Truth
(b) NoDA
(c) Z
(d) Vr
(e) ZVr
(f) ZVr2h
26°N
25°N
24°N
120°E
121°E
122°E
m s-1
Convergence field (1/s)
-6 -4 -2 0 2 4 6

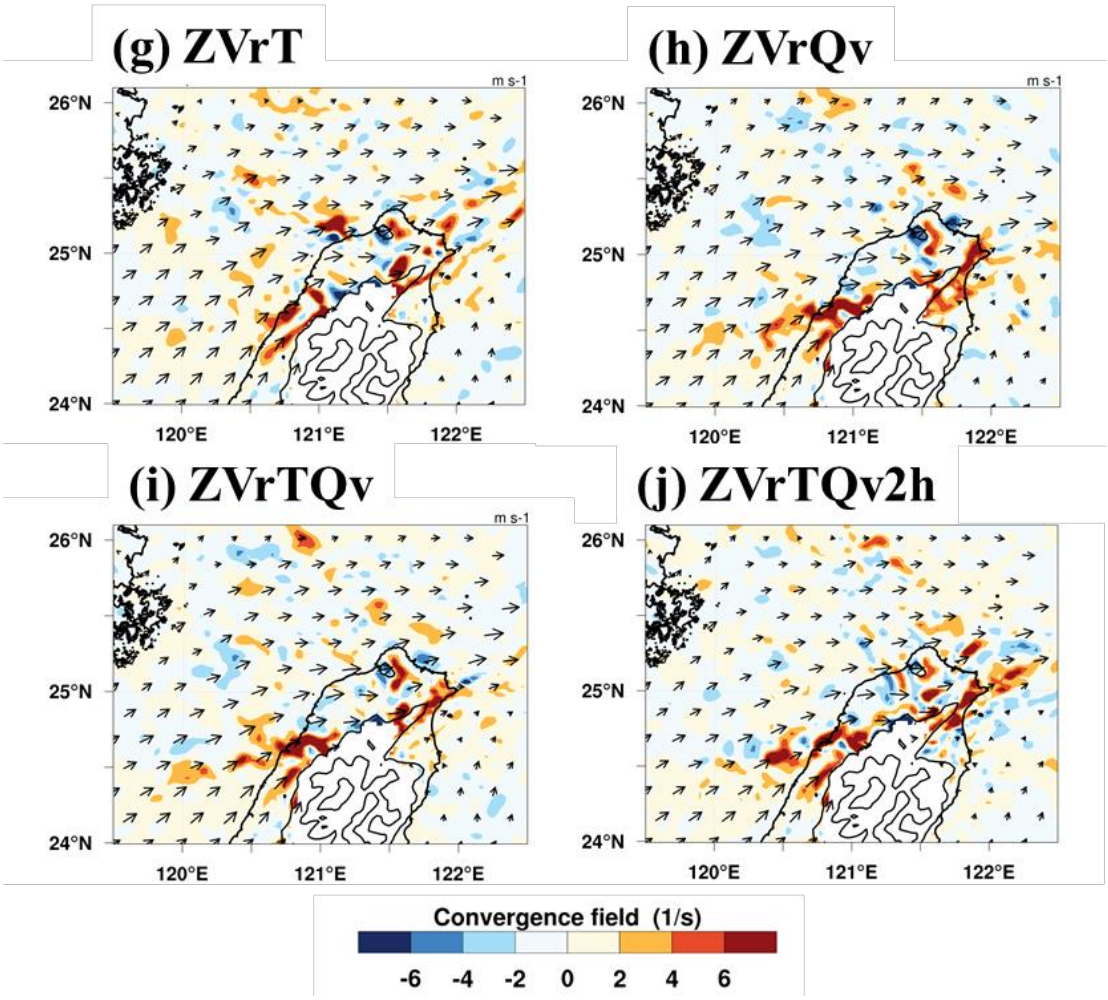

Fig. 5-4. The low-level convergence field (shaded, units: 10^{-4} s^{-1}) and wind vectors are shown at a 1-km height of 1400 UTC and focus on a small area of northern Taiwan from d03: (a) Truth; (b) NoDA; (c) Z; (d) Vr; (e) ZVr; (f) ZVr2h; (g) ZVrT; (h) ZVrQv; (i) ZVrTQv; (j) ZVrTQv2h.

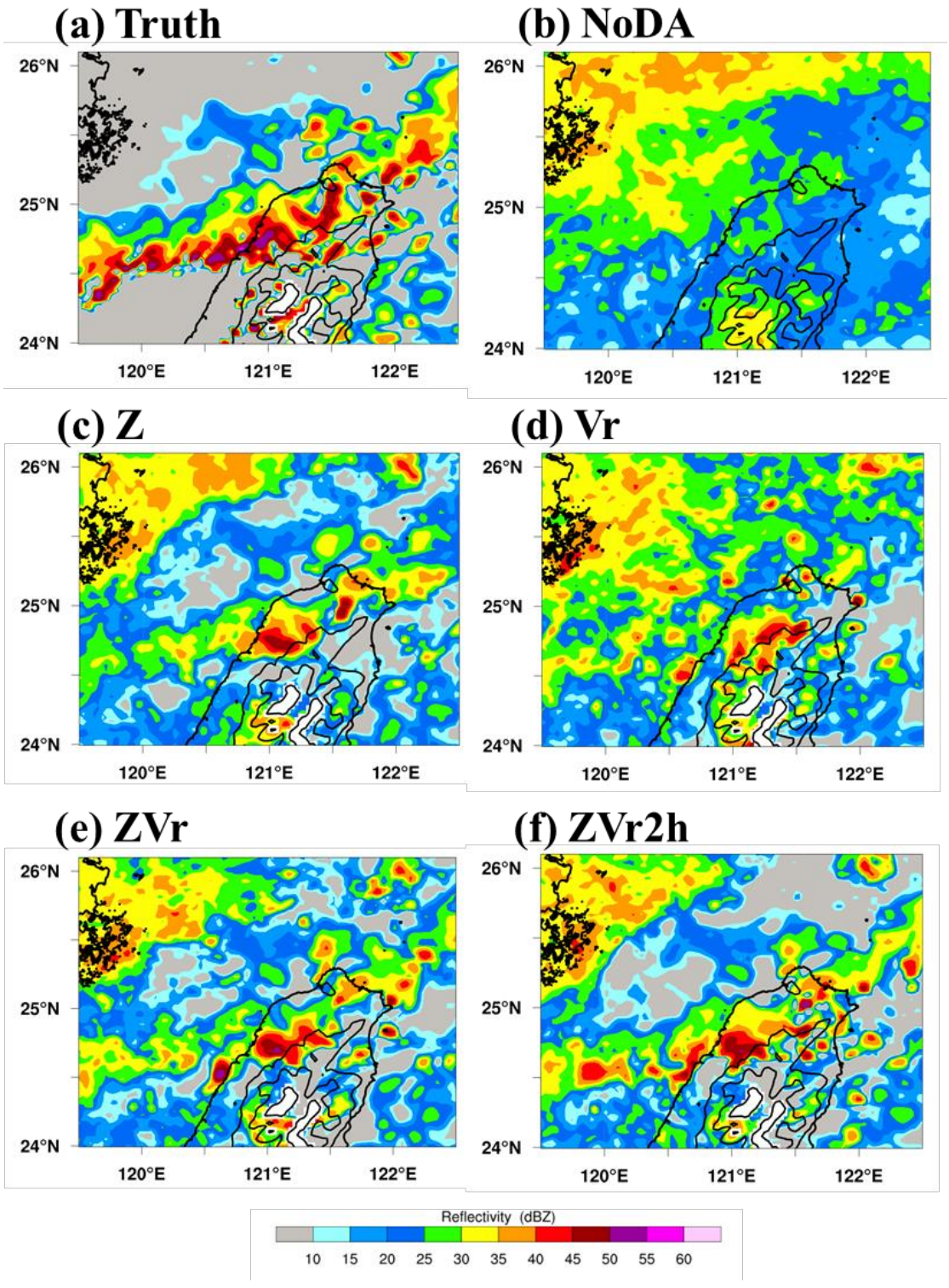
(a) Truth
(b) NoDA
(c) Z
(d) Vr
(e) ZVr
(f) ZVr2h
26°N
25°N
24°N
120°E
121°E
122°E
Reflectivity (dBZ)
10 15 20 25 30 35 40 45 50 55 60

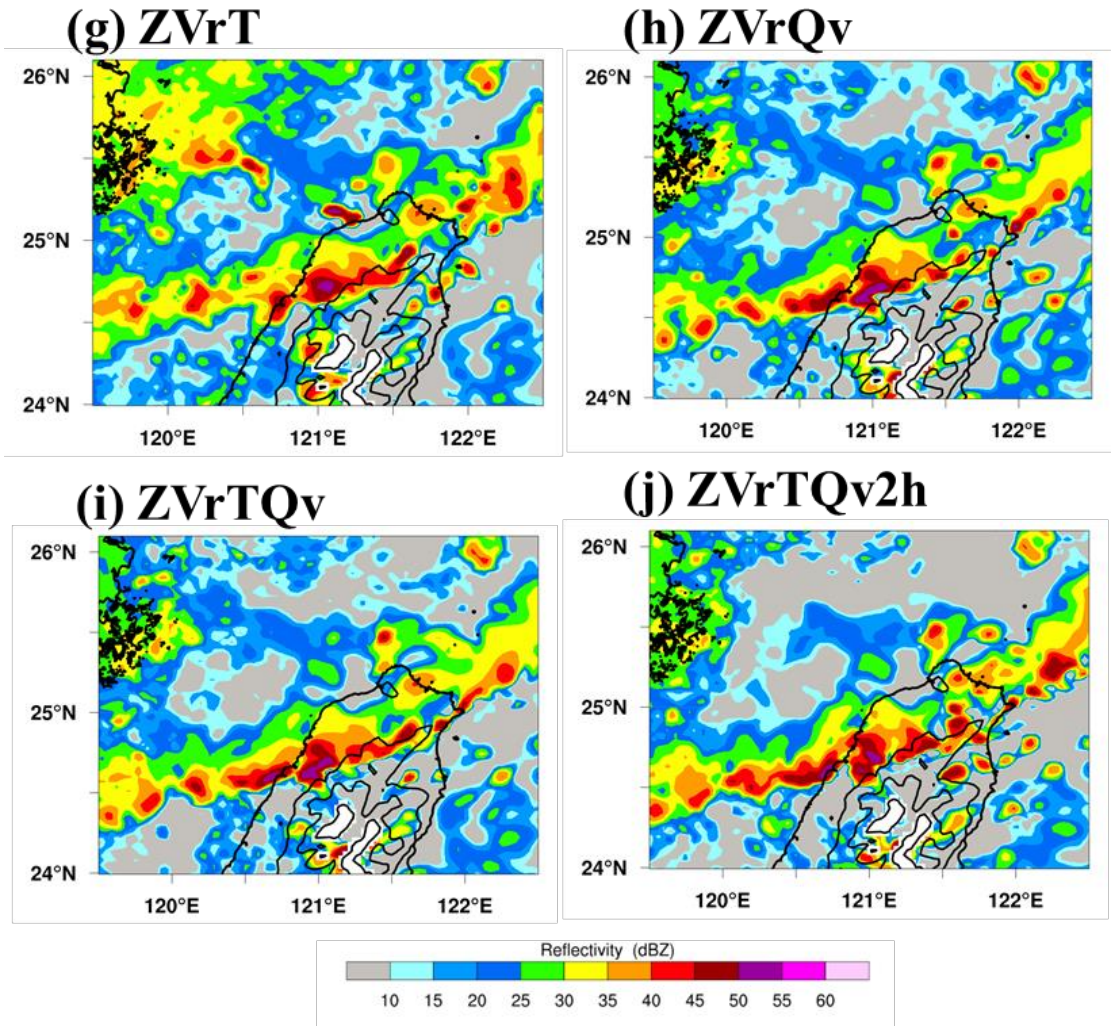

Fig. 5-5. Reflectivity field on 2.5-km height at 1400 UTC. (a) Truth; (b) NoDA; (c) Z; (d) Vr; (e) ZVr; (f) ZVr2h; (g) ZVrT; (h) ZVrQv; (i) ZVrTQv; (j) ZVrTQv2h.

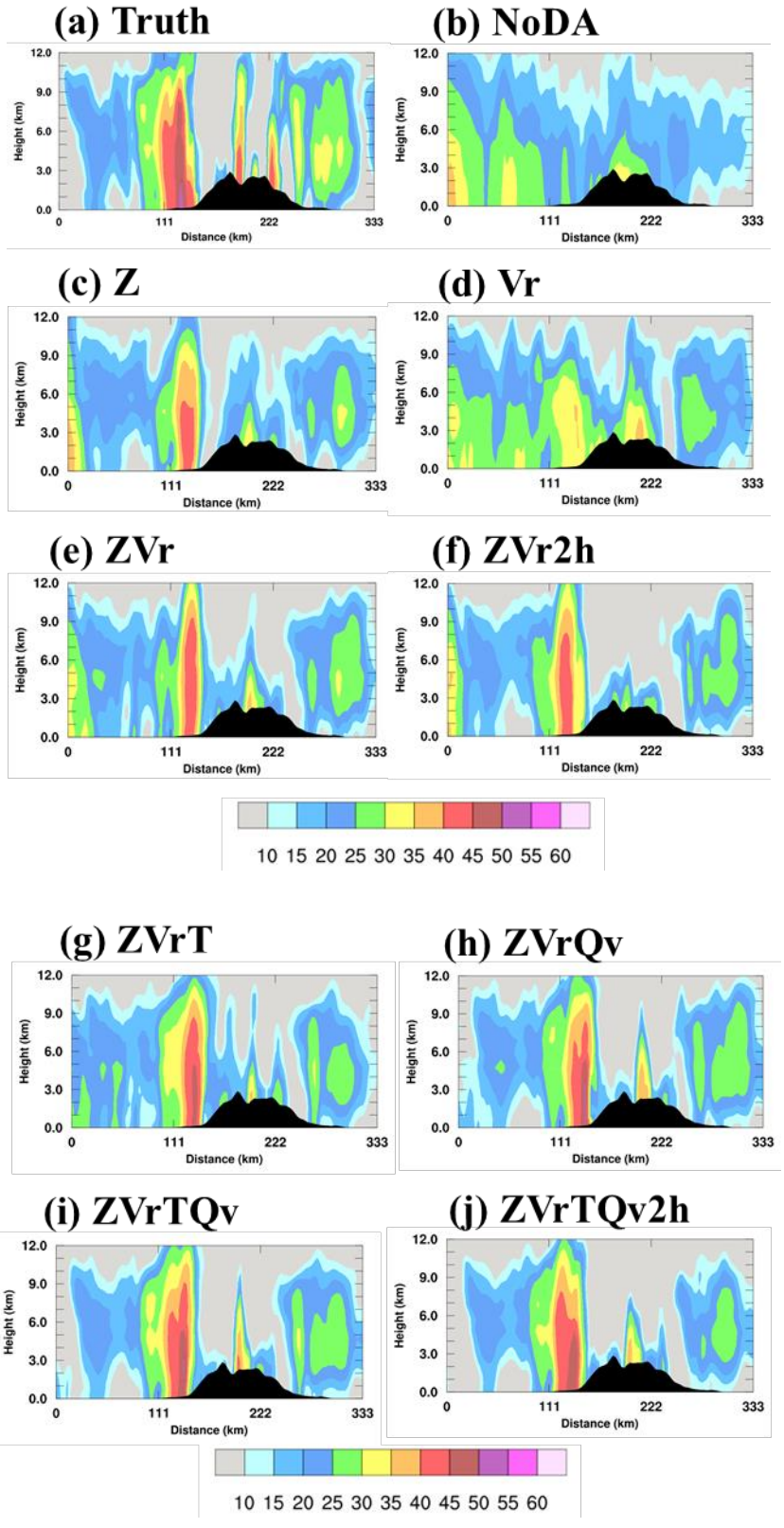

Fig. 5-6. Vertical cross-section of reflectivity (shaded colors) at 1400 UTC as the black solid line in Fig. 5a: (a) Truth; (b) NoDA; (c) Z; (d) Vr; (e) ZVr; (f) ZVr2h; (g) ZVrT; (h) ZVrQv; (i) ZVrTQv; (j) ZVrTQv2h.

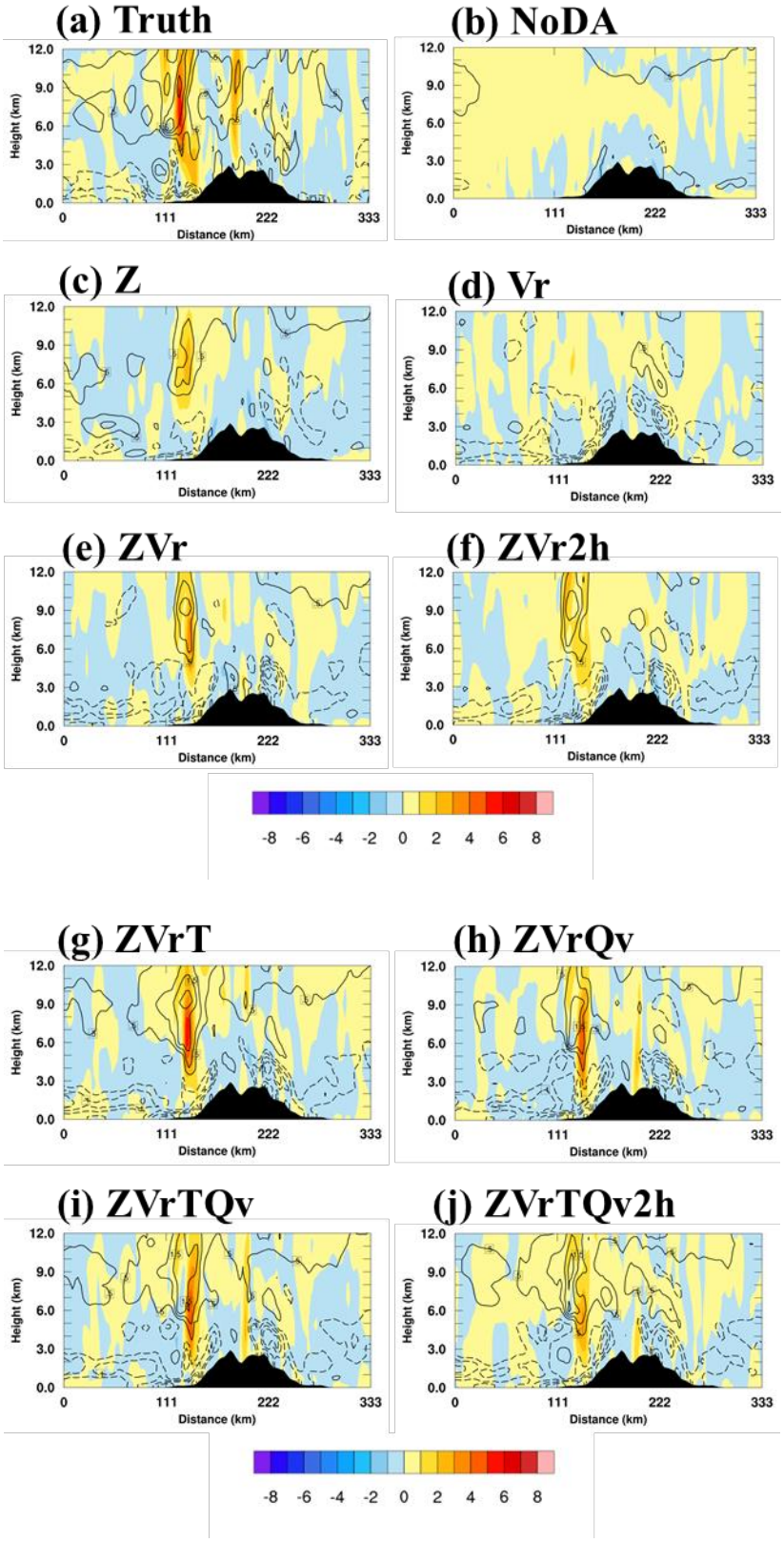

Fig. 5-7. Vertical velocity (shaded) and Potential temperature perturbation (contours, solid lines are positive values while dashed line are negative values with contours of -1.5, -1.2, -0.5, 1.0, 3.0, 5.0 K) at 1400 UTC shown on vertical cross-sections as in Fig. 5a: (a) Truth; (b) NoDA; (c) Z; (d) Vr; (e) ZVr; (f) ZVr2h; (g) ZVrT; (h) ZVrQv; (i) ZVrTQv; (j) ZVrTQv2h.

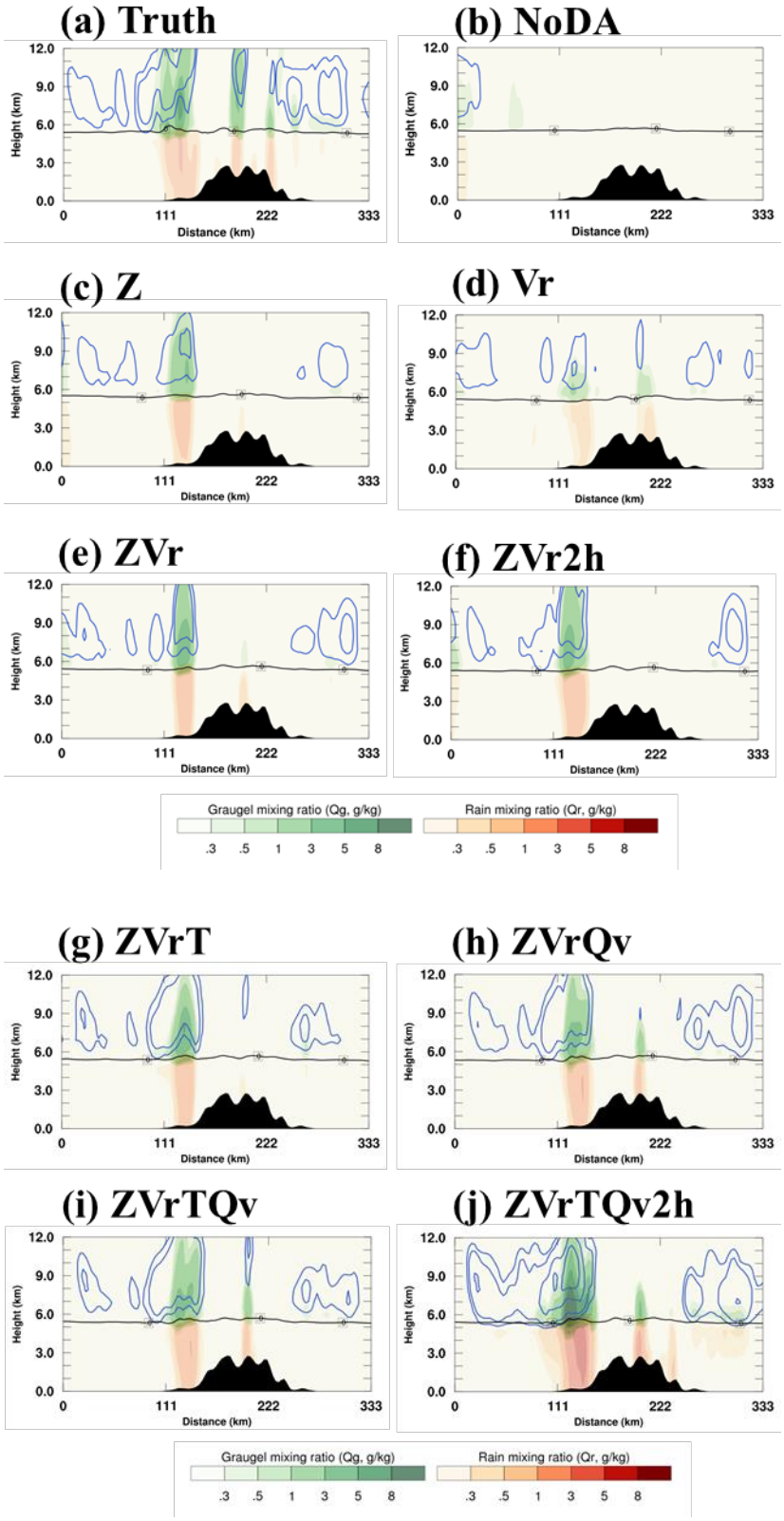

Fig. 5-8. The mixing ratios of graupel(Qg), snow(Qs), and rain(Qr): (a) Truth; (b) NoDA; (c) Z; (d) Vr; (e) ZVr; (f) ZVr2h; (g) ZVrT; (h) ZVrQv; (i) ZVrTQv; (j) ZVrTQv2h.

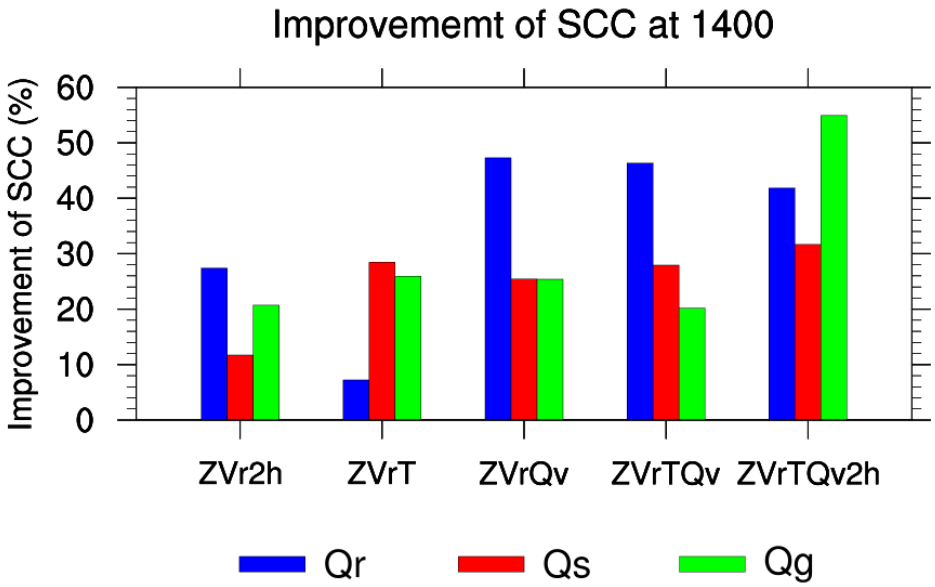

Fig. 5-9. Improvement of final ayalysis at 1400 UTC in spatial correlation coefficient of hydrometer variables compared with Exp. ZVr. Qg, Qs, and Qg refer to the mixing ratios of graupel, snow, and rain.

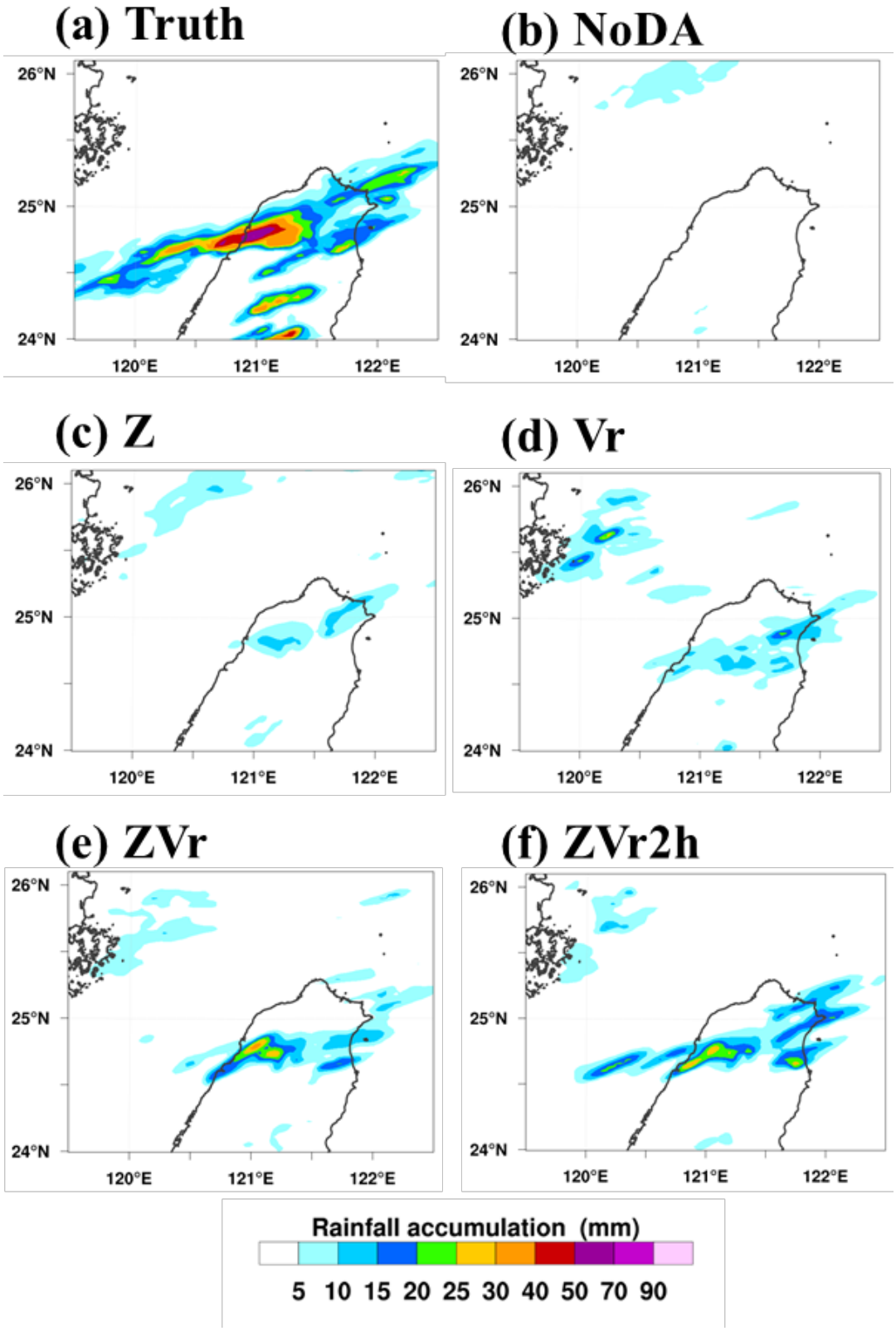
(a) Truth
(b) NoDA
(c) Z
(d) Vr
(e) ZVr
(f) ZVr2h
26°N
25°N
24°N
120°E
121°E
122°E
Rainfall accumulation (mm)
5 10 15 20 25 30 40 50 70 90

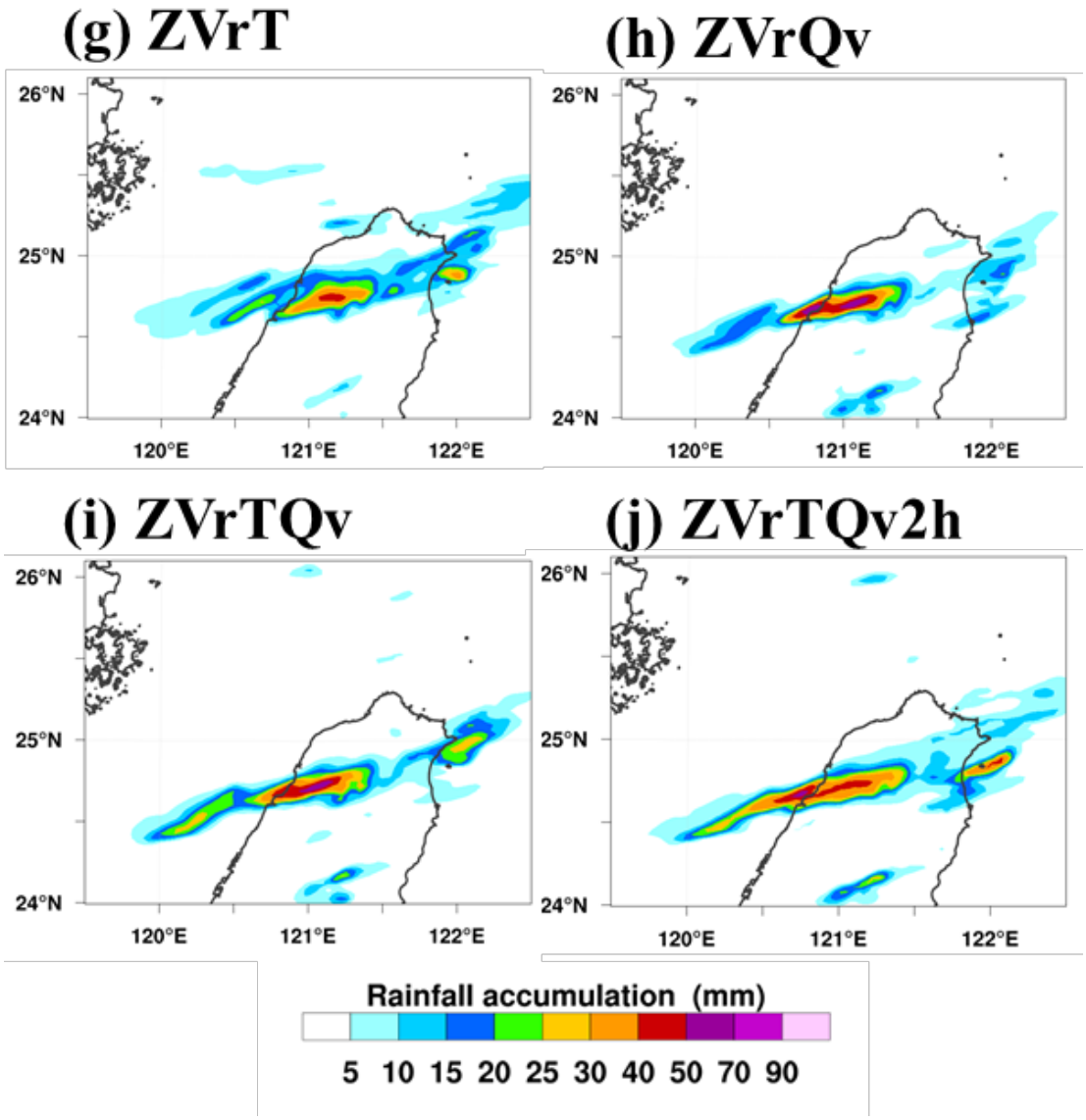

Fig. 5-10. Rainfall accumulation at northern Taiwan in d03 from 1400 UTC to 1500 UTC. (a) Truth; (b) NoDA; (c) Z; (d) Vr; (e) ZVr; (f) ZVr2h; (g) ZVrT; (h) ZVrQv; (i) ZVrTQv; (j) ZVrTQv2h.

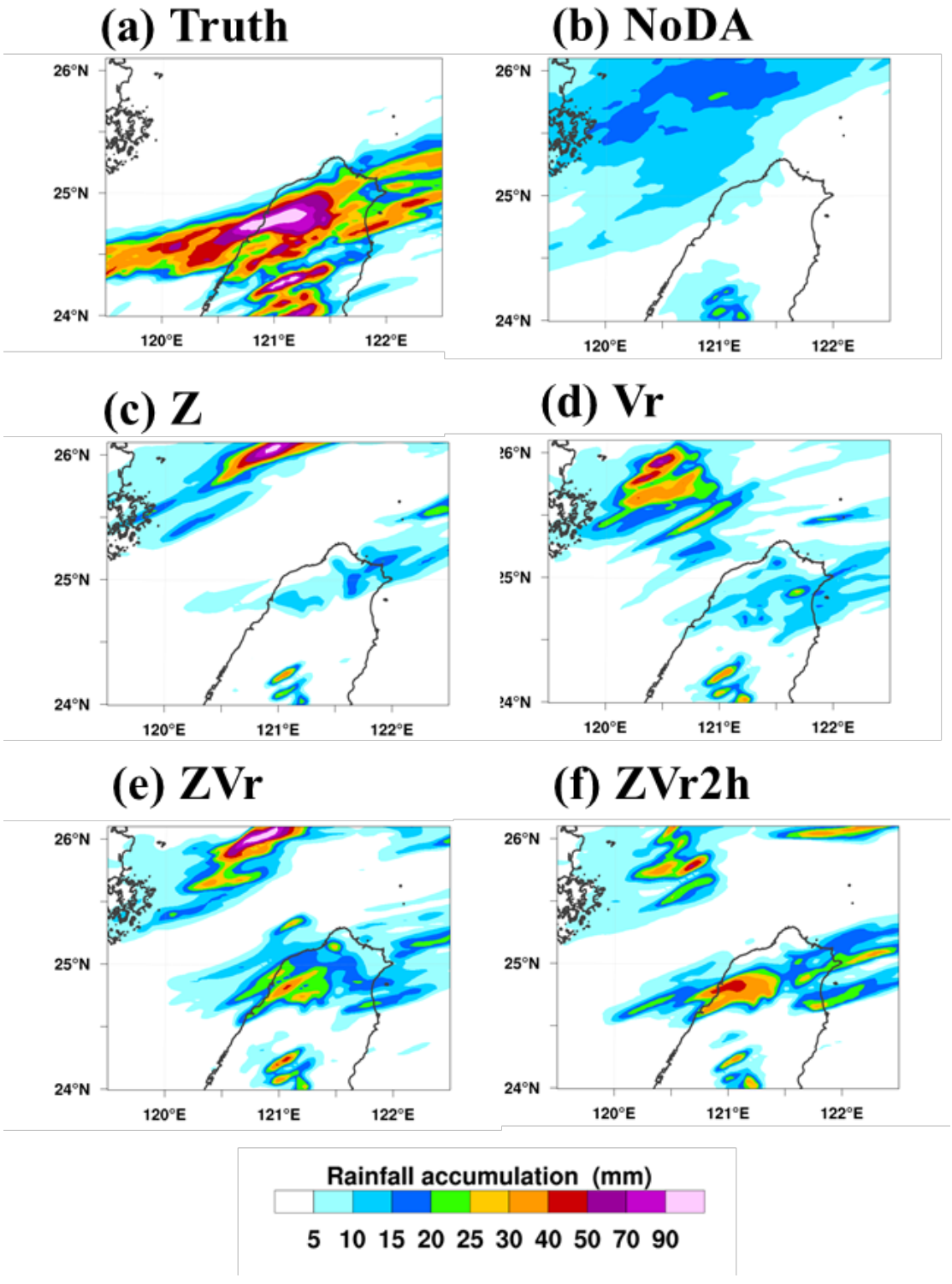
(a) Truth
(b) NoDA
(c) Z
(d) Vr
(e) ZVr
(f) ZVr2h
26°N
25°N
24°N
120°E
121°E
122°E
Rainfall accumulation (mm)
5 10 15 20 25 30 40 50 70 90

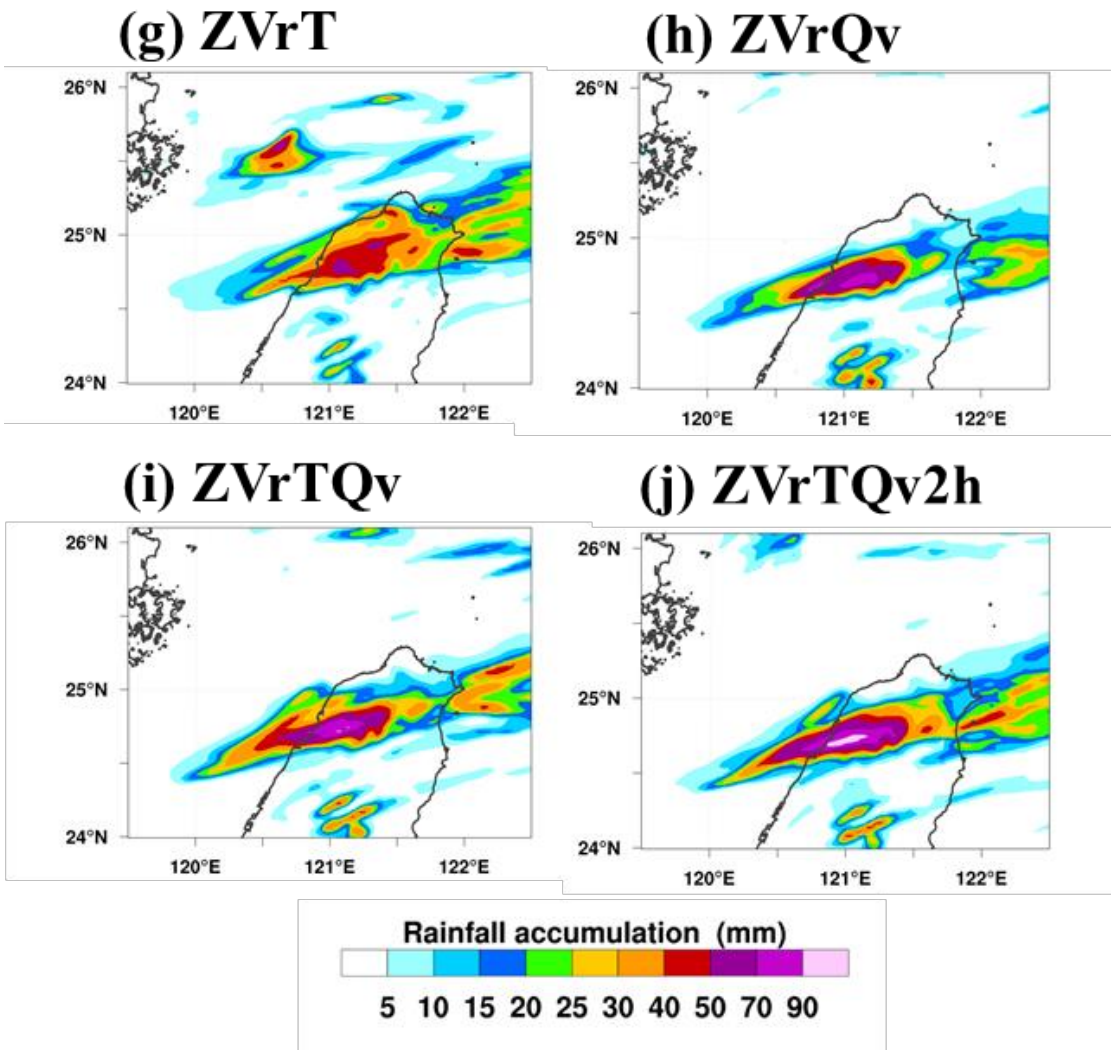

Fig. 5-11. Rainfall accumulation at northern Taiwan in d03 from 1400 UTC to 1700 UTC. (a) Truth; (b) NoDA; (c) Z; (d) Vr; (e) ZVr; (f) ZVr2h; (g) ZVrT; (h) ZVrQv; (i) ZVrTQv; (j) ZVrTQv2h.

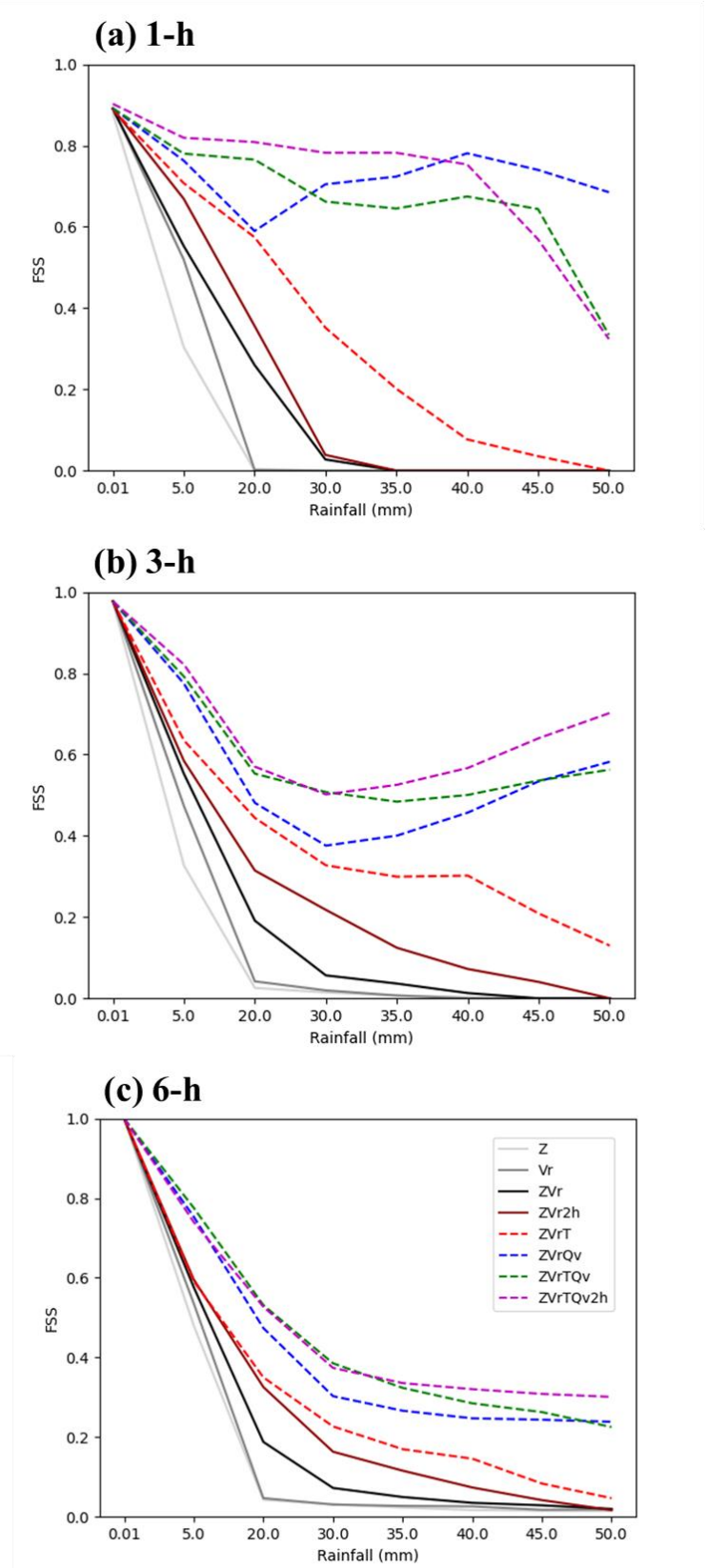

Fig. 5-12. Fractions Skill Score (FSS) of (a) 1-hr, (b) 3-hrs and (c) 6-hrs rainfall accumulation from 1400 UTC by deviation distance 24-km.

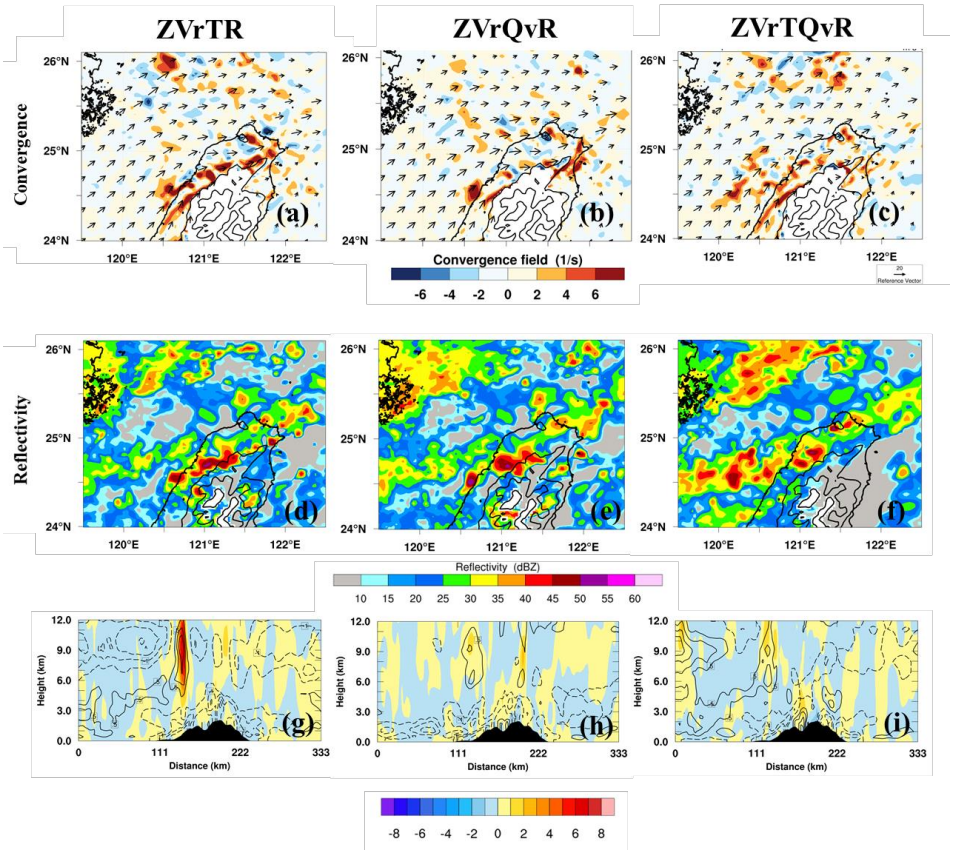

Fig. 5-13. Final analysis fields at 1400 UTC. ZVrTR (a, d, g), ZVrQvR (b, e, h), and ZVrTQvR (c, f, i). (a), (b), (c) same as Fig.12. (d), (e), (f) same as Fig.14. (g), (h), (i) same as Fig.15.

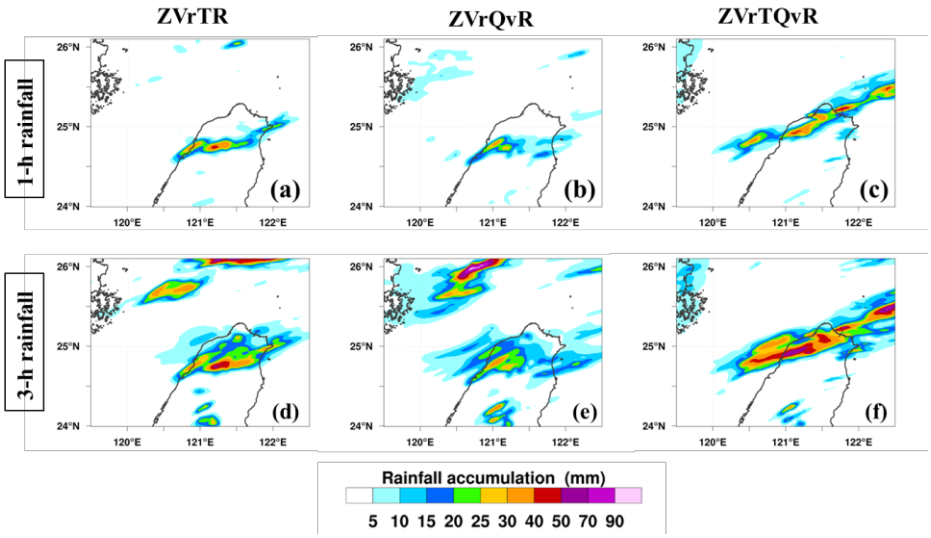

Fig. 5-14. Rainfall accumulation from 1400 UTC for 1-h (a), (b), and (c); for 3-h (d), (e), and (f). ZVrTR (a, d); ZVrQvR (b, e); ZVrTQvR (c, f).

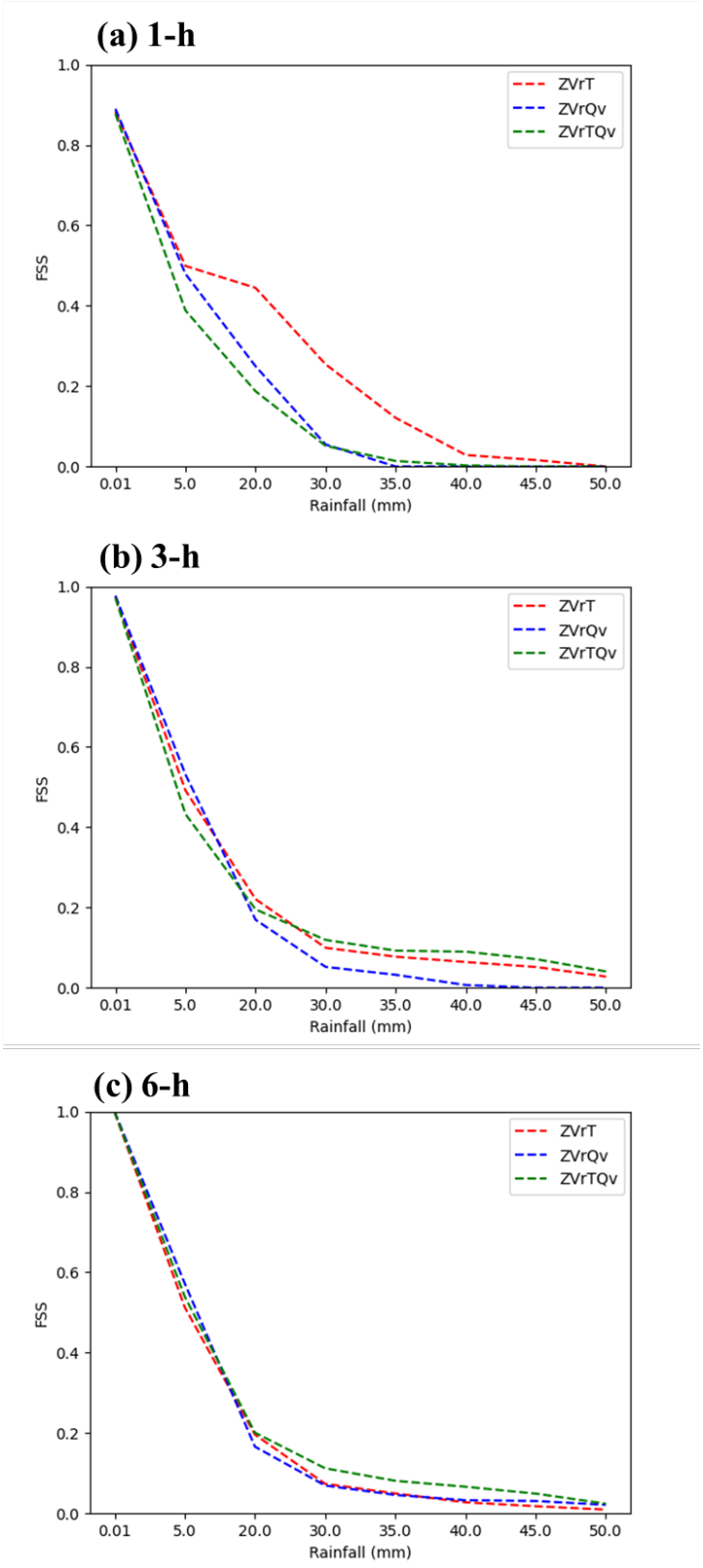

Fig. 5-15. FSSs of (a) 1-h, (b) 3-h, and (c) 6-h rainfall accumulation from 1400 UTC by deviation distance of 24-km.

Tables

Table 3-1. Features on the precipitation system in three stages.

Stage	State	Time (UTC)	Description
1	Fast speed (15 km hr^{-1})	1200 to 1230	The stage of precipitation system squall line structure
2	Landing (transition)	1300 to 1400	New cell merges to main convection region
3	Quasi-stationary	1430 to 1600	Extremely heavy rainfall happens at same area

Table 3-1. Features on the precipitation system in three stages.

Table 4-1. Summary of OSSE Experiments.

No.	Experiment	Initial condition	Assimilation period	Assimilation Radar data	Assimilation thermodynamic information
1	Truth	ERA-interim	-	-	-
2	NoDA	NCEP-FNL	-	-	-
3	Z	NCEP-FNL	1 h	Z	-
4	Vr	NCEP-FNL	1 h	Vr	-
5	ZVr	NCEP-FNL	1 h	Z, Vr	-
6	ZVr2h	NCEP-FNL	2 h	Z, Vr	-
7	ZVrT	NCEP-FNL	1 h	Z, Vr	T
8	ZVrQv	NCEP-FNL	1 h	Z, Vr	Qv
9	ZVrTQv	NCEP-FNL	1 h	Z, Vr	T, Qv
10	ZVrTQv2h	NCEP-FNL	2 h	Z, Vr	T, Qv
11	ZVrTR	NCEP-FNL	1 h	Z, Vr	Retrieved T
12	ZVrQvR	NCEP-FNL	1 h	Z, Vr	Retrieved Qv
13	ZVrTQvR	NCEP-FNL	1 h	Z, Vr	Retrieved T, Qv

Table 4-1. Summary of OSSE Experiments: Exp.1 (truth) and Exp.2 (NoDA) are simulated from ERA-interim and NCEP-FNL reanalyses, respectively. There are three sets of data assimilation in the study: 1) Exps. 3–6 that only assimilate radar data (Z and/or Vr). 2) Exps. 7–10 that assimilate radar data with additional thermodynamic data (T and/or Qv) generated from Exp.1 (truth). 3) Exps. 10–13 that assimilate radar data with thermodynamic data retrieved via TPTRS.